Hidemaro Suwa

Geometrically Constructed Markov Chain Monte Carlo Study of Quantum Spin-phonon Complex Systems

Springer

Springer Theses

Recognizing Outstanding Ph.D. Research

Aims and Scope

The series "Springer Theses" brings together a selection of the very best Ph.D. theses from around the world and across the physical sciences. Nominated and endorsed by two recognized specialists, each published volume has been selected for its scientific excellence and the high impact of its contents for the pertinent field of research. For greater accessibility to non-specialists, the published versions include an extended introduction, as well as a foreword by the student's supervisor explaining the special relevance of the work for the field. As a whole, the series will provide a valuable resource both for newcomers to the research fields described, and for other scientists seeking detailed background information on special questions. Finally, it provides an accredited documentation of the valuable contributions made by today's younger generation of scientists.

Theses are accepted into the series by invited nomination only and must fulfill all of the following criteria

- They must be written in good English.
- The topic should fall within the confines of Chemistry, Physics, Earth Sciences, Engineering and related interdisciplinary fields such as Materials, Nanoscience, Chemical Engineering, Complex Systems and Biophysics.
- The work reported in the thesis must represent a significant scientific advance.
- If the thesis includes previously published material, permission to reproduce this must be gained from the respective copyright holder.
- They must have been examined and passed during the 12 months prior to nomination.
- Each thesis should include a foreword by the supervisor outlining the significance of its content.
- The theses should have a clearly defined structure including an introduction accessible to scientists not expert in that particular field.

Hidemaro Suwa

Geometrically Constructed Markov Chain Monte Carlo Study of Quantum Spin-phonon Complex Systems

Doctoral Thesis accepted by
The University of Tokyo, Tokyo, Japan

Author (Current Address)
Dr. Hidemaro Suwa
Department of Physics
Boston University
Boston, MA
USA

Supervisor
Prof. Synge Todo
The University of Tokyo
Tokyo
Japan

Parts of this thesis have been published in the following journal articles:

- Hidemaro Suwa and Synge Todo

"Markov Chain Monte Carlo Method without Detailed Balance"
Phys. Rev. Lett. **105**, 120603 (2010); arXiv 1007.2262

- Hidemaro Suwa and Synge Todo

Butsuri, 66, 370 (2011) in Japanese

- Hidemaro Suwa and Synge Todo

"Geometric Allocation Approach for the Transition Kernel of a Markov Chain"
Monte Carlo Methods and Applications, 213–222 (2012); arXiv:1106.3562
Proceedings of the 8th IMACS Seminar on Monte Carlo Methods, August 29–
September 2, 2011,
Borovets, Bulgaria, Edited by Sabelfeld, Karl K./Dimov, Ivan
DE GRUYTER
Arxiv list:

- Hidemaro Suwa and Synge Todo

"General Construction of Irreversible Kernel in Markov Chain Monte Carlo"
arXiv:1207.0258

Supervisor's Foreword

Frustrated quantum magnets are one of the main subjects in the field of condensed matter physics and quantum statistical physics as a physical system in which novel quantum phases and quantum phase transitions can be realized. Spin-phonon coupling, the coupling between the spin and the lattice degrees of freedom, is one of the origins of spin frustration effects. In this thesis, Hidemaro Suwa has developed new and effective simulation algorithms that enable the detailed numerical analysis of the spin-phonon complex, and has revealed the nature of ground state and quantum critical phenomena of quantum magnets with effective frustrated interaction.

In Chap. 1, the spin-Peierls system, a typical spin-phonon complex, is introduced together with the difficulties and unsolved problems in that system. Especially, the demand for a novel numerical technique that can connect the adiabatic and anti-adiabatic limits, and the importance of the high dimensionality, i.e., the effects of interchain coupling, are emphasized. In Chap. 2, a generic Markov chain Monte Carlo algorithm that can greatly improve the convergence and relaxation of a Markov chain is proposed. The main idea here is expressing the problem of determination of transition probabilities for constructing a Markov chain as a geometric allocation (landfilling) problem. By using this new representation, it is shown that one can construct a rejection-minimized Markov chain that satisfies the balance condition without imposing a detailed balance. In Chap. 3, a new quantum Monte Carlo algorithm for the spin-Peierls system is presented. The standard worm algorithm, which is one of the most generic algorithms for the quantum lattice models, cannot be used for the spin-Peierls model as the number of bosons (quantum phonons) does not converge due to the spin-phonon coupling. In this thesis, several new techniques, such as the warp update and measuring off-diagonal Green's function, have been introduced in order to treat such a particle-number non-conserved system. In Chap. 4, a new finite-size scaling analysis technique, a combination of the level spectroscopy method, and the quantum Monte Carlo method, is proposed. This method is especially effective for the Kosterlitz-Thouless transition, for which the conventional finite-size scaling does not work at all.

By using the numerical techniques presented in the previous chapters, large-scale simulations for one and higher dimensional spin-Peierls systems have been performed in Chaps. 5 and 6. For one dimension, the ground-state phase diagram

of the *XXZ* spin-Peierls model is determined precisely by the level spectroscopy, and it is concluded that the ground-state phase diagram of the spin-Peierls system is qualitatively the same as in the frustrated zig-zag spin model realized in the anti-adiabatic limit; and thus the adiabatic limit and the anti-adiabatic one are connected continuously. In higher dimensions, the effects of interchain coupling are studied in detail. It is shown that in the case where the effective interchain interaction caused by the spin-phonon coupling has no frustration, the gapped dimer phase appears as soon as an infinitesimally weak interchain interaction is introduced. On the other hand, however, in the case where the effective couplings frustrate each other, it is demonstrated clearly that a two-dimensional quantum liquid phase is realized for the weak interchain coupling regime, which is also expected in the two-dimensional frustrated spin models.

To conclude, in this thesis, a promising approach for analyzing the frustrated quantum magnets has been demonstrated for the novel spin liquid phase and the exotic quantum phase transitions in the one- and two-dimensional spin-Peierls models. I believe this will have a great impact on the future studies of strongly correlated electron systems. Furthermore, the new numerical techniques developed for the Markov Chain Monte Carlo are quite generic and versatile, and are naturally expected to spread to all the fields of computational science.

Tokyo, July 2013   Synge Todo

Acknowledgments

Finally, let me thank my family from the bottom of my heart for their support— Kiyoteru, Sachie, Hitomi, and Sueko.

Contents

Chapter 1
Introduction

Frustrated quantum spin systems contain rich physical structures of nontrivial quantum states and phase transitions. Competing interactions can suppress any classical long-range order even at zero temperature and the system is fully governed by the strong quantum fluctuation, which is called the quantum spin liquid [3, 9]. As a result, it is predicted that an exotic or a fractional excitation characterizes the low-energy physics, such as the vison (Z_2 vortex) [42, 71] or the spinon (quark in the condensed matter) [4]. The origin of frustration can be a geometric structure or a long-range interaction and so on. Experimentally, the organic compounds, κ-(BEDT-TTF)$_2$Cu$_2$(CN)$_3$ [72] and EtMe$_3$Sb[Pd(dmit)$_2$]$_2$ [36], which can be modeled as the S = 1/2 quantum spin system on the triangular lattice, show no magnetic order even at very low temperatures. In addition, the materials forming the kagomé lattice, ZnCu$_3$(OH)$_6$Cl$_2$ (herbertsmithite) [49] and BaCu$_3$V$_2$O$_8$(OH)$_2$ (vesignieite) [57], are also candidates of the quantum spin liquid, while a peculiar order was observed in another kagomé lattice system, Cu$_3$V$_2$O$_7$(OH)$_2 \cdot$ 2H$_2$O (volborthite) [34]. On the other hand, the role of farther spin interactions have been investigated theoretically. It has been reported, for example, that the next-nearest neighbor interaction on the square lattice [69] and honeycomb lattice [2] brings about an interesting liquid phase in a *finite* parameter range; classical models usually does not produce such a finite-range disorder phase at absolute zero temperature. It is very important to elucidate the mechanism of the frustrated quantum spin systems as a grand challenge in the condensed matter physics and the materials design.

The farther spin-spin interactions stem from a coupling with other degrees of freedom in many realistic materials. Among them, the spin-lattice interaction has a large contribution for the determination of the effective spin interaction. As a system dominated by the spin-lattice interaction, a spin-Peierls system has caught the attention for a long time. When the decrease in energy by dimerization, forming spin singlet pairs, exceeds the increase by lattice distortion, the spin-Peierls system turns into the dimer phase, which is called the spin-Peierls transition. This formation of the singlet pairs results entirely from the quantum nature of the spin degrees of freedom. The analysis of this system and transition will bring understanding of the

role of lattice degrees of freedom and nontrivial frustrated spin systems in condensed matter physics.

In the spin-Peierls system, the quantum effect of the lattice degree of freedom is controversial. The hybridization of the two degrees of freedom depends on the difference of the energy scales. Theoretically, two limiting cases have been mainly investigated in the system: the adiabatic limit and the antiadiabatic limit. The former case, where the energy scale of the phonon is much smaller than that of the spin and the quantum nature of lattice is ignored, is approximately realized in some organic materials: for example, TTF-CuBDT [15, 37] found as the first spin-Peierls material in 1975. The low-energy physics is described by the $S = 1/2$ one-dimensional antiferromagnetic Heisenberg chain coupled with the lattice degree of freedom in the harmonic potential. Cross and Fisher [23] analyzed this model by using the abelian bosonization method [30] combined with the random phase approximation (RPA) in the adiabatic limit. Their theory seems effective to the organic materials because a soft phonon mode that was one of the assumptions in their theory was actually observed in the experiments.

The Cross-Fisher theory is, however, considered to be not valid to $CuGeO_3$ [5, 32, 40, 65, 73, 80] that was discovered as the first inorganic spin-Peierls material in 1993. It is because that the energy scale of phonon is the same order with that of spin [13, 14], which is away from the adiabatic region, and no soft phonon was observed experimentally. Interestingly, Gros and Werner [31] showed later that the RPA treatment does not always result in the soft phonon. They argued the validity of the Cross-Fisher theory to the inorganic compound, comparing with the phenomeno-logical theories for the central peak occurring in structural phase transitions [16]. In addition, Pouget et al. [60, 61] discussed the comparison between the RPA calculation and the experimental data in the correlation length. They argued that the phonon spectral function calculated by the mean-field treatment supported well the phe-nomenological theories. About the dynamical property, furthermore, the magnetic excitation spectrum with the static dimerization, which corresponds to the adiabatic limit, has been calculated; there, the magnon peak and the soliton continuum have been interestingly compared to the experimental data [79, 82]. As stated above, the possibility of explaining the experimental data of the inorganic material from the adiabatic limit is still being discussed.

Nevertheless, the discovery of $CuGeO_3$ triggered many theoretical approaches from the antiadiabatic limit: the perturbation expansion [45], the linked cluster expan-sion [78], the Lanczos diagonalization method [6, 7, 17, 87], the flow equation method [63, 64, 81], the unitary transformation [1, 85, 86, 88], and the density matrix renormalization group (DMRG) [18, 20, 38, 59, 85]. According to these approaches, tracing out the phonon degree of freedom produces a long-range spin interaction and an effective frustration. Perticularly, the next-nearest neighbor antifer-romagnetic interaction (J_2) plays an essential role for the construction of the singlet dimers as the famous Majumdar-Ghosh point [47].

Intriguingly, these two limits produce a qualitatively different phase diagram. In the adiabatic limit, the lattice degree of freedom is nothing but a classical parameter, and the phase diagram is the same with the spin model with the alternating interaction.

The alternating *XXZ* spin model can be mapped onto the quantum Ashkin-Teller model [43], the hidden $Z_2 \times Z_2$ symmetry [39] being manifested. For the isotropic Heisenberg point, the infinitesimal alternation that corresponds to the infinitesimal spin-lattice coupling drives the ground state into the dimer phase. This alternating-bond model, in the meanwhile, can be mapped to the quantum sine-Gordon model with double frequencies [25, 27, 41, 68] through the bosonization technique. There, the alternating interaction term is relevant; the corresponding critical dimension is 1/2, being less than the system dimension 2. Thus the gap is instantaneously formed by introducing the relevant interaction. These analyses and the Cross-Fisher conclusion are totally consistent.

In the antiadiabatic limit, on the other hand, a simple effective model is the frustrated J_1-J_2 spin model [45, 85]. This model can also be transformed to the quantum sine-Gordon model [45, 54]. For the isotropic point, in this case, the next-nearest neighbor J_2 term is reduced to the marginal interaction term in the sine-Gordon model. When the marginal term becomes zero, the Kosterlitz-Thouless (KT) type [44] quantum phase transition from the Tomonaga-Luttinger liquid phase to the dimer phase occurs [28]. This transition is corresponding to the pairing of spinless fermion at half filling in the Su-Schrieffer-Heeger model [74], which is clear through the Jordan-Wigner transformation. That is, the antiadiabaticity brings about the critical point at a finite spin-phonon interaction.

The question is, then, how the two limits connect with each other. For this crossover problem, the self-consistent harmonic approximation [21, 24, 52] and the renormalization group (RG) method [8, 19, 21, 28, 75] have been applied to the effective models. Particularly, Sun et al. [75] solved numerically the RG equations of the effective action and obtained the phase diagram of the *XXZ* spin-Peierls model over the whole adiabaticity. About this analysis, however, Citro et al. [21] claimed that the result was not correct because an invalid scaling [84] was used. The phase diagram needs to be investigated by a more reliable approach. In addition, some realistic materials have been found where the ratio of the spin and phonon energy scales is away from the two limits, such as $CuGeO_3$ and $MEM(TCNQ)_2$ [12, 35, 83]. The mechanism of the phase transitions are still contentious.

Not only for understanding the difference between the limits but also for explaining the behavior of realistic materials, it is important to analyze the crossover between them. An accurate calculation for the intermediate region, however, has been difficult because of the complexity of the system. Meanwhile, it is expected that the quantum Monte Carlo (QMC) method can treat the large-scale spin-Peierls system without approximation, but the conventional methods [46, 48, 51, 58, 64, 67] cannot calculate it efficiently as we will explain in detail in Chap. 3.

On these backgrounds, we will introduce a novel quantum Monte Carlo method that can correctly treat the particle-number-nonconserving system, such as the spin-Peierls model. We extend further the worm [62] (directed-loop [77]) algorithm that is now the most robust and standard method of the QMC update method based on the worldline representation [11, 66, 76]. There, the worm-bounce process that is a kind of rejection has been a bottleneck of the method for efficient calculations. For the determination of transition probability, usually, the detailed balance equation

is solved as the Metropolis (or Metropolis-Hastings) algorithm [33, 50] or the heat bath algorithm (Gibbs sampler) [10, 22, 29]. However, these canonical algorithms are not optimal. We, in the present thesis, invent a new optimization method for the transition kernel of Markov chain; rewriting the algebraic problem into a geometric problem, we indeed always minimize the average rejection rate. Applying the geometric optimization method, we completely eliminate the bounce process of bosonic-worm scattering in the spin-Peierls model. This is a crucial improvement for correct calculations. As a remarkable point, our algorithm is the first Markov chain Monte Carlo method that is free from the detailed balance for general cases since the invention of the method in 1953 [50].

For the analysis of the spin-Peierls transitions, a tricky problem remains; it is extremely difficult to apply the finite-size scaling method for the KT transition [26, 70]. In the meanwhile, the level spectroscopy [53–56] was first developed for the determination of the critical point of the frustrated J_1-J_2 spin model. The method powerfully performed for the analyses of the difficult phase transitions, such as the KT transition, where the strong finite-size effect hinders us to extrapolate the thermodynamic limit correctly. The combination of the level spectroscopy and the QMC method sounds fascinating, but it is not trivial because the needed energy gaps cannot be accurately calculated by the conventional way. In the present thesis, we propose a new gap-estimator sequence that converges a true gap value without systematic error. By calculating the energy gap in terms of the useful estimators, we make it possible, for the first time, to combine the level spectroscopy with the QMC method.

Fully utilizing the above novel methods, we will elucidate the phase diagram of the *XXZ* spin-Peierls chain. Surprisingly, even under the small quantum effect of the lattice degree of freedom, the ground state and the universality class are consistent to the frustrated J_1-J_2 spin model, which is a simple effective model in the antiadiabatic limit. We will show the previous RG analysis is not correct. The universality class is unambiguously identified by the QMC level spectroscopy. We will also show the calculations of the spin velocity and the central charge that are important physical quantities in the conformal field theory, for the first time by the QMC method.

From the other point of view, we can indeed simulate critical phenomena of effectively frustrated quantum spin models. It has long been a big challenge to apply the QMC technique to frustrated systems; the negative sign problem prevents us from getting valid statistical averages. However, there is no negative sign over the relevant parameter region in the spin-Peierls model. In other words, we are successful in avoiding the problematic sign with the help of the quantum phonon degree of freedom as an auxiliary field. This fact encourages us to apply the present methods to more complex systems beyond the simple chain.

We investigate, in this thesis, the multi-chain and two-dimensional system where the chains are connected by the lattice interaction through the harmonic potential. This extension is natural because the lattice interaction does usually not have a low-dimensional feature in contrast to the electron interaction; that is why it forms the solid realistically. We will discuss that the system instantaneously turns into the dimer phase with unfrustrated interchain phonon interaction, but, with full frustration, the ground state is a nontrivial liquid state in weak coupling region and the phase

transition to a dimer phase occurs at a finite spin-phonon coupling. This is the first discovery of a two-dimensional liquid phase by the worldline QMC method for effectively frustrated quantum spin models. The liquid ground state is presumably described by the one-dimensional feature where the lowest excitation is the deconfined spinon.

The organization of the present thesis is as follows: In Chap. 2, we will propose the geometric allocation algorithms for creating a transition kernel of Markov chain after reviewing the previous research of optimized transition matrices. In Chap. 3, the extended QMC method for nonconserved particles is presented together with the detailed update of the spin-Peierls model being exemplified. In Chap. 4, we will introduce the level spectroscopy and the new gap estimators accessed by the QMC calculation. By the above three methods, the phase diagram and the universality class of the *XXZ* spin-Peierls model are discussed in detail in Chap. 5. The ground state of the multi-chain and the two-dimensional spin-Peierls system is investigated in Chap. 6. Finally, the last chapter is the summary.

References

1. Akiyama, S., & Yasuda, C. (2011). Quantum phase transition in antiferromagnetic Heisenberg chains coupled to phonons. *Journal of the Physical Society of Japan*, *80*(104), 709.
2. Albuquerque, A., Schwandt, D., Hetényi, B., Capponi, S., Mambrini, M., & Läuchli, A. M. (2011). Phase diagram of a frustrated quantum antiferromagnet on the honeycomb lattice: Magnetic order versus valence-bond crystal formation. *Physical Review B*, *84*(024), 406.
3. Anderson, P. W. (1987). The resonating valence bond state in La_2CuO_4 and superconductivity. *Science*, *235*, 1196.
4. Anderson, P. W., Baskaran, G., Zou, Z., & Hsu, T. (1987). Resonating-valence-bond theory of phase transitions and superconductivity in La_2CuO_4-based compounds. *Physical Review Letters*, *58*, 2790.
5. Arai, M., Fujita, M., Motokawa, M., Akimitsu, J., & Bennington, S. M. (1996). Quantum spin excitations in the spin-Peierls system $CuGeO_3$. *Physical Review Letters*, *77*, 3649.
6. Augier, D., & Poilblanc, D. (1998). Dynamical properties of low-dimensional $CuGeO_3$ and NaV_2O_5 spin-Peierls systems. *European Physical Journal B: Condensed Matter Physics*, *1*, 19–28.
7. Augier, D., Poilblanc, D., Sørensen, E., & Affleck, I. (1998). Dynamical effects of phonons on soliton binding in spin-Peierls systems. *Physical Review B*, *58*, 9110–9113.
8. Bakrim, H., & Bourbonnais, C. (2007). Quantum versus classical aspects of one dimensional electron-phonon systems revisited by the renormalization group method. *Physical Review B*, *76*(195), 115.
9. Balents, L. (2010). Spin liquids in frustrated magnets. *Nature*, *464*, 199–208.
10. Barker, A. A. (1965). Monte Carlo calculations of the radial distribution functions for a proton-electron plasma. *Australian Journal of Physics*, *18*, 119.
11. Beard, B. B., & Wiese, U. J. (1996). Simulations of discrete quantum systems in continuous Euclidean time. *Physical Review Letters*, *77*, 5130.
12. van Bodegom, B., Larson, B. C., & Mook, H. A. (1981). Diffuse x-ray and inelastic neutron scattering study of the spin Peierls transition in N-methyl-N-ethyl-morpholinium bistetracyanoquinodimethane [MEM(TCNQ)$_2$]. *Physical Review B*, *24*, 1520–1523.
13. Braden, M., Hennion, B., Reichardt, W., Dhalenne, G., & Revcolevshi, A. (1998). Spin-phonon coupling in $CuGeO_3$. *Physical Review Letters*, *80*, 3634.

14. Braden, M., Reichardt, W., Hennion, B., Dhalenne, G., & Revcolevschi, A. (2002). Lattice dynamics of CuGeO$_3$: Inelastic neutron scattering and model calculations. *Physical Review B*, *66*(214), 417.

15. Bray, J., Hart, H. R., Interrante, L. V., Jacobs, I. S., Kasper, J. S., Watkins, G. D., et al. (1975). Observation of a spin-Peierls transition in a Heisenberg antiferromagnetic linear-chain system. *Physical Review Letters*, *35*, 744.

16. Bruce, A. D., & Cowley, R. A. (1981). *Structural Phase Transitions*. London: Taylor & Francis.

17. Büchner, B., Fehske, H., Kampf, A. P., & Wellein, G. (1999). Lattice dimerization in the spinPeierls compound CuGeO$_3$. *Physica B: Condensed Matter*, *259–261*, 956.

18. Bursill, R. J., McKenzie, R. H., & Hamer, C. J. (1999). Phase diagram of a Heisenberg spin-Peierls model with quantum phonons. *Physical Review Letters*, *83*, 408.

19. Caron, L. G., & Bourbonnais, C. (1984). Two-cutoff renormalization and quantum versus classical aspects for the one-dimensional electron-phonon system. *Physical Review B*, *29*, 4230–4241.

20. Caron, L. G., & Moukouri, S. (1996). Density matrix renormalization group applied to the ground state of the *XY* spin-Peierls system. *Physical Review Letters*, *76*, 4050.

21. Citro, R., Orignac, E., & Giamarchi, T. (2005). Adiabatic-antiadiabatic crossover in a spin-Peierls chain. *Physical Review B*, *72*(024), 434.

22. Creutz, M. (1980). Monte Carlo study of quantized SU(2) gauge theory. *Physical Review D*, *21*, 2308.

23. Cross, M. C., & Fisher, D. S. (1979). A new theory of the spin-Peierls transition with special relevance to the experiments on TTFCuBDT. *Physical Review B*, *19*, 402.

24. Dashen, R.F., Hassiacher, B., & Neveu, A. (1974). Nonperturbative methods and extended-hadron models in field theory. I. semiclassical functional methods. *Physical Review D*, *10*, 4114–4129.

25. Delfino, G., & Mussardo, G. (1998). Non-integrable aspects of the multi-frequency sine-Gordon model. *Nuclear Physics B*, *516*, 675–703.

26. Edwards, R., Goodman, J., & Sokal, A. (1991). Multi-grid Monte Carlo (ii). two-dimensional XY model. *Nuclear Physics B*, *354*, 289–327.

27. Fabrizio, M., Gogolin, A., & Nersesyan, A. (2000). Critical properties of the double-frequency sine-Gordon model with applications. *Nuclear Physics B*, *580*, 647–687.

28. Fradkin, E., & Hirsch, J. E. (1983). Phase diagram of one-dimensional electron-phonon systems. I. the Su-Schrieffer-Heeger model. *Physical Review B*, *27*, 1680–1697.

29. Geman, S., & Geman, D. (1984). Stochastic relaxation, Gibbs distributions and the Bayesian restoration of images. *IEEE Transactions on Pattern Analysis and Machine Intelligence*, *6*, 721.

30. Giamarchi, T. (2004). *Quantum physics in one dimension*. New York: Oxford University Press, *50*, 2743–2762.

31. Gros, C., & Werner, R. (1998). Dynamics of the Peierls-active phonon modes in CuGeO$_3$. *Physical Review B*, *58*(R14), 677.

32. Hase, M., Terasaki, I., & Uchinokura, K. (1993). Observation of the spin-Peierls transition in linear Cu^{2+} (spin-$\frac{1}{2}$) chains in an inorganic compound CuGeO$_3$. *Physical Review Letters*, *70*, 3651.

33. Hastings, W. K. (1970). Monte Carlo sampling methods using Markov chains and their applications. *Biometrika*, *57*, 97.

34. Hiroi, Z., Yoshida, H., Okamoto, Y., & Yoshida, M. (2011). Novel magnetic order in the kagome lattice of volborthite. *Journal of Physics: Conference Series*, *320*(012), 003.

35. Huizinga, S., Kommandeur, J., Sawatzky, G. A., Thole, B. T., Kopinga, K., de Jonge, W. J. M., et al. (1979). Spin-Peierls transition in N-methyl-N-ethyl-morpholinium-ditetracyanoquinodimethanide [MEM $-$ (TCNQ)$_2$]. *Physical Review B*, *19*, 4723–4732.

36. Itou, T., Oyamada, A., Maegawa, S., Tamura, M., & Kato, R. (2007). Spin-liquid state in an organic spin-1/2 systemon a triangular lattice, EtMe$_3$Sb[Pd(dmit)$_2$]$_2$. *Journal of Physics: Condensed Matter*, *19*(145), 247.

37. Jacobs, I. S., Bray, J. W., Hart, H. R., Interrante, J. L., Kasper, J. S., & Watkins, G. D. (1976). Spin-Peierls transitions in magnetic donor-acceptor compounds of thetrathiafulvalene (TTF) with bisdithiolene metal complexes. *Physical Review B*, *14*, 3036.

38. Jeckelmann, E., Zhang, C., & White, S. R. (1999). Metal-insulator transition in the one-dimensional Holstein model at half filling. *Physical Review B*, *60*, 7950–7955.

39. Kennedy, T., & Tasaki, H. (1992). Hidden $Z_2 \times Z_2$ symmetry breaking in Haldane-gap antiferromagnets. *Physical Review B*, *45*, 304–307.

40. Kikuchi, J., Matsuoka, T., Motoya, K., Yamauchi, T., & Ueda, Y. (2002). Absence of edge localized moments in the doped spin-Peierls system $CuGe_{1-x}Si_xO_3$. *Physical Review Letters*, *88*(037), 603.

41. Kitazawa, A., & Nomura, K. (1997). Critical properties of $S = 1$ bond-alternating XXZ chains and hidden $Z_2 \times Z_2$ symmetry. *Journal of the Physical Society of Japan*, *66*, 3944–3956.

42. Kivelson Steven, A., Rokhsar Daniel, S., & Sethna James, P. (1987). Topology of the resonating valence-bond state: Solitons and high-T, superconductivity. *Physical Review B*, *35*, 8865–8868.

43. Kohmoto, M., den Nijs, M., & Kadanoff Leo, P. (1981). Hamiltonian studies of the $d = 2$ Ashkin-Teller model. *Physical Review B*, *24*, 5229.

44. Kosterlitz, J. M., & Thouless, D. J. (1973). Ordering, metastability and phase transitions in two-dimensional systems. *Journal of Physics C*, *6*, 1181.

45. Kuboki, K., & Fukuyama, H. (1987). Spin-Peierls transition with competing interactions. *Journal of the Physical Society of Japan*, *56*, 3126–3134.

46. Kühne, R. W., & Löw, U. (1999). Thermodynamical properties of a spin-$\frac{1}{2}$ Heisenberg chain coupled to phonons. *Physical Review B*, *60*(12), 125.

47. Majumdar, C. K., & Ghosh, D. K. (1969). On next-nearest-neighbor interaction in linear chain. I. *Journal of Mathematics and Physics*, *10*, 1388–1398. DOI:10.1063/1.1664978.

48. McKenzie, R. H., Hamer, C. J., & Murray, D. W. (1996). Quantum Monte Carlo study of the one-dimensional Holstein model of spinless fermions. *Physical Review B*, *53*, 9676–9687.

49. Mendels, P., Bert, F., de Vries, M. A., Olariu, A., Harrison, A., Duc, F., Trombe, J. C., Lord, J., Amato, A., & Baines, C. (2007). Quantum magnetism in the paratacamite family: Towards an ideal kagomé lattice. *Physical Review Letters*, *98*(077), 204.

50. Metropolis, N., Rosenbluth, A. W., Rosenbluth, M. N., Teller, A. H., & Teller, E. (1953). Equation of state calculations by fast computing machines. *The Journal of Chemical Physics*, *21*, 1087.

51. Michel, F., & Evertz, H. G. (2007). *Lattice dynamics of the Heisenberg chain coupled to finite frequency bond phonons*. cond-mat p. arXiv:0705.0799v2.

52. Nakano, T., & Fukuyama, H. (1981). Dimerization and solitons in one-dimensional XY-Z antiferromagnets. *Journal of the Physical Society of Japan*, *50*, 2489–2499.

53. Nomura, K. (1995). Correlation functions of the 2D sine-Gordon model. *Journal of Physics A: Mathematical and General*, *28*, 5451–5468.

54. Nomura, K., & Okamoto, K. (1994). Critical properties of $S = \frac{1}{2}$ antiferromagnetic XXZ chain with next-nearest-neighbour interactions. *Journal of Physics A: Mathematical and General*, *27*, 5773.

55. Nomura, K., & Okamoto, K. (2001). BKT transition and level spectroscopy. *Butsuri*, *56*, 836.

56. Nomura, K., & Okamoto, K. (2002). BKT transition and level spectroscopy. In *Proceedings on French-Japanese Symposium Quantum Properties of Low-Dimensional Antiferromagnets*; cond-mat/020172.

57. Okamoto, Y., Yoshida, H., & Hiroi, Z. (2009). Vesignieite $BaCu_3V_2O_8(OH)_2$ as a candidate spin-1/2 kagome antiferromagnet. *Journal of the Physical Society of Japan*, *78*(033), 701.

58. Onishi, H., & Miyashita, S. (2003). Quantum narrowing effect in a spin-Peierls system with quantum lattice fluctuation. *Journal of the Physical Society of Japan*, *72*, 392.

59. Pearson, C. J., Barford, W., & Bursill, R. J. (2010). Quantized lattice dynamic effects on the spin-Peierls transition. *Physical Review B*, *82*(144), 408.

60. Pouget, J. P. (2001). Microscopic interactions in $CuGeO_3$ and organic spin-Peierls systems deduced from their pretransitional lattice fluctuations. *European Physical Journal B: Condensed Matter Physics*, *20*, 321–333.

61. Pouget, J. P., Ravy, S., Schoeffel, J., Dhalenne, G., & Revcolevshi, A. (2004). Spin-Peierls lattice fluctuations and disorders in $CuGeO_3$ and its solid solutions. *European Physical Journal B: Condensed Matter Physics*, *38*, 581–598.
62. Prokof'ev, N. V., Svistunov, B. V., & Tupitsyn, I. S. (1998). Exact, complete, and universal continuous-time world-line Monte Carlo approach to the statistics of discrete quantum systems. *Soviet Physics JETP*, *87*, 310.
63. Raas, C., Bühler, A., & Uhrig, G. S. (2001). Effective spin models for spin-phonon chains by flow equations. *European Physical Journal B: Condensed Matter Physics*, *21*, 369–374.
64. Raas, C., Löw, U., Uhrig, G. S., & Kühne, R. W. (2002). Spin-phonon chains with bond coupling. *Physical Review B*, *65*(144), 438.
65. Regnault, L. P., Renard, J. P., Dhalenne, G., & Revcolevschi, A. (1995). Coexistence of dimerization and antiferromagnetism in Si-doped $CuGeO_3$. *Europhysics Letters*, *32*, 579–584.
66. Sandvik, A. W. (1999). Stochastic series expansion method with operator-loop update. *Physical Review B*, *59*(R14), 157.
67. Sandvik, A. W., & Campbell, D. K. (1999). Spin-Peierls transition in the Heisenberg chain with finite-frequency phonons. *Physical Review Letters*, *83*, 195.
68. Schulz, H. J. (1986). Phase diagrams and correlation exponents for quantum spin chains of arbitrary spin quantum number. *Physical Review B*, *34*, 6372.
69. Schulz, H. J., Ziman, T., & Poiblanc, D. (1994). Fluctuations in quantum antiferromagnets. In H. T. Diep (Ed.), *Magnetic Systems With Competing Interactions* (pp. 120–160). Singapore: World Scientific.
70. Seiler, E., Stamatescu, I., Patrascioiu, A., & Linke, V. (1988). Critical behaviour, scaling and universality in some two-dimensional spin models. *Nuclear Physics B*, *305*, 623–660.
71. Senthil, T., & Fisher Matthew, P. A. (2001). Fractionalization in the cuprates: Detecting the topological order. *Physical Review Letters*, *86*, 292–295.
72. Shimizu, Y., Miyagawa, K., Kanoda, K., Maesato, M., & Saito, G. (2003). Spin liquid state in an organic Mott insulator with a triangular lattice. *Physical Review Letters*, *91*(107), 001.
73. Simonet, V., Grenier, B., Villain, F., Flank, A. M., Dhalenne, G., Revcolevschi, A., et al. (2006). Effect of structural distortions on the magnetism of doped spin-Peierls $CuGeO_3$. *European Physical Journal B: Condensed Matter Physics*, *53*, 155–167.
74. Su, W. P., Schrieffer, J. R., & Heeger, A. J. (1979). Solitons in polyacetylene. *Physical Review Letters*, *42*, 1698–1701.
75. Sun, P., Schmeltzer, D., & Bishop, A. R. (2000). Analytic approach to the one-dimensional spin-Peierls system in the entire frequency range. *Physical Review B*, *62*, 11308–11311.
76. Suzuki, M. (1976). Relationship between d-dimensional quantal spin systems and $(d + 1)$-dimensional Ising systems. *Programming Theoretical Physics*, *56*, 1454.
77. Syljuasen, O. F., & Sandvik, A. W. (2002). Quantum Monte Carlo with directed loops. *Physical Review E*, *66*(046), 701.
78. Trebst, S., Elstner, N., & Monien, H. (2001). Renormalization of the spin-Peierls transition due to phonon dynamics. *Europhysics Letters*, *56*(2), 268–274.
79. Tsvelik, A. M. (1992). Spectrum of magnetic excitations in the spin-Peierls state. *Physical Review B*, *45*, 486–488.
80. Uchinokura, K. (2002). Spin-Peierls transition in $CuGeO_3$ and impurity-induced ordered phases in low-dimensional spin-gap systems. *Journal of Physics: Condensed Matter*, *14*, R195–R237.
81. Uhrig, G. S. (1998). Nonadiabatic approach to spin-Peierls transitions via flow equations. *Physical Review B*, *57*(R14), 004.
82. Uhrig, G. S., & Schulz, H. J. (1996). Magnetic excitation spectrum of dimerized antiferromagnetic chains. *Physical Review B*, *54*, R9624–R9627.
83. Visser, R. J. J., Oostra, S., Vettier, C., & Voiron, J. (1983). Determination of the spin-Peierls distortion in N-methyl-N-ethyl-morpholinium ditetracyanoquinodimethanide [$MEM(TCNQ)_2$]: Neutron diffraction study at 6 K. *Physical Review B*, *28*, 2074–2077.
84. Voit, J., & Schulz, H. J. (1988). Electron-phonon interaction and phonon dynamics in one-dimensional conductors. *Physical Review B*, *37*, 10068–10085.

85. Weiße, A., Hager, G., Bishop, A. R., & Fehske, H. (2006). Phase diagram of the spin-Peierls chain with local coupling: Density-matrix renormalization-group calculations and unitary transformations. *Physical Review B*, *74*(214), 426.
86. Weiße, A., Wellein, G., & Fehske, H. (1999). Quantum lattice fluctuations in a frustrated Heisenberg spin-Peierls chain. *Physical Review B*, *60*, 6566.
87. Wellein, G., Fehske, H., & Kampf, A. P. (1998). Peierls dimerization with nonadiabatic spin-phonon coupling. *Physical Review Letters*, *81*, 3956.
88. Zheng, H. (1997). Quantum lattice fluctuations in the ground state of an XY spin-Peierls chain. *Physical Review B*, *56*, 14414–14422.

Chapter 2
Geometric Allocation Approach in Markov Chain Monte Carlo

2.1 Markov Chain Monte Carlo

The Monte Carlo method was first devised by Ulam et al. [61] in 1947, and it has been enjoyed for a wide variety of applications in mathematics, physics, statistics, etc. According to the literature, the method is defined as a simulation that solves a deterministic problem by means of a stochastic way. Ulam and the coworkers used the Monte Carlo method for neutron diffusion problem in fissile material of atomic bombs and for the eigenvalue problem of the Schrödinger equation at Los Alamos during the World War II. In the both applications, the average of random sampling converges to a target integral.

Let $s \in N$ be a dimension and $D \subset R^s$ be an integral range on the Lebesgue measure (now we assume D is compact as topological space for simplicity), $x \in D$ be a continuous state variable, $f : R^s \to R$ be an integrand function, and I be a target integral defined as

$$I = \int_D f(x)dx, \tag{2.1}$$

which takes a finite value. If f has a finite mean and we generate M independent samples, $x_1, x_2, \ldots,$ in D, then the average of the function values at the samples

$$\hat{I}_M = \frac{1}{M} \sum_{i=1}^{M} f(x_i) \tag{2.2}$$

converges to the target value I almost surely, which is proved by *the strong law of large numbers*:

$$\hat{I}_M \overset{a.s.}{\to} I. \tag{2.3}$$

Moreover, if f has a finite variance v, *the central limit theorem* states the weak convergence (convergence in distribution):

$$\sqrt{M}(\hat{I}_M - I) \xrightarrow{d} N(0, v).\qquad(2.4)$$

Here $N(\mu', v')$ is the normal (Gaussian) distribution with the mean μ' and the variance v'.

The key point of the method is how the samples are chosen. The simple uniform sampling on the range D is feasible only for very low-dimensional problems. The relative error of the Monte Carlo average gets exponentially large as the dimension s becomes high, which is called the *the curse of dimensionality* [6]. For some low-dimensional problems (typically $s < 10$ or 100), the quasi Monte Carlo techniques have been developed [14, 33]. These are very useful in finance, for example; the price of derivative needs to be calculated very quickly. The idea of the quasi Monte Carlo is that the samples should be distributed in integral range with low "discrepancy" as shown in the widely known Koksma-Hlawka inequality [27]. Some algorithms for generation of low-discrepancy (artificial) sequence have been proposed, such as the degital (t, m, s)-nets (including the Soboĺ sequence [53], the Faure sequence [17], and the Niederreiter sequence [47]), the Halton sequence, the lattice rule, the Kronecker sequence and so on. By using these artful sequences, the order of convergence is drastically improved for some cases. For such a successful improvement, one of the key concepts is the *effective dimension* that is corresponding to the number of effective variables contributing to the variance of Monte Carlo average. Although these recent techniques have many interesting applications, it is still difficult to work well in high-dimensional problems including many physical systems.

An effective way for conquering the dimensional problem is *the importance sampling* where samples that have larger contribution to the integral are selected more often. The Markov chain Monte Carlo (MCMC) method [24, 32, 52] is a computational method that *approximately* generates samples stochastically from any target distribution. As a result of the importance sampling, an expectation value of a function (an observable) $O : X \rightarrow R$ (X is a state space) on the target distribution can be approximated from the simple average of the M samples:

$$\langle O \rangle = \frac{\int w(x)\, O(x) dx}{\int w(x) dx} \simeq \frac{1}{M} \sum_i O(x_i),\qquad(2.5)$$

where $w : X \rightarrow R$ is a weight function (measure). The MCMC method is a powerful tool for systems with multiple degrees of freedom (correlated high-dimensional problem) that are very important in the condensed matter physics. In this thesis, we use and extend the MCMC method for investigation of strongly correlated systems.

In the MCMC method, we start from an initial state (configuration), and the next state is stochastically chosen depending on the present configuration. Then the sequence of states (samples) constructs a Markov chain; the Markov property comes from the fact of dependency only on the one-step previous state. In other words, we set an initial distribution and continue to operate a kernel to the distribution at each Monte Carlo step. When an ergodicity condition holds, the distribution converges to an

equilibrium distribution. In the end, we can get samples from the target (equilibrium) distribution.

For a finite state space, the condition becomes easy if we take the natural discrete topology for the state space. It is because every open set is closed in this topology space and thus the Borel algebra (field) is trivial, which is the smallest closed set including all open sets. For a general space, however, the convergence condition is complicated. Usually, if a Markov chain is Harris positive recurrent and aperiodic, the chain is called ergodic [41, 59].[1] It is far from trivial to prove the ergodicity of a Markov chain in general. Necessarily in many practical simulations, the condition is simply assumed. Then, of course, we have to check the MC averages converge to the correct value. About our simulations in this thesis, we first confirmed the correctness by comparing with a more precise calculation, e.g., the numerical exact diagonalization, in simple or small systems (the diagonalization can be done only when the dimension of the Hilbert space is very small). Although we have not succeeded in mathematically proving the ergodicity in some cases, such a check is convincing enough to assure us the validity of the simulations. We, however, should keep in mind the mathematical conditions especially when we try to develop and improve the method.

Instead of the curse of dimensionality, the MCMC method suffers from the sample correlation. Since the next configuration is generated (updated) from the previous one, the samples are not independent of each other. Then the correlation gives rise to two problems: we have to wait for the distribution convergence (equilibration) before sampling, and the number of effective samples is decreased.

The former convergence problem is quantified by a distribution distance to the target. In many cases, the total variation distance

$$\| P^m(x, \cdot) - \pi(\cdot) \| = \sup_{A \in \mathscr{B}(X)} \left| P^m(x, A) - \pi(A) \right|, \tag{2.6}$$

is used, where $\mathscr{B}(X)$ is the Borel algebra, A is a Borel set, and $P^m(x, A) = P(x_m \in A | x_0 = x)$ is the m-step transition probability. For a finite state space, this is corresponding to the second largest eigenvalue in absolute value.

As an assessment for the latter problem, the decrease of the number of effective samples, the integrated autocorrelation time is defined as

$$\tau_{\text{int}} = \sum_{t=1}^{\infty} C(t) \tag{2.7}$$

$$C(t) = \frac{\langle O_{i+t} O_i \rangle - \langle O \rangle^2}{\langle O^2 \rangle - \langle O \rangle^2}, \tag{2.8}$$

---

[1] In the literature of physics, the ergodicity is confused with the irreducibility in many cases. If a state space is finite and a Markov chain is aperiodic, the ergodicity and the irreducibility are equivalent but they differ in a general state space.

where O_i is an observable at the i-th Monte Carlo step, and $C(t)$ is almost independent of i after the distribution convergence. This autocorrelation decreases the number of effective samples as

$$M_{\text{eff}} \simeq \frac{M}{1 + 2\tau_{\text{int}}}, \tag{2.9}$$

where M is the total number of samples in simulations. Although an MCMC method satisfying appropriate conditions guarantees correct results asymptotically in principle[2] [41], variance reduction of relevant estimators is crucial for the method to work in practice. If the central limit theorem holds, as we mentioned, the variance of expectations decreases as $v/M \simeq \text{var}(f)/M_{\text{eff}}$, where v is called the asymptotic variance that depends on the integrand function and the update method through the autocorrelation time.

What we have to concern is, thus, to shorten the distribution convergence (burn-in) time and to reduce the asymptotic variance. Optimal strategies against these two criteria must differ as we will explain in the next section. For most lattice systems (Markov random fields), however, it is presumably possible to improve conventional sampling methods in the both quantities. It is because the usual method is far from the global optimal strategy in the both respect.

There are three key points for the MCMC method to be effective. One is the choice of the ensemble. From the view of this respect, the extended ensemble methods, such as the multicanonical method [7] and the replica exchange method [28], have been proposed and applied successfully to protein folding problems, spin glasses, etc. The second is the selection of candidate configurations. The cluster algorithms, e.g., the Swendsen-Wang algorithm [57] and the loop algorithm [16], can overcome the critical slowing down by taking advantage of mapping to graph configurations in many physical models.[3] The hybrid (Hamiltonian) Monte Carlo method performs a simultaneous move, where the candidate state is chosen by taking the advantage of the Newtonian dynamics. The third is the determination of the transition probability, given candidate configurations. We focus our interest on this optimization problem of the probabilities in the following sections of this chapter.

2.2 Optimization of Transition Kernel

We will explain previous optimization approaches for transition kernel in the MCMC method in this section. Let us consider a finite state space now for simplicity. In the method, for the equilibrium distribution to be a target distribution, the (total) balance, the invariance of target distribution,

---

[2] All estimators measured in the MCMC method are biased. The ergodicity, however, ensures they are (strong) consistent. That is, the sequence of Monte Carlo average converges to the correct result in probability (almost surely).

[3] The improved estimator on the graph configuration reduces also the variance of the integrand function var(f).

$$w(c_i) = \sum_j w(c_i)p(c_i \to c_j) = \sum_j w(c_j)p(c_j \to c_i) \qquad \forall i, \qquad (2.10)$$

is imposed to the transition kernel.[4] In this equation, $p(c_i \to c_j)$ is a transition probability from configuration c_i to c_j, and $w(c_i)$ is an unnormalized weight (measure) of configuration c_i that is proportional to the normalized weight π_i. In most practical implementations, the Metropolis-Hastings algorithm [26, 40] (we call it simply the Metropolis algorithm below) or the heat bath algorithm [5, 11], namely, the Gibbs sampler [23] have been used for the determination of the transition probabilities. The next state is chosen by probability

$$p(c_i \to c_j) = \frac{1}{n-1} \min\left(1, \frac{w(c_j)}{w(c_i)}\right) \qquad i \neq j \qquad (2.11)$$

in the Metropolis algorithm, and

$$p(c_i \to c_j) = \frac{w(c_j)}{\sum_k w(c_k)} \qquad \forall i, j \qquad (2.12)$$

in the heat bath algorithm among n candidate states. These canonical algorithms satisfy the detailed balance, the reversibility,

$$w(c_i)p(c_i \to c_j) = w(c_j)p(c_j \to c_i) \qquad \forall i, j, \qquad (2.13)$$

which is a sufficient condition for the total balance (2.47). Under this condition, thanks to the simple property that every elementary transition balances with a corresponding inverse process (Fig. 2.1), it becomes easy to find a qualified transition probability by solving the equation for each pair of configurations as the Metropolis and the heat bath algorithm do. Attempts to optimizing the transition matrix have concentrated within this sufficient condition so far. We will review the previous optimization approaches below.
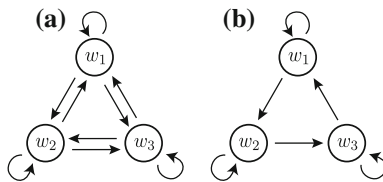
Fig. 2.1 Stochastic flow with the detailed balance (**a**) and without it (**b**). In the former, the flow balances with a corresponding inverse process. On the other hand, in the latter, a net stochastic flow exists as the result of breaking the detailed balance

---

[4] Note that there has been some interesting progress for generating samples from the target distribution asymptotically, the transition kernel being modified in an adaptive procedure [3].

2.2.1 Criteria of Markov Chain

Let S be a finite state space and n be the number of elements of S. Assume n is small enough to calculate the transition probabilities from all states to all. The discussion here can be easily extended to a conditional case in a huge state space; that is, we choose a state variable and update it on the condition that other variables are fixed. Let us also define an average of function f and inner product of f and g as

$$\langle f \rangle = \sum_{s \in S} f(s)\pi(s), \tag{2.14}$$

and

$$\langle f, g \rangle_{\pi} = \sum_{s \in S} f(s)g(s)\pi(s), \tag{2.15}$$

respectively. The following theorem connects the asymptotic variance and the eigenvalues of the reversible transition matrix, which are always real.

Theorem 2.2.1 *Let P be an irreducible and a reversible (w.r.t. π) stochastic matrix. Let x(0), x(1),… be a Markov chain on state space S with transition matrix P and $f: S \to \mathbb{R}$ For any initial distribution,*

$$v(f, P, \pi) = \lim_{M \to \infty} M \, \mathrm{var}\left(\frac{1}{M} \sum_{k=0}^{M-1} f[x(k)] \right) \tag{2.16}$$

$$= \langle (I - P)^{-1}(I + P)(f - \langle f \rangle 1), \, f - \langle f \rangle 1 \rangle_{\pi}. \tag{2.17}$$

This fact was proved first by Peskun [48]. Easy computations show that the above limit is equal to

$$\sum_{k=2}^{n} \frac{1 + \lambda_k}{1 - \lambda_k} \langle f, \bar{e}_k \rangle_{\pi}^2, \tag{2.18}$$

where $P\bar{e}_k = \lambda_k \bar{e}_k$, $\|\bar{e}_k\|_{\pi} = 1$. This is also described as

$$\sum_{k=2}^{n} \frac{1 + \lambda_k}{1 - \lambda_k} a_k \mathrm{var}(f), \tag{2.19}$$

where a_k are some nonnegative constants such that $\sum_k a_k = 1$. This formula links the asymptotic variance $v(f, P, \pi)$ to the eigenvalues and eigenvectors of P. In order to make the asymptotic variance small, it seems useful to use dynamics P with possibly *all* negative and small eigenvalues (except the largest one which is 1). In this sense, one can say that negative eigenvalues help the asymptotic variance get small.

The negative eigenvalues, however, do not always help the weak convergence (convergence in distribution) gets rapid. The m-step transition matrix $P^m(x, y) = P(x_m = y | x_0 = x)$ is represented as

$$P^m(x, y) = \sum_{k=1}^{n} e_k(x) e_k(y) \lambda_k^m. \tag{2.20}$$

The dominant term becomes $e_1(\cdot) = \pi(\cdot)$ for large m since $\lambda_1 = 1$. It is clear that the speed of the convergence depends on the second largest eigenvalue in absolute value.

These two goals seem to be in different point. We also mention the noticeable relation between them:

$$v(f, P, \pi) \le \frac{1 + |\lambda_2|}{1 - |\lambda_2|} \mathrm{var}(f) \le \frac{2}{1 - |\lambda_2|} \mathrm{var}(f). \tag{2.21}$$

Therefore, the spectral gap $1 - |\lambda_2|$ that determines the convergence rate gives also the upper bound of the asymptotic variance.

If the convergence is so slow that it is not possible to ignore the intrinsic bias of the MCMC sampler, we have to reduce the absolute value of the second eigenvalue. Once the equilibrium state becomes accessible in feasible time, the statistical efficiency, the asymptotic variance is more important to calculation.

2.2.2 Peskun's Theorem

There is a simple theorem as a guideline for the optimization. Let X be a discrete random variable following distribution π, and let P be the transition matrix of a Markov chain with π as its invariant distribution. Following Peskun [48], we define $P_2 \ge P_1$ for any two transition matrices if each of the off-diagonal elements of P_2 is grater than or equal to the corresponding off-diagonal elements of P_1. The following lemma is Theorem 2.1.1 of Peskun [48].

Lemma 2.2.1 (Peskun) *Suppose each of the irreducible transition matrices P_1 and P_2 is reversible for the same invariant probability distribution π. If $P_2 \ge P_1$, then, for any f,*

$$v(f, P_1, \pi) \ge v(f, P_2, \pi), \tag{2.22}$$

where

$$v(f, P, \pi) = \lim_{M \to \infty} M \, \mathrm{var}(\hat{I}_M), \tag{2.23}$$

and $\hat{I}_M = \sum_{i=1}^{M} f(x_i)/M$ is an estimator of $I = E_\pi(f)$ using M consecutive samples from the Markov chains.

Based on this theorem, a modified Gibbs sampler called the "Metropolized Gibbs sampler" was proposed by Liu [34, 35]. Assume ordering of the states as $\pi_1 \leq \pi_2 \leq \cdots \leq \pi_n$, where $\pi_i = w_i / \sum_i w_i$. In the heat bath algorithm, we choose the next state with forgetting the current state. Meantime, it is obvious that the rejection that the current state is chosen as the next state should be avoided as much as possible from the Peskun's theorem. Then, some will think we can exclude the current state at first proposal and use the Metropolis algorithm for going to the chosen state actually. Applying the heat bath algorithm at the first proposal seems plausible. This modified Gibbs sampler is reduced to the Metropolis algorithm for $n = 2$, not to the usual Gibbs sampler, which is also called the Barker's algorithm [5]. That is why it is called the Metropolized Gibbs sampler. By this approach, the transition matrix P is described as

$$P_{ij}^{MG} = \min(\pi_i/(1 - \pi_j), \pi_i/(1 - \pi_i)). \tag{2.24}$$

The matrix forms as

$$P^{MG} = \begin{bmatrix} 0 & \frac{\pi_1}{1-\pi_1} & \frac{\pi_1}{1-\pi_1} & \cdots & \frac{\pi_1}{1-\pi_1} \\ \frac{\pi_2}{1-\pi_1} & 1 - \cdots & \frac{\pi_2}{1-\pi_2} & \cdots & \frac{\pi_2}{1-\pi_2} \\ \frac{\pi_3}{1-\pi_1} & \frac{\pi_3}{1-\pi_2} & 1 - \cdots & \cdots & \frac{\pi_3}{1-\pi_3} \\ \vdots & \vdots & \vdots & \ddots & \vdots \\ \frac{\pi_n}{1-\pi_1} & \frac{\pi_n}{1-\pi_2} & \frac{\pi_n}{1-\pi_3} & \cdots & 1 - \cdots \end{bmatrix}, \tag{2.25}$$

where P_{ij} is the transition probability from i to j. Let P^{HB} be the transition matrix by using the normal heat bath algorithm. It follows that $P^{MG} \geq P^{HB}$ and hence the Peskun's theorem says the following theorem.

Theorem 2.2.2 *The Metropolized Gibbs sampler for discrete random variables as defined above is statistically more efficient than the usual heat bath algorithm (Gibbs sampler).*

2.2.3 Worst Case Solution

The above "Metropolization" always set to zero the diagonal element for the smallest-weight states. Interestingly, Frigessi et al. [21] showed that this procedure gives a kind of optimal property. Let us follow their theorems below.

At first, we have a general fact about the second largest eigenvalue as follows.

Theorem 2.2.3 (Frigessi, Hwang, Younes 1) *(a) The second largest eigenvalue of any stochastic matrix P, reversible w.r.t. π, is greater than or equal to*

$$- \frac{\pi_1}{1 - \pi_1}. \tag{2.26}$$

For all matrices whose second largest eigenvalue attains this lower bound, the corresponding eigenvector is

$$e_2 = (1 - \pi_1, -\pi_1, \ldots, -\pi_1)^T. \tag{2.27}$$

Furthermore, their first column has a zero as first entry and all other elements are equal to

$$\frac{\pi_1}{1 - \pi_1}. \tag{2.28}$$

That is, the matrix forms as

$$P = \begin{bmatrix} 0 & \frac{\pi_1}{1-\pi_1} & \cdots & \frac{\pi_1}{1-\pi_1} \\ \frac{\pi_2}{1-\pi_1} & & & \\ \vdots & & P_2 & \\ \frac{\pi_n}{1-\pi_1} & & & \end{bmatrix}, \tag{2.29}$$

where the submatrix P_2 is in detailed balance again. This is nothing but the Metropolization for the smallest-weight state.

(b) The above construction can be iterated to finally obtain a matrix with the following properties: (i) all the elements along the diagonal are zero, except possibly the last one; (ii) its eigenvalues are $1 = \lambda_1 > 0 > \lambda_2 \geq \cdots \geq \lambda_n$ and satisfy the property that λ_{i+1} attains the smallest possible value among all matrices (reversible w.r.t. π) that already possess the eigenvalues $1, \lambda_2, \ldots, \lambda_i$; (iii) its columns have constant entries under the diagonal, which are, respectively, $-\lambda_2, \ldots, -\lambda_n$. (iv) its eigenvectors are

$$e_1 = 1 \tag{2.30}$$

and

$$e_{k+1} = \delta_k - \langle \delta_k | 1, 2, \ldots, k - 1 \rangle_\pi, \quad k = 1, \ldots, n - 1, \tag{2.31}$$

where $1 = (1, \ldots, 1)^T$, $\delta_k = (0, \ldots, 1, \ldots, 0)^T$, and $\langle f | 1, 2, \ldots, k - 1 \rangle_\pi$ is the conditional expectation of f given the σ-algebra generated by the sets $1, \ldots, k - 1$ under the probability π; in vector notation,

$$e_{k+1} = \left(\underbrace{0, \ldots, 0}_{k-1 \text{terms}}, 1 - \frac{\pi_k}{\pi_k + \cdots + \pi_n}, -\frac{\pi_k}{\pi_k + \cdots + \pi_n}, \ldots, -\frac{\pi_k}{\pi_k + \cdots + \pi_n} \right)^T. \tag{2.32}$$

(c) Moreover, this matrix is the unique one which satisfies the previous condition (ii).

The resulting matrix, which we call the iterative Metropolized Gibbs sampler, is described as

$$
P^{IMG} = \begin{bmatrix}
0 & y_1 & y_1 & \cdots & & y_1 \\
\frac{w_2}{w_1} y_1 & 0 & y_2 & \cdots & & y_2 \\
\frac{w_3}{w_1} y_1 & \frac{w_3}{w_2} y_2 & 0 & \cdots & & y_3 \\
\vdots & \vdots & \vdots & \ddots & & \vdots \\
\frac{w_n}{w_1} y_1 & \frac{w_n}{w_2} y_2 & \frac{w_n}{w_3} y_3 & \cdots & 1 - y_1 - y_2 - \cdots
\end{bmatrix}, \tag{2.33}
$$

where $y_1 = \pi_1/(1 - \pi_1)$, $y_2 = (1 - y_1)\pi_2/(1 - \pi_1 - \pi_2)$, ... We do not prove this theorem here, but refer also some remarks.

Remark 2.2.1 *A final nonzero element on the diagonal may remain in the matrix of part (b). In fact this happens if and only if $\pi_{n-1} \neq \pi_n$.*

Remark 2.2.2 *It is not difficult to write down the values of $\lambda_2, \ldots, \lambda_n$. They are*

$$
\lambda_{k+1} = -y_k = -\frac{\pi_k}{\pi_{k+1} + \cdots + \pi_n} \prod_{\ell=1}^{k-1} \left(1 - \frac{\pi_\ell}{\pi_{\ell+1} + \cdots + \pi_n} \right). \tag{2.34}
$$

If $\pi_{k-1} = \pi_k$, then $\lambda_k = \lambda_{k+1}$. It is not surprising that $\delta_1 - \langle \delta_1 \rangle 1$ realizes the above bound. In other words, this means that the most difficult quantity to estimate by time averages is the probability of the least likely state. This seems consistent with intuition.

In addition, we have a relation between the eigenvalues and the asymptotic variance of integrand.

Corollary 2.2.1 *Let P be a stochastic matrix, reversible w.r.t. π. Let $v(P, \pi)$ be the maximum asymptotic variance of $(1/M) \sum_{i=1}^{M} f(x_i)$ for norm 1 functions f. Then*

$$
v(P, \pi) \geq \frac{1 + \lambda_2}{1 - \lambda_2} \tag{2.35}
$$

$$
\geq 1 - 2\pi_1, \tag{2.36}
$$

and any matrix that realizes this equality must have the properties given in Theorem 2.2.3(a) and hence be of the form (2.29).

This corollary says that the second largest eigenvalue is the lower bound of the asymptotic variance in the *worst* case, and the function is proportional to the eigenvector (2.32) that belongs to the second largest eigenvalue.

2.2.4 Four Optimization Problems

For an optimization problem, there are two interesting cases theoretically: the worst case and the average case. Our problem of the asymptotic variance is the minimization of the following two quantities; for the worst case

$$v(P, \pi) = \sup_{\langle f \rangle = 0, \langle f^2 \rangle = 1} v(f, P, \pi), \tag{2.37}$$

and for the average case

$$\bar{v}(P, \pi) = \int_{\langle f \rangle = 0, \langle f^2 \rangle = 1} v(f, P, \pi) dS(f), \tag{2.38}$$

where $dS(f)$ stands for the normalized surface area. We can consider these problem with/without the detailed balance. Set $\mathscr{P} = \{P : \pi P = \pi\}$ and $\mathscr{R} = \{P : P \text{ is reversible w.r.t. } \pi\}$. There are following 4 optimization problems:

(i) Minimize $v(P, \pi)$ over all $P \in \mathscr{R}$.
(ii) Minimize $v(P, \pi)$ over all $P \in \mathscr{P}$.
(iii) Minimize $\bar{v}(P, \pi)$ over all $P \in \mathscr{R}$.
(iv) Minimize $\bar{v}(P, \pi)$ over all $P \in \mathscr{P}$.

The above theorem we mentioned is the solution of (i), the worst case of reversible kernels.

2.2.5 Average Case Solution

Interestingly, Hwang these days has given the solution of (iv), the average case of irreversible kernel [30]. He proved the following important lemma and showed optimal solutions.

Theorem 2.2.4 (Hwang) *The average asymptotic variance is expressed by the trace of an inverse matrix:*

$$\bar{v}(P, \pi) = \int_{\langle f \rangle = 0, \langle f^2 \rangle = 1} v(f, P, \pi) dS(f) \tag{2.39}$$

$$= \frac{2}{n - 1} \text{tr}(1 - P)^{-1} - 1. \tag{2.40}$$

Then the trace has a lower bound:

$$\text{tr}(1 - P)^{-1} = \sum_j \pi_j E_\pi(T_j) \geq \sum_{i=1}^n (i - 1)\pi_i, \tag{2.41}$$

where

$$T_i = \inf\{t \geq 0 : x_t = i\}, \tag{2.42}$$

is a stopping time and x_t is a generated state at t-th Monte Carlo step.

　Then, there are at most 2^{n-2} transition matrices reaching the minimum. For the each transition matrix,

$$p_{i,i} = \begin{cases} 0 & i < n \\ \frac{\pi_n - \pi_{n-1}}{\pi_n} & i = n \end{cases} \tag{2.43}$$

and one of the following holds:

- $p_{2,1} = 1$ *and* $p_{1,i} = \pi_1/\pi_i$ *for some i.*
- $p_{1,2} = \pi_1/\pi_2$ *and* $p_{j,1} = 1$ *for some j.*

According to this theorem, the specific transition matrix,

$$P^{OPA} = \begin{bmatrix} 0 & 0 & \cdots & 0 & \frac{\pi_1}{\pi_n} \\ 1 & 0 & \cdots & 0 & \frac{\pi_2 - \pi_1}{\pi_n} \\ 0 & 1 & \cdots & 0 & \frac{\pi_3 - \pi_2}{\pi_n} \\ \vdots & \vdots & \ddots & \vdots & \vdots \\ 0 & 0 & \cdots & 1 & \frac{\pi_n - \pi_{n-1}}{\pi_n} \end{bmatrix}, \tag{2.44}$$

is one of the optimal matrices that gives the minimized average asymptotic variance. Note that the problems (ii) and (iii) are still open.

2.2.6 For Lattice Systems

When we can control the all matrix elements, the above theorems will be powerful. For lattice models (Markov random fields), however, we have to deal with a exponentially large number of states such that we need to update variables *locally* one by one. In fact, this is the main philosophy of the MCMC. Then, the optimization problem of the asymptotic variance becomes very difficult, and the above optimization schemes for local variables may not be efficient for the whole transition matrix.

　On lattice systems, Frigessi et al. proved an interesting theorem. Let D be a finite lattice (say, $D \subset \mathbb{Z}^2$), S_0 be a finite set and $S = (S_0)^D$. An element x of S will thus be a $|D| - tuple$, $x = (x_\sigma)_{\sigma \in D}$, $x_\sigma \in S_O$. We consider the measure π on S given by $\pi(x) = \exp(-\beta U(x))/Z_\beta$, where β is an inverse temperature and Z_β is a partition function (normalizing constant). We, now, consider the random update where the site to be updated is chosen uniformly at random. Their theorem is as follows.

Theorem 2.2.5 (Frigessi, Hwang, Younes 2) *(a) For any nonconstant* f,

$$v(f, P^{MG_1}, \pi) < v(f, P^{HB}, \pi), \tag{2.45}$$

where P^{MG_1} *is the transition matrix which is constructed by Metropolizing for only the minimum weight states in the local updates as the form (2.29), and* P^{HB} *is that by the heat bath algorithm. As a consequence, the second eigenvalue of* P^{MG_1} *is strictly smaller than the that of* P^{HB}.

(b) If β *is large enough and the potential* U *has at least two local minimums, then the second eigenvalue in absolute value of* P^{MG_1} *is strictly smaller than that of* P^{HB}.

This theorem states that the iterative Metropolized Gibbs sampler is always better than the heat bath algorithm in terms of asymptotic variance, and also weak convergence at least low temperature.

2.2.7 Other Approaches

As applications of the Metropolized Gibbs sampler, Loison et al. [38] researched the efficiency of the (single) Metropolized Gibbs sampler (they called it the restricted direct heat bath algorithm) in some $O(N)$ models. Pollet et al. [49] applied the iterative version to the Potts model and quantum *XY* model by using the worm (directed-loop) algorithm, which will be explained in Sect. 3.4.3.

As other approaches, Mira tried to modify the transition matrix by directly moving the probabilities from the diagonal elements to off diagonal elements [42, 43]. Green et al. thought a multi trial after rejections [25]. Chiang et al. investigated the asymptotic convergence rate in low-temperature limit [10]. Baldi et al. researched the convergence issue of lattice systems (Markov random fields) [4], and Frigessi et al. investigated the computational complexity of finite Markov random fields [22]. As a reinterpretation, Billera et al. showed a simple diagram of the Metropolis algorithm [8]. Moreover, for enhancement of negative correlation, Frigessi et al. considered an antithetic coupling of two Gibbs sampler chains [20]. Although some optimization approaches for the transition kernel have been proposed, they are based on the Metropolis algorithm or the Gibbs sampler and they do not seem to improve the efficiency drastically.

For the optimization of local transition matrix, it seems intuitively efficient to minimize the diagonal elements (we call them the rejection rates). Actually, even for a simple update case of finite number of candidates, the conventional methods fail to minimize the diagonal elements. We will present a new method that constructs a rejection-minimized transition matrix in the next section.

2.3 Geometric Allocation

In this section, we introduce a novel method that constructs a transition kernel by a geometric approach. This method can find solutions by applying a graphical procedure, *weight allocation*, instead of solving the detailed balance equation algebraically as before. Surprisingly, it is *always* possible to find a solution that minimizes the average rejection rate.

In the MCMC method, we update configuration (or state) variables locally and run over the whole system. Now, let us consider updating one discrete variable as an elementary process, e.g., flipping a single spin in the Ising or Potts models [63] as Fig. 2.2. Given an environmental configuration, we would have n candidates (including the current one) for the next configuration. The weight of each candidate configuration (or state) is given by w_i $(i = 1, \ldots, n)$, to which the equilibrium probability measure is proportional. Although the total and detailed balance are usually expressed in terms of the weights $\{w_i\}$ and the transition probabilities $\{p_{i \to j}\}$ from state i to j, it is more convenient to introduce a quantity $v_{ij} := w_i \, p_{i \to j}$, which corresponds to the amount of (raw) stochastic flow from state i to j. The law of probability conservation and the total balance are then expressed as

$$w_i = \sum_{j=1}^{n} v_{ij} \quad \forall i \tag{2.46}$$

$$w_j = \sum_{i=1}^{n} v_{ij} \quad \forall j, \tag{2.47}$$

respectively. The average rejection rate is written as

$$\sum_i v_{ii} / \sum_i w_i. \tag{2.48}$$

Also, it is straightforward to confirm that $\{v_{ij}\}$ satisfy

$$v_{ij} = \frac{1}{n-1} \min[w_i, w_j] \quad i \neq j \tag{2.49}$$

for the Metropolis algorithm with the flat proposal distribution, and

Fig. 2.2 Single spin (Elementary) update in the ferromagnetic Ising model and the weights of each configuration. The parameter β is an inverse temperature
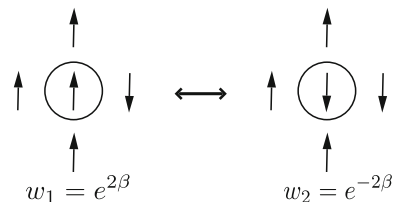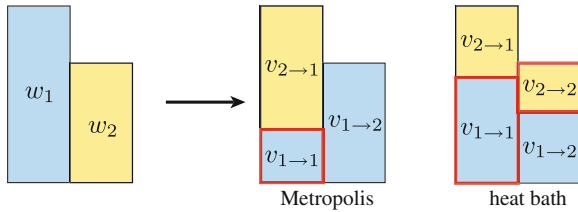
Fig. 2.3 Example of the weight allocation by the Metropolis and heat bath algorithms for $n = 2$. The regions with thick frame denote the rejection rates

$$v_{ij} = \frac{w_i w_j}{\sum_{k=1}^{n} w_k} \qquad \forall i, j \tag{2.50}$$

for the heat bath algorithm (Gibbs sampler), where the detailed balance, i.e., the absence of net stochastic flow, is manifested by the symmetry under the interchange of the indices:

$$v_{ij} = v_{ji} \qquad \forall i, j. \tag{2.51}$$

Our aim is to find a set $\{v_{ij}\}$ that minimizes the average rejection rate while satisfying Eqs. (2.46) and (2.47). The procedure for the task can be understood visually as *weight allocation*, where we move (or allocate) some amount of weight (v_{ij}) from state i to j keeping the entire shape of the weight boxes intact. For catching on this allocation picture, let us think at first the case with $n = 2$ as in the single spin update of the Ising model. Figure 2.3 shows the allocation when the Metropolis and heat bath algorithms are applied, where the average rejection rate ($\propto v_{11} + v_{22}$) clearly remains finite. Indeed, for $n = 2$ the Metropolis algorithm gives the best solution, i.e., the minimum average rejection rate even within the total balance (see Eq. (2.52)).

For $n \geq 3$, these two methods fail to minimize the rejection rate as we will mention. Besides, a generic method that accomplishes the minimization has not been known before. We will show that we can easily make it possible by this geometric picture. Although many optimal solutions are found actually, here we will introduce two specific algorithms. One makes a reversible kernel, and the other makes an *irreversible* kernel without the detailed balance.

2.3.1 Reversible Kernel

For describing our algorithm, let us introduce an operation named Swap:

```
Swap( i, j, w ) {
    v_ii ← v_ii − w
    v_ij ← v_ij + w
    v_ji ← v_ji + w
    v_jj ← v_jj − w
}.
```
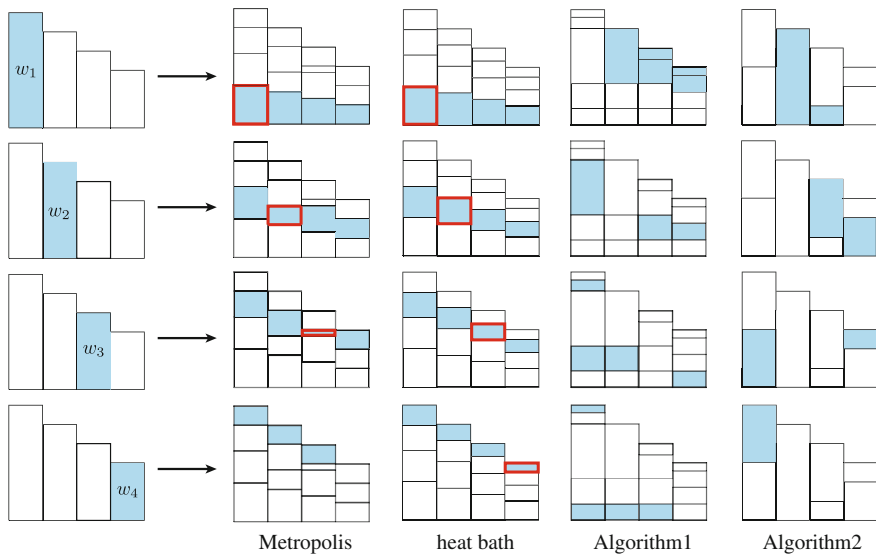
Fig. 2.4 Example of weight allocation by the Metropolis, the heat bath, and the proposed two algorithms for $n = 4$. Algorithm 1 constructs a reversible kernel, and Algorithm 2 does an irreversible kernel. Both proposed algorithms minimize the average rejection rate in general, and they are rejection free in this case while the conventional methods remain finite rejection rates as indicated by the thick frames

We note that if $\{v_{ij}\}$ satisfy the conditions (2.46), (2.47) and (2.51), this Swap operation does not break them. A certain algorithm for the construction of reversible kernel that minimizes the average rejection rate is described in Algorithm 1 [56]. This algorithm starts with the diagonal matrix $[v_{ij}]$ and uses only Swap operation for construction. Therefore the three conditions (2.46), (2.47) and (2.51) are automatically satisfied in the whole procedure. This algorithm can be depicted visually as Algorithm 1 in Fig. 2.4. As a result, the self-allocated weight that produces rejection is expressed as

$$v_{ii} = \begin{cases} \max(0, \ w_1 - \sum_{i=2}^{n} w_i) & i = 1 \\ 0 & i \geq 2. \end{cases} \tag{2.52}$$

That is, a rejection-free solution is obtained if the condition

$$w_1 \leq \frac{S_n}{2} \equiv \frac{1}{2} \sum_{k=1}^{n} w_k \tag{2.53}$$

is satisfied. When it is not satisfied, one has to necessarily assign the maximum weight to itself since it is larger than the sum of the rest. Thus, the present solution is optimal in the sense that it minimizes the average rejection rate.

2.3.2 Irreversible Kernel

Next, we show another algorithm that constructs an irreversible kernel [54]. Since the invention by Metropolis and the coworkers, the reversibility, the detailed balance, has been imposed to the Markov chain in most MCMC simulations. The reversibility is sufficient for the invariance of target distribution (sampling from the target distribution asymptotically). It is, however, *not necessary*. If it is possible to find a solution beyond the sufficient condition, further optimization can be achieved. In the meanwhile, it has long been considered difficult to satisfy the total balance without imposing the detailed balance. Thus attempts to optimizing transition probabilities have concentrated within the reversibility as we mentioned in the previous section [21, 34].

In fact, the reversibility is often broken secretly, even though the detailed balance is used apparently to define the transition probabilities. The single spin update in a classical system is such an example. The random update, where a spin to be flipped is chosen uniformly randomly among all spins, satisfies the detailed balance strictly.

Algorithm 1 Construction of Reversible Kernel with Minimized Rejection

---

Sort n candidate configurations as $w_1 \geq w_2 \geq w_3 \geq \cdots \geq w_n$ ($n \geq 3$).

$v_{ij} \leftarrow w_i \delta_{ij}$
$w_{\text{diff}} \leftarrow w_1 - w_2$
$S_3 \leftarrow \sum_{i=3}^{n} w_i$

if $w_{\text{diff}} \geq S_3$ **then**
    for $i = 2, ..., n$ **do**
        Swap($1, i, w_i$)   // v_{ii} becomes 0
    end for
else
    for $i = 3, ..., n$ **do**
        $v \leftarrow w_{\text{diff}} * w_i / S_3$
        Swap($1, i, v$)
    end for   // $v_{11} = v_{22} \geq v_{33} \geq \cdots \geq v_{nn}$
    for $j = n, ..., 2$ **do**
        $v' \leftarrow v_{jj}/(j-1)$
        for $k = j-1, ..., 1$ **do**
            Swap(j, k, v')
        end for   // $v_{11} = v_{22} \geq \cdots \geq v_{j-1,j-1}$ and $v_{jj} = 0$
    end for
end if

On the other hand, the reversibility is broken in the sequential update, where spins are swept in a fixed order. The detailed balance is satisfied only locally, that is, only in each spin flip, and the total balance is eventually fulfilled in one sweep [39].

In this subsection, we present another geometric algorithm that fulfills the total balance but breaks the detailed balance even locally. Furthermore, breaking the detailed balance introduces a net stochastic flow in the configuration space. It will boost up the convergence further by suppressing random walk behavior [1, 13, 15].[5]

Our approach is the first method that can generally satisfy the total balance without the detailed balance. Although a solution is not unique obviously, we propose the following procedure as a concrete algorithm to find a solution for general n.

  (i) Choose a configuration with maximum weight. If two or more configurations have the same maximum weight, choose one of them. In the following, we assume w_1 is the maximum without loss of generality. The order of the remaining weights does not matter.
 (ii) Allocate the maximum weight w_1 to the next box ($i = 2$). If the weight still remains after saturating the box, reallocate the remainder to the next ($i = 3$). Continue until the weight is all allocated.
(iii) Allocate the weight of the first landfilled box (w_2) to the last partially filled box in step (ii). Continue the allocation likewise.
 (iv) Repeat step (iii) for $w_3, w_4, \ldots, w_n$. Once all the boxes with $i \geq 2$ are saturated, landfill the first box ($i = 1$) afterward.

The whole algorithm is described in Algorithm 2. In the algorithm, if two or more configurations have the same maximum weight, choose one of them at first. Any order of configurations accomplishes the same minimized rejection rate. In the above procedure, all the boxes are filled without any space as well as the reversible case, as in Fig. 2.4; it satisfies the two conditions (2.46) and (2.47). However, the reversibility (2.51) is broken. (For example, $v_{12} > 0$, but $v_{21} = 0$ as depicted in the figure.) Since w_1 is the maximum, it is also clear that the second and subsequent boxes must be already saturated when the allocation of its own weight is initiated.

By this procedure, $\{v_{i \to j}\}$ are determined as

$$v_{i \to j} = \max(0, \, \min(\Delta_{ij}, \, w_i + w_j - \Delta_{ij}, \, w_i, \, w_j)), \qquad (2.54)$$

where

$$\Delta_{ij} := S_i - S_{j-1} + w_1 \qquad 1 \leq i, \, j \leq n \qquad (2.55)$$

$$S_i := \sum_{k=1}^{i} w_k \qquad 1 \leq i \leq n \qquad (2.56)$$

$$S_0 := S_n. \qquad (2.57)$$

---

[5] The overrelaxation method [1] and the hybrid Monte Carlo [15] both satisfy the detailed balance, mistakenly believed to break it.

Algorithm 2 Construction of Irreversible Kernel with Minimized Rejection

---

Choose a configuration that has the maximum weight and number it 1.
Sort other configurations in an arbitrary order.
$i \leftarrow 1$
$j \leftarrow 2$
while $i \leq n$ **do**
   $w_r \leftarrow w_i$
   while $w_r > 0$ **do**
      if $w_r \geq w_j$ **then**
         $v_{ij} \leftarrow w_j$
         $w_r \leftarrow w_r - w_j$
         if $j = n$ **then**
            $j \leftarrow 1$
         else
            $j \leftarrow j + 1$
         end if
      else
         $v_{ij} \leftarrow w_r$
         $w_j \leftarrow w_j - w_r$
         $w_r \leftarrow 0$
      end if
   end while
   $i \leftarrow i + 1$
end while

It is easy to understand from Eq. (2.54) that the rejection flow is expressed as the same Eq. (2.52) with Algorithm 1. In contrast to the reversible case, a net stochastic flow is introduced as the result of breaking the detailed balance, and it is expected to further boost up the sampling efficiency [13].

We close the introduction of our algorithm with a note about the ergodicity. Our new algorithms both minimize the average rejection rate; they are methods of choice. One hand, it is difficult to prove that the present irreversible kernel satisfies the ergodicity in the sequential update since many of the transition probabilities become zero. On the other hand, our reversible kernel can be ergodic almost as likely as the heat bath algorithm because the transition probabilities to other states except the current one are all positive. Since it is quite easy to prove the ergodicity of Markov chain by the heat bath algorithm, this reversible version must be ergodic in almost every cases. As we mentioned, the net stochastic flow in state space will boost the convergence; the irreversible version will be better than the reversible one. Thus, it is a good strategy to first check the ergodicity of the irreversible chain by comparing to the reversible chain and then use the irreversible one basically. Another way to ensure the ergodicity in the irreversible version is to randomly choose one of the probability sets obtained by different allocation order. Although we have not observed any glimpse of ergodicity breaking in the following simulations, such a prescription will assure users of the ergodicity.

2.4 Benchmarks in Potts Model

In order to assess the effectiveness of the present algorithms, we investigate the convergence and the autocorrelations in the ferromagnetic q-state Potts models on the square lattice [63]; the local (spin) state is expressed as σ_k that takes an integer $(1 \leq \sigma_k \leq q)$. These systems exhibit a continuous $(q \leq 4)$ or first-order $(q > 4)$ phase transition at $T4 = 1/\ln(1 + \sqrt{q})$. We calculate the square of order parameter (structure factor) for $q = 4$ and 8 by several algorithms. The order parameter [64], which is one of the most important quantity in statistical mechanical models, is defined as

$$O = \frac{q-1}{q} \parallel m \parallel_2^2, \tag{2.58}$$

where

$$m = (m_1, m_2, \ldots, m_q) \tag{2.59}$$

$$m_i = \frac{1}{L^d(q-1)} \left\langle \sum_k (q\, \delta_{i,\sigma_k} - 1) \right\rangle \quad 1 \leq i \leq q,$$

in the Potts model.

The order parameter equilibration (convergence) is shown in Fig. 2.5, where the simulation starts with the fully ordered state and the local variables are sequentially updated by the several algorithms. The square lattice with $L = 32$ and the critical temperature $T = 0.9102392266$ are used. The Metropolis algorithm (2.11) [40], the heat bath algorithm (2.12) [5], the Metropolized Gibbs sampler (2.24) [34, 35], the itera-

Fig. 2.5 Convergence of the order parameter (square root of the structure factor) in the ferromagnetic 4-state Potts model on the *square* lattice with $L = 32$ at the critical temperature. The *horizontal axis* is the Monte Carlo step. The simulation starts with the ordered (all "up") state. Our rejection-minimized samplers achieve the fastest convergence. There is no difference, in this scale, of two data by the reversible and irreversible kernel (That is why only one data is plotted)
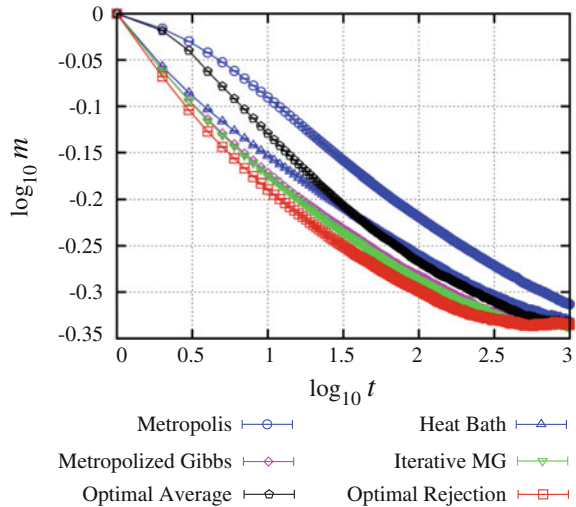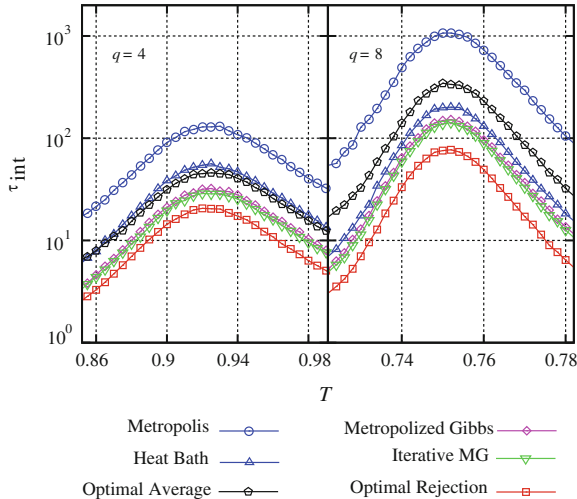
Fig. 2.6 Autocorrelation time of the square of order parameter near the transition temperature ($T \simeq 0.910$ and 0.745, respectively) in the 4-state (*left*) and 8-state (*right*) Potts models by several methods. The system size is 16×16. In the both cases, the present methods realize the shortest autocorrelation time. The error bars are the same order with the point sizes

tive Metropolized Gibbs sampler (2.33) [21], the optimal average sampler (2.44) [30], our rejection-minimized algorithms, Algorithm 1 [56] and Algorithm 2 (2.54) [54], are compared. Our samplers accomplish the fastest convergence of the quantity (square root of the structure factor). The two reversible and irreversible kernel perform equally. This acceleration implies that locally rejection-minimized algorithms reduce the second largest eigenvalue of the whole transition matrix in absolute value, which real part is presumably positive expected from the overdamping form.

In Fig. 2.6, on the other hand, it is clearly seen that our algorithms significantly reduce the autocorrelation time for $q = 4, 8$ in comparison with the conventional methods. The autocorrelation time τ_{int} is estimated through the relation: $\sigma^2 \simeq (1 + 2\tau_{\text{int}})\sigma_0^2$, where σ_0^2 and σ^2 are the variances of the estimator without considering autocorrelation and with calculating correlation from the binned data using a bin size much larger than the τ_{int} [32]. In the 4 (8)-state Potts model, the autocorrelation time becomes nearly 6.4 (14) times as short as that by the Metropolis algorithm, 2.7 (2.6) times as short as the heat bath algorithm, and even 1.4 (1.8) times as short as the iterative Metropolized Gibbs sampler [21, 49], which was considered as one of the best solutions before our approach. The autocorrelations of our two algorithms are much the same both for $q = 4, 8$.

Next, we investigated the dynamical exponent of the autocorrelation time at the critical temperature. The system-size dependence of the autocorrelation for $q = 4$ is shown in Fig. 2.7. All the update methods suffer from the critical slowing down with the exponent $z \sim 2.3$. Unfortunately, the locally optimized method does not reduce

Fig. 2.7 System-size dependence of the autocorrelation time for $q = 4$ at the critical temperature. The dynamics of all update methods experiences the critical slowing down with the dynamical exponent $z \sim 2.3$. Although the local optimization does not improve the exponent, the rejection-minimized samplers get always factor over 6, compared with the Metropolis algorithm
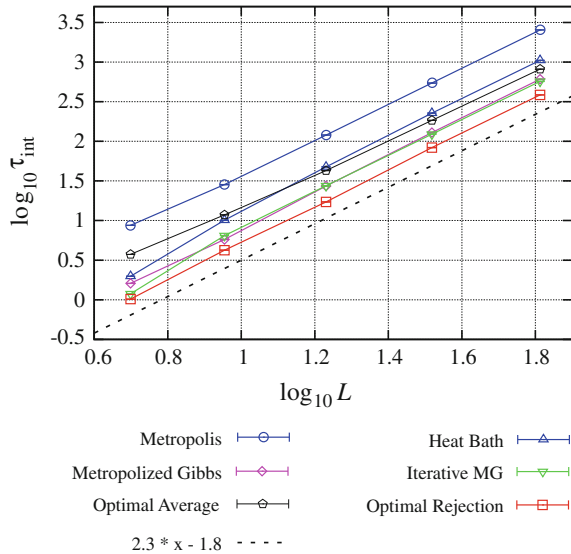
the exponent. The factor, however, over 6 is always gained against the Metropolis algorithm.

As we have seen, our rejection-minimized samplers boost the convergence and reduce the autocorrelation time of the relevant estimator (order parameter). The present methods will be effective in not only the Potts model but also the many kinds of systems. A further eigenvalue analysis is important. Particularly, modifications of the above theorems for irreversible kernels are greatly of interest.

2.5 Bounce-Free Worm (Directed-Loop) Algorithm

Next, we will move onto the quantum Monte Carlo (QMC) method. Although we will explain the detailed formalism of the QMC method with new modifications in the next chapter, here let us see an example of the kernel optimization in the QMC method.

The worm algorithm for quantum spin and lattice boson models is formulated based on either the Euclidean path integral or the high-temperature series [50, 58]. One Monte Carlo sweep of the worm algorithm consists of the diagonal update, where operators are inserted or removed without changing the shape of worldlines, and the off-diagonal update, where the worldlines (and the type of operators) are updated with keeping the position of operators unchanged. In the latter process, a pair of creation and annihilation operators, which is called a worm, is inserted on a worldline (pair creation), and one of them (called the head) is moved stochastically until the head and the tail destroy each other (pair annihilation). As a thorny problem,
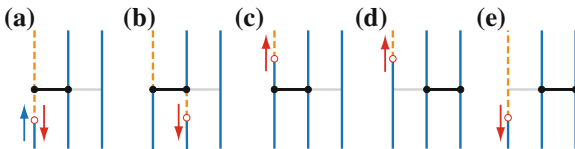
Fig. 2.8 Extension of the worm-going pathway in the $S = 1/2$ model. Here, *dashed* (*solid*) *vertical lines* denote spin up (*down*). The head of worm (*open circle*) moves on the worldline (**a**), and scatters at the operator (*horizontal thick line*). As candidate configurations, we introduce operator-flip updates (**d**), (**e**) in addition to the conventional ones (**a**)–(**c**). Note that in (**e**) the position of the operator is shifted simultaneously in contrast to the simple bounce process (**a**)

a bounce process, where the head just backtracks and cancels the last update, has been generally inevitable within the detailed balance. Here, as an example, we consider the $S = 1/2$ antiferromagnetic *XXZ* model:

$$\mathcal{H} = \sum_{<i,j>} \left(S_i^x S_j^x + S_i^y S_j^y + \Delta S_i^z S_j^z - C \right) - h \sum_i S_i^z, \qquad (2.60)$$

where we introduce a parameter C controlling the ratio between the diagonal and off-diagonal weights. In the head scattering process at an operator, only three among four exits have a nonzero weight due to the conservation of the total S^z (Fig. 2.8a–c). At the Heisenberg point ($\Delta = 1$), there remain finite bounce probabilities except at $h = 0$ within the detailed balance [2, 49, 58]. Unfortunately, the situation does not improve much even in the total balance because the number of candidates is too small. However, the condition (2.53) provides us a clear prospect; by increasing the number of candidates, a bounce-free algorithm will be realized. According to this strategy, we introduce an *operator-flip* update, where sites on which an operator acts are shifted simultaneously (Fig. 2.8). By the operator flip together with the constant C chosen as

$$C = \max \left(\frac{1}{4}(2\Delta + 3h - 1), \ \frac{1}{8}(\Delta + 3h + 1) \right), \qquad (2.61)$$

we can indeed eliminate the bounce process.

The autocorrelation data of the magnetization in the Heisenberg chain ($\Delta = 1$) are shown in Fig. 2.9. Amazingly, the bounce-free worm algorithm with the operator flip is faster by about 2 orders of magnitude than the Metropolis and the heat bath algorithms. In this model, our irreversible kernel is nearly 3 times as fast as our reversible kernel; the net stochastic flow effectively works in this case. Also in high-S spin systems, the bounce-free worms can be constructed by having the head hold the matrix element of the ladder operator or by representing the partition function of general S system as that of decomposed $S = 1/2$ spin system [60]. Our idea of breaking the detailed balance and operator-flip updates are also applied to general bosonic models and the efficiency is improved because bosonic worms get
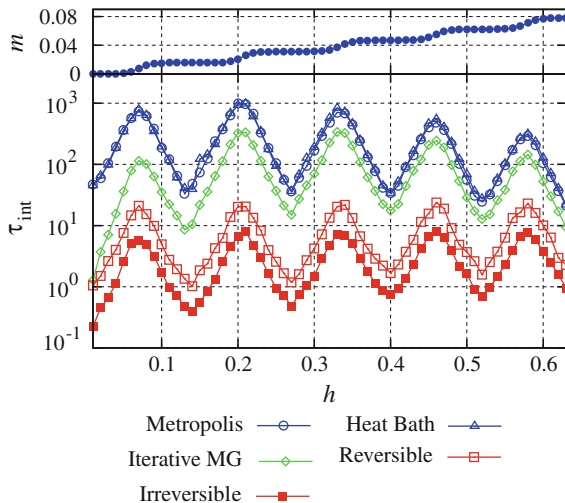
Fig. 2.9 Magnetic field dependence of magnetization (*upper*) and autocorrelation time (*lower*) of the $S = 1/2$ antiferromagnetic Heisenberg chain ($L = 64$, $T = 1/2L$). The maximum autocorrelation time is 1.0×10^3 by the worm update with Metropolis (*circles*), 9.8×10^2 by the worm with heat bath (*triangles*), and 3.3×10^2 by the iterative Metropolized Gibbs sampler (*diamonds*). By the bounce-free worm with the operator flip, τ_{int} is further reduced down to 23.8 (*open squares*) for the reversible version and 8.1 (*solid squares*) for the irreversible version

bounce-minimized with more candidates. This application is very important also for our calculation of spin-Peierls models in the following chapters.

2.6 General Construction of Irreversible Kernel

We will mention also new methods constructing improved kernel for general state space that is not finite. Let us consider updating a continuous variable here. When the inversion method is applicable, the variable is updated by the heat bath algorithm (Gibbs sampler) usually. That is, the next state is determined from a uniformly random variable $r \in [0, 1]$ on conditional cumulative distribution. The calculation of the inverse function is needed in this procedure. On the other hand, when the inversion method cannot be applied, a candidate state is chosen from a proposal distribution and accepted/rejected by the Metropolis algorithm usually. In this situation, where we are in most cases, the inevitable rejection will be a bottleneck for sampling. For continuous variables, it is not possible to apply directly the previous allocation algorithm because the measure of each state is zero. We can, nevertheless, improve the efficiency for both cases by extending the idea of breaking the detailed balance.

2.6.1 Beyond Heat Bath Algorithm

First, we introduce an improved sampling that is an alternative method to the Gibbs sampler. Let us review our allocation algorithm for the irreversible kernel for finite-size problems. We start at the configuration with the maximum weight and allocate the weight to the next. This procedure can be also represented by shifting each position in the maximum weight on the cumulative distribution. We compare the shifted distribution to the original (non-shifted) one as Fig. 2.10 and assign the next position (state). It is possible to set the amount of shift any value. If there is a self-allocation as a result of the shift, the amount is nothing but the rejection rate. It is obvious that the amount of shift that can avoid the self-allocation is not unique; the rejection-free kernel can be achieved as long as the amount of shift is such that the maximum weight has no overlap with its original position as in the figure. For continuous variables, we can set the start point of allocation (the amount of shift) at our disposal. Let us consider the bivariate Gaussian distribution as a simple example:

$$P(x_1, x_2) \propto e^{-\frac{(x_1 - x_2)^2}{2\sigma_1^2} - \frac{(x_1 + x_2)^2}{2\sigma_2^2}}. \tag{2.62}$$

Given x_2, x_1 is updated by using the conditional cumulative distribution

$$F(x_1|x_2) = \int_{-\infty}^{x_1} P(x, x_2)dx. \tag{2.63}$$

The heat bath algorithm determines the next state as

$$x_1' = F^{-1}(r), \tag{2.64}$$

where $r \in [0, 1]$ is an uniformly (pseudo) random variable. This process satisfies the detailed balance.

The overrelaxation method has been known as one of the best ways to update the Gaussian variables. The name "overrelaxation" comes from an idea to make the

Fig. 2.10 Picture of the cumulative distribution shifts. The algorithm for the irreversible kernel is corresponding to the shift in the maximum weight as shown in the midst. If we shift in a larger value, we could get a rejection free algorithm as in the *right* bar
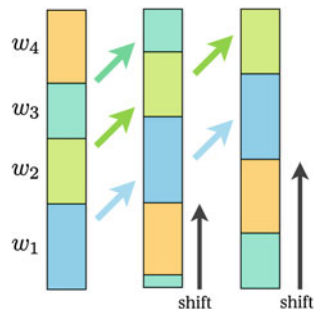
Markov chain to have negative correlation. We have already seen that the negative eigenvalues, which results in the negative correlation, make the asymptotic variance smaller and the sampling more efficient. This method was first proposed by Adler [1] for updating variables with a Gaussian conditional distribution. Whitmer [62] discussed slightly an extended application range of the method. In the overrelaxation method, for generation of a variable from a conditional distribution

$$P(z_i|\cdot) \sim N(\mu_i, \sigma_i^2), \tag{2.65}$$

the next state is chosen as

$$z_i' = \mu_i + \alpha(z_i - \mu_i) + \sigma_i\sqrt{1 - \alpha^2}\nu, \tag{2.66}$$

where ν is a random variable generated from $N(0, 1)$ and α is a parameter with $-1 < \alpha < 1$. Later, Brown et al. [9] and Creutz [12] applied the idea of generating negative correlation to the SU(2) and SU(3) gauge theory, mapping the state space into an Euclidean space where the distribution can be described by the Gaussian distribution. Mira et al. rediscovered the overrelaxation method [44] in statistics. Moreover, this overrelaxation technique can be used for not only the Gaussian but some simple distributions, e.g., the conditional distribution of the classical *XY* model or the Heisenberg model. The main idea is to try to go to the opposite side over the center of the conditional distribution under the detailed balance. Thus, we need to know where the center is. This condition hinders us from applying the method to general cases. As an approach for general models, Neal [46] proposed the ordered overrelaxation where some candidates are generated from the conditional distribution and ordered, then we go to approximately opposite side through the order of states. This method, however, still needs to generate configurations from the conditional distribution. Thereby, the application range is not so extended practically.

Now, as an another update method [55], let us choose the next state as

$$x_1' = F^{-1}(\{F(x_1|x_2) + c + wu\}), \tag{2.67}$$

where x_1 is the current state, c and w is a positive real parameter with $c \geq w$, and u is an uniformly random variable in $[-1, 1]$, respectively. The symbol $\{a\}$ takes the fractional portion of a real number a. If we use $c = w = 1/2$, this process is nothing but the heat bath algorithm. On the other hand, when $c \neq 0, 1/2$, it does not satisfy the detailed balance and there is a net stochastic flow. This flow can push the configuration globally as in Fig. 2.11. As the result, the autocorrelation time of $(x_1 + x_2)^2$ is significantly reduced as shown in Fig. 2.12. In this figure, the overrelaxation methods and the ordered overrelaxation method are also tested. Compared with the conventional methods, the present update method can be better on the whole parameter region; at any ratio σ_2/σ_1, there is a better parameter set of present scheme than the best parameter of the overrelaxation or the ordered overrelaxation methods. Figure 2.12 shows the results by using the heat bath algorithm, the overrelaxation method with $\alpha = -0.86$, the ordered overrelaxation with the number of candidates
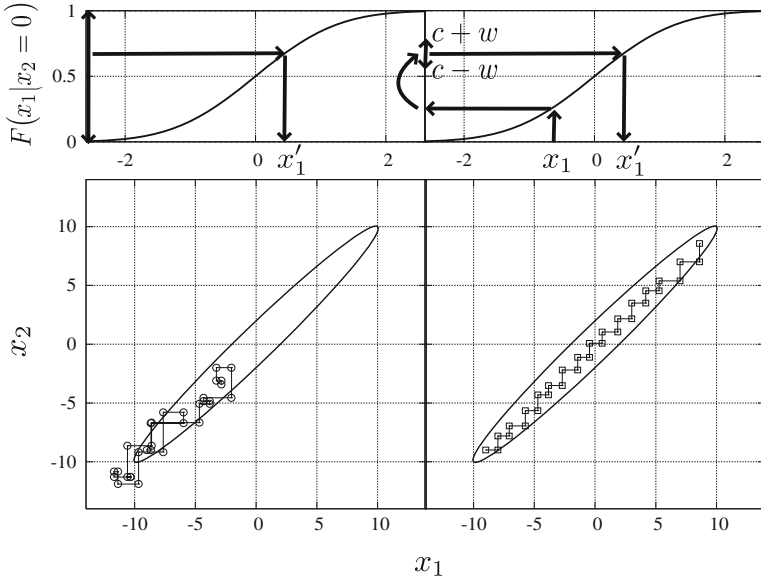
Fig. 2.11 Trajectories of configurations updated by the heat bath algorithm (*left*) and by the present irreversible algorithm with $c = 0.4$ and $w = 0.1$ (*right*) in the bivariate Gaussian distribution with $\sigma_1 = 1$ and $\sigma_2 = 10$. The ellipsoidal line is the three-sigma line of the Gaussian distribution. The *upper* figures show the update procedures of each algorithm

Fig. 2.12 Autocorrelation times of $(x_1 + x_2)^2$ in the bivariate Gaussian distribution by using the heat bath algorithm (*triangles*), the overrelaxation (*circles*) 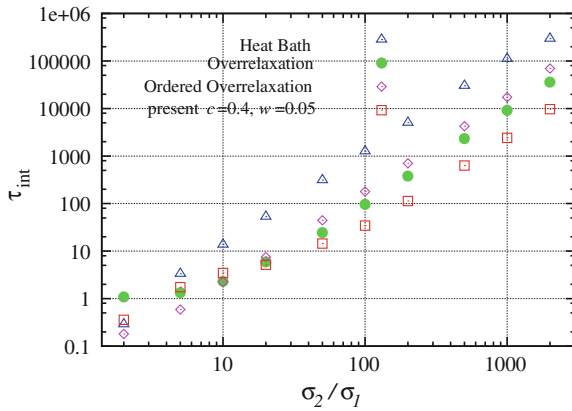with $\alpha = -0.86$, the ordered overrelaxation (*diamonds*) with the number of candidates 10, and the present method with $c = 0.4$ and $w = 0.05$ (*squares*). The horizontal axis σ_2/σ_1 is corresponding to the sampling difficulty

10, and the present algorithm with $c = 0.4$ and $w = 0.05$. The present method produces the shortest correlation time over $\sigma_2/\sigma_1 \geq 50$ and achieves about 50 times as short correlation time as the heat bath algorithm in the region. As we mentioned, we can surely find a better parameter set of the present algorithm than the best parameter of the conventional overrelaxation methods in the whole region.

2.6.2 Beyond Metropolis Algorithm

We will explain here it is possible to significantly reduce the rejection rate for general cases. When the direct inversion method as in the previous subsection cannot be applied, we resort to the Metropolis algorithm usually, where a candidate is generated and the update trial is accept/reject according to the weight ratio. The Metropolis algorithm is very simple and easy to implement. It has been a canonical algorithm for the MCMC method since the invention in 1953 [40]. However, the inevitable rejection often obstructs the efficient sampling. Obviously it is important to reduce the rejection rate. When the number of candidates is two, the Metropolis algorithm achieves the minimized rejection rate that is easily proved by the geometric picture we introduced in Sect. 2.3. On the other hand, the Barker algorithm, which is nothing but the heat bath algorithm for two candidates, has more rejection. Therefore, in order to reduce the rejection rate, we have to prepare more candidates than two. As an alternative to the simple Metropolis algorithm, some methods have been proposed so far. An example is the multipoint Metropolis methods, where after generating some candidate states the next configuration is stochastically chosen with the detailed balance kept. See references Frenkel et al. [19], Liu et al. [37], Qin et al. [51], and Liu [36]. Another example is the window algorithm proposed by Neal [45]. This is a variant of the multipoint Metropolis methods for the hybrid Monte Carlo method [15].

We can apply our rejection-minimized algorithms after creating some candidate states. Let us consider sampling from the wine-bottle (Mexican-hat) potential:

$$P(x_1, x_2) \propto \exp\left(-\left(\frac{(x_1 - x_2)^2}{2\sigma_1^2} + \frac{(x_1 + x_2)^2}{2\sigma_2^2}\right)\left(\frac{(x_1 - x_2)^2}{2\sigma_1^2} + \frac{(x_1 + x_2)^2}{2\sigma_2^2} - h\right) + \frac{h^2}{4}\right). \tag{2.68}$$

The example of the potential is shown in Fig. 2.13. We propose a candidate configuration by the isotropic bivariate Gaussian distribution $\propto \exp(-(\Delta x_1)^2 - (\Delta x_2)^2)$. Here, we try to make some proposals. If we propose candidates from the current position and naively make a transition matrix (probability) taking into account only the weights, the total balance is broken. It is because we have to consider also the different proposal probability. Avoiding this difficult task, we use the following strategy:

1. A configuration is chosen as a hub from the current configuration by a proposal distribution.
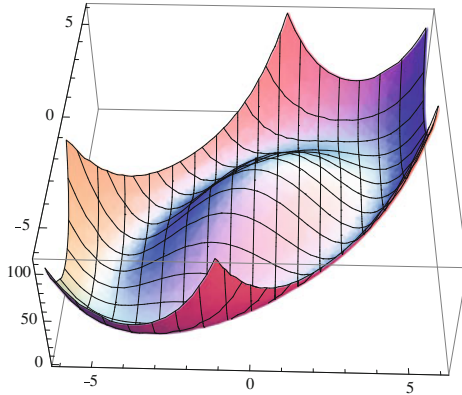
Fig. 2.13 Wine-bottle (Mexican-hat) potential for $\sigma_1 = 1, \sigma_2 = 2, h = 16$

2. Candidates are generated by using the same proposal distribution with process 1 from the hub.
3. The next state is chosen among the candidates and the current configuration by using the transition probabilities taking into account only the weights of the states.

This procedure is depicted as in Fig. 2.14. In the process 3, we can make the rejection rate minimized by applying our algorithms we introduced. Figure 2.15 shows that the rejection rate is indeed reduced by using this multi-proposal algorithm and the irreversible kernel. The correlation time of $(x_1 + x_2)^2$ also gets shorter as the number of candidates is increased. Although this example is a simple case, this procedure is applicable to any MCMC sampling. The further investigation of the validity is a future problem. These days, the role of the net stochastic flow (irreversible drift) has caught much attention [18, 29, 31]. The performance of our algorithm and the efficient flow structure need to be investigated further in the future.

Finally, we close this chapter with noting of the CPU time cost. As we mentioned in the introduction of the geometric allocation algorithms, there is no extra CPU time cost when we can prepare all transition probabilities before sampling. As for the continuous variables, it is not the case; we have to calculate probabilities at each

Fig. 2.14 Multi-proposal strategy for $n = 4$. At first, a center position is chosen from the current position x. Then, candidates x', x'', x''' are generated from the center. The *dot line* shows the 1 sigma line of the Gaussian distribution
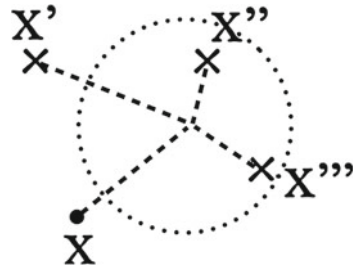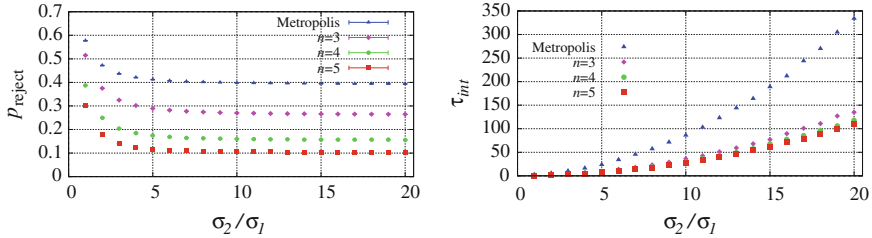
Fig. 2.15 Rejection rates (*left*) and the correlation times of $(x_1 + x_2)^2$ (*right*) by the simple Metropolis algorithm and the rejection-minimized method for $n = 3$ and $n = 4$. The rejection rate is definitely reduced as the number of candidates is increased. Accompanying the rejection rate, the correlation time gets shorter

transition. Although the rejection rate is certainly reduced by using the multi proposal strategy, meanwhile, the CPU time cost is increased. Thus, the question arises that the needed calculation time is truly decreased. Here, we mention a combination with parallelization method. The process of preparing candidates can be done independently. Thus, we can control the CPU time by applying the parallelization for the multi proposal. This multi-core update scheme is effective especially for the cases where the long thermalization (convergence) time is needed by a simple single core update. The effectiveness of this combination method needs to be researched.

References

1. Adler, S. L. (1981). Over-relaxation method for the Monte Carlo evaluation of the partition function for multiquadratic actions. *Physical Review D*, *23*, 2901.
2. Alet, F., Wessel, S., & Troyer, M. (2005). Generalized directed loop method for quantum Monte Carlo simulations. *Physical Review E*, *71*, 036706. doi:10.1103/PhysRevE.71.036706.
3. Andrieu, C., & Toms, J. (2008). A tutorial on adaptive MCMC. *Statistics and Computing*, *18*, 343–373.
4. Baldi, P., Frigessi, A., & Piccioni, M. (1993). Importance sampling for Gibbs random fields. *Annals of Applied Probability*, *3*, 914–933.
5. Barker, A. A. (1965). Monte Carlo calculations of the radial distribution functions for a proton-electron plasma. *Australian Journal of Physics*, *18*, 119.
6. Bellman, R. E. (1957). *Dynamic programming*. Princeton: Princeton University Press.
7. Berg, B. A., & Neuhaus, T. (1992). Multicanonical ensemble: A new approach to simulate first-order phase transitions. *Physical Review Letters*, *68*, 9.
8. Billera Louis, J., & Diaconis, P. (2001). A geometric interpretation of the Metropolis-Hastings algorithm. *Statistical Science*, *16*, 335–339.
9. Brown, F. R., & Woch, T. J. (1987). Overrelaxed heat-bath and Metropolis algorithms for accelerating pure gauge Monte Carlo calculations. *Physical Review Letters*, *58*, 2394–2395.
10. Chiang, T. S., & Chow, Y. (1993). Asymptotic behavior of eigenvalues and random updating shemes. *Applied Mathematics and Optimization*, *28*, 259–275.
11. Creutz, M. (1980). Monte Carlo study of quantized SU(2) gauge theory. *Physical Review D*, *21*, 2308.

12. Creutz, M. (1987). Overrelaxation and Monte Carlo simulation. *Physical Review D*, *36*, 515–519.
13. Diaconis, P., Holmes, S., & Neal, R. M. (2000). Analysis of a nonreversible Markov chain sampler. *Annals of Applied Probability*, *10*, 726.
14. Dick, J., & Pillichshammer, F. (2010). *Digital nets and sequences: Discrepancy theory and Quasi Monte Carlo integration*. Cambridge: Cambridge University Press.
15. Duane, S., Kennedy, A. D., Pendleton, B. J., & Roweth, D. (1987). Hybrid Monte Carlo. *Physics Letters B*, *195*, 216.
16. Evertz, H. G., Lana, G., & Marcu, M. (1993). Cluster algorithm for vertex models. *Physical Review Letters*, *70*, 875.
17. Faure, H. (1982). Discrépance de suites associées à un systéme de numération (en dimension s). *Acta Arithmetica*, *41*, 337–351.
18. Franke, B., Hwang, C. R., Pai, H. M., & Sheu, S. J. (2010). The behavior of the spectral gap under growing drift. *American Mathematical Society*, *362*, 1325–1350.
19. Frenkel, D., & Smit, B. (2001). *Understanding molecular simulation: From algorithms to applications* (2nd ed.). San Diego: Academic Press.
20. Frigessi, A., Gåsemayr, J., & Rue, H. (2000). Antithetic coupling of two Gibbs sampler chains. *Annals of Statistics*, *28*, 1128–1149.
21. Frigessi, A., Hwang, C. R., & Younes, L. (1992). Optimal spectral structure of reversible stochastic matrices, Monte Carlo methods and the simulation of Markov random fields. *Annals of Applied Probability*, *2*, 610–628.
22. Frigessi, A., Martinelli, F., & Stander, J. (1997). Computational complexity of Markov chain Monte Carlo methods for finite Markov random fields. *Biometrika*, *84*, 1–18.
23. Geman, S., & Geman, D. (1984). Stochastic relaxation, Gibbs distributions and the Bayesian restoration of images. *IEEE Transactions on Pattern Analysis and Machine Intelligence*, *6*, 721.
24. Gilks, W. R., Richardson, S., & Spiegelhalter, D. J. (1996). *Markov Chain Monte Carlo in Practice*. London/New York: Chapman & Hall.
25. Green, P. J., & Mira, A. (2001). Delayed rejection in reversible jump Metropolis-Hastings. *Biometrika*, *88*, 1035–1053.
26. Hastings, W. K. (1970). Monte Carlo sampling methods using Markov chains and their applications. *Biometrika*, *57*, 97.
27. Hlawka, E. (1961). Funktionen von beschränkter variation in der theorie der gleichverteilung. *Annali di Matematica Pura ed Applicata*, *54*, 325–333.
28. Hukushima, K., & Nemoto, K. (1996). Exchange Monte Carlo method and application to spin glass simulations. *Journal of the Physical Society of Japan*, *65*, 1604.
29. Hwang, C. R. (2006). Nonreversible perturbations accelerate convergence. *RIMS Kokyuroku*, *1462*, 26–34.
30. Hwang, C. R., Chen, T. L., Chen, W. K., & Pai, H. M. (2012). On the optimal transition matrix for MCMC sampling. *SIAM Journal on Control and Optimization*, *50, 2743–2762.*
31. Hwang, C. R., Hwang-Ma, S. Y., & Sheu, S. J. (2005). Accelerating diffusions. *Annals of Applied Probability*, *15*, 1433–1444.
32. Landau, D. P., & Binder, K. (2005). *A guide to Monte Carlo simulations in statistical physics* (2nd ed.). Cambridge: Cambridge University Press.
33. Lemieux, C. (2009). *Monte Carlo and Quasi-Monte Carlo sampling*. New York: Springer.
34. Liu, J. S. (1996). Metropolized independent sampling with comparisons to rejection sampling and importance sampling. *Statistics and Computing*, *6*, 113.
35. Liu, J. S. (1996). Peskun's theorem and a modified discrete-state Gibbs sampler. *Biometrika*, *83*, 681–682.
36. Liu, J. S. (2001). *Monte Carlo strategies in scientific computing* (1st ed.). Springer: New York.
37. Liu, J. S., Liang, F., & Wong Wing, H. (2000). The multiple-try method and local optimization in Metropolis sampling. *Journal of the American Statistical Association*, *95*, 121.
38. Loison, D., Qin, C. L., Schotte, K. D., & Jin, X. F. (2004). Canonical local algorithms for spin systems: Heat bath and Hasting's methods. *European Physical Journal B*, *41*, 395–412.

39. Manousiouthakis, V. I., & Deem, M. W. (1999). Strict detailed balance is unnecessary in Monte Carlo simulation. *Journal of Chemical Physics*, *110*, 2753.
40. Metropolis, N., Rosenbluth, A. W., Rosenbluth, M. N., Teller, A. H., & Teller, E. (1953). Equation of state calculations by fast computing machines. *Journal of Chemical Physics*, *21*, 1087.
41. Meyn, S. P., & Tweedie, R. L. (1993). *Markov chains and stochastic stability*. New York: Springer.
42. Mira, A. (2001). Ordering and improving the performance of Monte Carlo Markov chains. *Statistical Science*, *16*, 340–350.
43. Mira, A. (2006). Stationarity preserving and efficiency increasing probability mass transfers made possible. *Computational Statistics*, *21*, 509–522.
44. Mira, A., & Sargent Daniel, J. (2003). A new strategy for speeding Markov chain Monte Carlo algorithms. *Statistical Methods and Applications*, *12*, 49–60.
45. Neal, R. M. (1994). An improved acceptance procedure for the hybrid Monte Carlo algorithm. *Journal of Computational Physics*, *111*, 194–203.
46. Neal, R. M. (1999). Suppressing random walks in Markov chain Monte Carlo using ordered overrelaxation. In M. I. Jordan (Ed.), *Learning in graphical models* (pp. 205–228). Cambridge: MIT Press.
47. Niederreiter, H. (1988). Low-discrepancy and low-dispersion sequences. *Journal of Number Theory*, *30*, 51–70.
48. Peskun, P. H. (1973). Optimum Monte Carlo sampling using Markov chains. *Biometrika*, *60*, 607.
49. Pollet, L., Rombouts, S. M. A., Van Houcke, K., & Heyde, K. (2004). Optimal Monte Carlo updating. *Physical Review E*, *70*, 056705.
50. Prokof'ev, N. V., Svistunov, B. V., & Tupitsyn, I. S. (1998). Exact, complete, and universal continuous-time world-line Monte Carlo approach to the statistics of discrete quantum systems. *Soviet Physics JETP*, *87*, 310.
51. Qin, Z. S., & Liu, J. S. (2001). Multipoint Metropolis method with application to hybrid Monte Carlo. *Journal of Computational Physics*, *172*, 827.
52. Robert, C. P., & Casella, G. (2004). *Monte Carlo statistical methods* (2nd ed.). New York: Springer.
53. Sobol, I. M. (1967). Distribution of points in a cube and approximate evaluation of integrals. *Žrnal Vyčislitel'noi Matematiki i Matematicheskoi Fiziki*, *7*, 784–802.
54. Suwa, H., & Todo, S. (2010). Markov chain Monte Carlo method without detailed balance. *Physical Review Letters*, *105*, 120603.
55. Suwa, H., & Todo, S. (2011). *Butsuri*, *66*, 370 (in Japanese).
56. Suwa, H., & Todo, S. (2012). Geometric allocation approach for transition kernel of Markov chain. In *Monte Carlo methods and applications*, (pp. 213–221). Berlin: De Gruyter.
57. Swendsen, R. H., & Wang, J. S. (1987). Nonuniversal critical dynamics in Monte Carlo simulations. *Physical Review Letters*, *58*, 86.
58. Syljuasen, O. F., & Sandvik, A. W. (2002). Quantum Monte Carlo with directed loops. *Physical Review E*, *66*, 046701.
59. Tierney, L. (1994). Markov chain for exploring posterior distributions. *Annals of Statistics*, *22*, 1701.
60. Todo, S., & Kato, K. (2001). Cluster algorithms for general-*S* quantum spin systems. *Physical Review Letters*, *87*, 047203.
61. Ulam, S., Richtmyer, R. D., & von Neumann, J. (1947). *Statistical methods in neutron diffusion*. Los Alamos, NM: Los Alamos Scientific Laboratory. (Report LAMS-551).
62. Whitmer, C. (1984). Over-relaxation methods for Monte Carlo simulations of quadratic and multiquadratic actions. *Physical Review D*, *29*, 306–311.
63. Wu, F. Y. (1982). The Potts model. *Reviews of Modern Physics*, *54*, 235.
64. Zheng, B. (1998). Monte Carlo simulations of short-time critical dynamics. *International Journal of Modern Physics B*, *12*, 1419.

Chapter 3
Monte Carlo Method for Spin-Peierls Systems

3.1 Developments of Quantum Monte Carlo

The quantum Monte Carlo (QMC) method that is based on the worldline representation have been applied to a wide variety of quantum spin and bosonic systems and established its value as a powerful numerical tool for investigating quantum critical phenomena [15]. Particularly in strongly correlated systems that it is essential to simulate on a large scale, the method has made a significant contribution to elucidate a lot of nontrivial quantum natures with unbiased results [3, 17]. The basic idea of the QMC method was devised by Handscomb [11] as early as 1962. A series expansion of the density-matrix operator $\exp(-\beta H)$ and importance sampling of the operator sequence was introduced. The application range, however, is restricted to a few models, such as the $S = 1/2$ ferromagnetic Heisenberg model. Another representation using the Trotter formula was invented by Suzuki [29], where a quantum system is mapped onto a classical system by the Feynman path integral with discretized imaginary time. The mapped state is called the worldline configuration and sampled by means of the Monte Carlo method. Although we can get correct results by extrapolating the discretization step of imaginary time to zero, it had been an artificial bottleneck that the convergence and sampling efficiency fatally dropped down as the discretization step is decreased.

One of the recent progresses of the QMC method was the elimination of the decomposition error. Beard et al. [1] showed that it is possible to simulate quantum systems directly in continuous time. Shortly later, the stochastic series expansion (SSE), which expresses the partition function as the high-temperature series, was proposed by Sandvik [25] as an another exact representation. In the meantime, the worldline update had consisted of local updates that had many drawbacks, e.g., the poor acceptance rate and the inability to change the winding number.

Another significant progress of the QMC method was the development of efficient nonlocal update methods, such as the loop algorithm [7] and the worm algorithm [22]. The loop algorithm, which is a quantum version of the Swendsen-Wang algorithm [30], performs a cluster update on the worldlines and reduces significantly

the dynamical exponent at critical temperature in some quantum spin systems, e.g., the Heisenberg model on bipartite lattices [6]. On the other hand, the worm algorithm proposed by Prokof'ev et al. [22] is more generally applicable than the loop algorithm, where a pair of the creation and annihilation operators, called the worm, is inserted and moved stochastically on the worldlines. These days, the directed-loop algorithm proposed by Syljuasen et al. [32], which is a variant of the worm algorithm, has become a standard method for quantum spin and bosonic systems.

In the meanwhile, the QMC method suffers from the negative sign problem for frustrated quantum spin models or fermionic models except half filling. For the one-dimensional spinless fermionic systems, in fact, the meron algorithm [3, 4] can greatly overcome the problem. The fermionic degree of freedom being traced out, the worldline configuration is the pure loop in the method. Then, the pure-loop configuration that has at least one "meron" that inverts the sign by flipping is ruled out for statistical averages. For spin systems, however, there has been no example where the meron algorithm works well except for the trivial cases so far. We will mention the first application of the algorithm to a quantum spin model with the twisted boundary condition in Sect. 4.4.

3.2 Difficulty of Conventional Methods

Although the QMC methods have performed well for many quantum systems, the conventional update methods cannot satisfy the ergodicity (irreducibility) for particle number nonconserving systems. When it is not trivial to find a good quantum number and basis set, it is inevitable to treat such nonconserved particles; the quantum number necessarily varies along the imaginary time axis. One of the relevant models is the frustrated transverse Ising model [13, 31] where the total S^z is not conserved in the Hamiltonian (Note that a cluster update can be performed only on bipartite lattices without frustration [24]). Another example is a spin-Peierls model:

$$H = \sum_r J(1 + \alpha q_r)S_{r+1} \cdot S_r + \frac{p_r^2}{2m} + \frac{c}{2}q_r^2$$

$$= \sum_r J\left(1 + \sqrt{\frac{\omega \lambda}{2}}(a_r + a_r^\dagger)\right)S_{r+1} \cdot S_r + \sum_r \omega\left(a_r^\dagger a_r + \frac{1}{2}\right), \quad (3.1)$$

where q_r and p_r are the coordinate and momentum operators at site r, m and c are the mass and the spring constant of the lattice degree of freedom, $a_r^\dagger$ and a_r are the creation and annihilation operators of boson (phonon), $J > 0$ (antiferromagnetic spin interaction), α is the spin-lattice coupling parameter, $\omega = \sqrt{c/m}$ is the excitation gap of dispersionless (Einstein) phonon, and $\lambda = \alpha^2/c$ is the spin-phonon coupling parameter, respectively. Here the lattice degree of freedom is transformed to a boson (phonon) by the second quantization:

$$q_r = \sqrt{\frac{1}{2m\omega}}(a_r^\dagger + a_r) \qquad (3.2)$$

$$p_r = i\sqrt{\frac{m\omega}{2}}(a_r^\dagger - a_r). \qquad (3.3)$$

Let us consider the one-dimensional $S = 1/2$ spin-Peierls model here, and we will extend this model to a dispersive case in two-dimensional systems in Chap. 6. The optical phonon is adequate for describing the physical property of $CuGeO_3$ as discussed in the references [10, 34].

In this Hamiltonian, the boson number is not conserved owing to the spin-phonon interaction. The spin-Peierls system exhibits the spin-Peierls transition that has been observed in experiments for organic and inorganic materials, e.g., TTF-CuBDT [2], $CuGeO_3$ [12, 33] and TiOCl [28], and has been investigated theoretically [5, 9] and numerically [20, 27] during several decades. Particularly, a quantum phase transition between a gapless spin-liquid phase and a quantum dimer (spin-Peierls) phase in the one-dimensional system has attracted much attention and been reported in many papers [27]. However, the phase diagram and the universality class are still unclear, as we mentioned in Chap. 1. It is far from trivial to analyze the spin-Peierls system analytically due to the existence of multiple (spin and phonon) degrees of freedom and the infinite dimension of the Hilbert space. Thus, we have to resort to numerical calculations. Accurate calculations are, however, still difficult to be reached by the exact diagonalization method and the density matrix renormalization group method due to the needed large Hilbert space.

The Monte Carlo method can treat such large systems, but there are many difficulties of applying the conventional QMC method [16, 18, 19, 21, 23, 27] as follows:

1. Fine-mesh slowing down.
2. Ergodicity satisfaction.
3. Necessity of the occupation number cutoff.
4. Rejection (bounce) from treating many candidate states.
5. Calculation of non-trivial correlation functions and energy gaps.
6. Appearance of the long-range interactions.

Our new method presented below completely overcomes all of these problems.

1. When we use a real coordinate basis for the lattice degree of freedom, which is called the path-integral Monte Carlo, the fine mesh of the imaginary time brings about the slowing down as we mentioned in the last section. In order to avoid the discretization error and slowing down, we transform the lattice degree of freedom into the boson (phonon) by the second quantization and represent the system on the continuous time as introduced in Sect. 3.3.1.
2. The transformed Hamiltonian, however, does not conserve the total number of bosons. Thus, the conventional worm update cannot satisfy the ergodicity (irreducibility) because the generated configurations keep the occupation number constant in the imaginary time direction. Then, we extend the worm (directed-loop)

update for satisfying the ergodicity by developing an update called *warp update* and using a variant of the worm named *bug* in Sect. 3.4.3.

3. In the meantime, the SSE, which uses the high-temperature series, is known as one of the exact representation of quantum systems as we mentioned. For systems with soft-core bosons like the present spin-Peierls model, however, it is necessary to impose an occupation number cutoff for the soft-core bosons in the high-temperature series representation, which introduces an artificial systematic error. Thus, we purposely select not the high-temperature series but the continuous imaginary-time representation in order to avoid the cutoff and reduce significantly the CPU time, as we will explain in detail in the Sect. 3.3.2.

4. When we conduct the worm scattering at operators, there are many next candidate states. Here, the update procedure of the worm algorithm has an analogy with the single spin update of the Potts model thoroughly discussed in the last chapter. Thus the optimization of transition probabilities is very important for efficient calculation. In fact, the rejection that we call the bounce has been a serious bottleneck generally in the worm algorithm. We have succeeded in perfectly eliminating the bounce process in the worm scattering, applying the novel optimization approach that we introduced in Sect. 2.3.

5. Moreover, we will explain the detailed calculation of non-trivial correlation functions and energy gaps, which are fully utilized in the level spectroscopy. Particularly for investigating the critical phenomena, it is also critical to precisely calculate correlation functions. It is not trivial, however, to calculate off-diagonal (Green's) correlations, e.g. $\langle S^-(\tau)S^+ \rangle$ and $\langle a(\tau)a^\dagger \rangle$; the local update of worldline configurations, such as, the insertion of pair off-diagonal operators, cannot catch the above non-trivial correlations. The worm algorithm, on the other hand, constructs extended configurations where the off-diagonal correlations directly appear. Then, we can acquire such quantities by an ingenious reweighting procedure as explained in Sect. 3.4.4.

6. The transformed spin-phonon model includes long-range interactions when the phonon has a dispersion. Treating these correctly can be a drawback in practical simulations, consuming the CPU time. We then apply an efficient algorithm called *Walker's method of alias* and succeed in reducing the CPU time cost significantly as first developed and demonstrated by Fukui et al. [8]. Moreover, we have to take an infinite number of weights into consideration owing the the dispersive phonon. We will also introduce a guiding weight for efficient treatment of various matrix elements that come from the long-range interactions.

3.3 Representation of Quantum Systems

3.3.1 Continuous Time Representation

The spin-Peierls system has been numerically investigated by the path-integral Monte Carlo method [20], where the real-space basis is used for the lattice degree of

freedom and the imaginary time is decomposed. The applicable models of the method, however, have been restricted to small (one-dimensional) systems. It is because the relaxation (convergence) of the Markov chain becomes fatally slow when the discretization step is decreased. Recently, it has been possible to eliminate the discretization error by taking advantage of the discrete feature of the second quantization for the lattice degree of freedom [27]. As a modern representation without the decomposition error, let us describe the partition function in continuous time at first and see the relation with the high-temperature series later.

In the continuous-time representation, we decompose the Hamiltonian into two parts:

$$H = H_0 + V. \tag{3.4}$$

We assume the part H_0 to be a diagonal operator according to a chosen basis set. The partition function of a canonical ensemble at inverse temperature β is expanded as

$$
\begin{aligned}
Z = \mathrm{tr}\, e^{-\beta H} &= \mathrm{tr}\left[T_\tau \exp\left(-\int_0^\beta d\tau\, V(\tau) \right) e^{-\beta H_0} \right] \\
&= \mathrm{tr}\left[\left(1 - \int_0^\beta d\tau_1 V(\tau_1) + \int_0^\beta d\tau_1 \int_{\tau_1}^\beta d\tau_2 V(\tau_1) V(\tau_2) + \cdots \right. \right. \\
&\qquad \left. \left. + (-1)^n \int_0^\beta d\tau_1 \int_{\tau_1}^\beta d\tau_2 \cdots \int_{\tau_{n-1}}^\beta d\tau_n \prod_{i=1}^n V(\tau_i) + \cdots \right) e^{-\beta H_0} \right].
\end{aligned}
\tag{3.5}
$$

Here T_τ is the time-ordering operator and $V(\tau) = e^{-\tau H_0} V e^{\tau H_0}$ as accustomed in the interaction representation. Inserting complete basis sets between V's, we rewrite the partition function as

$$
\begin{aligned}
Z = \sum_{\alpha_1} \langle \alpha_1 | e^{-\beta E_1} |\alpha_1\rangle \;+\; \sum_{n=1}^\infty \sum_{(\alpha_1,\ldots,\alpha_n)} \sum_{(\ell_1,\ldots,\ell_n)} \int_0^\beta d\tau_1 \int_{\tau_1}^\beta d\tau_2 \cdots \int_{\tau_{n-1}}^\beta d\tau_n \\
e^{-\tau_1 E_1} \langle \alpha_1 | - V_{\ell_1} |\alpha_2\rangle e^{-(\tau_2-\tau_1)E_2} \cdots \langle \alpha_n | - V_{\ell_n} |\alpha_1\rangle e^{-(\beta-\tau_n)E_1},
\end{aligned}
\tag{3.6}
$$

where $E_i = \langle \alpha_i | H_0 | \alpha_i \rangle$, and V_ℓ is one of local operators of which the term V consists. If all the matrix elements $\langle \alpha_p | - V_{\ell_p} | \alpha_{p+1} \rangle$ are positive definite, we can designate a weight for each worldline configuration as

$$w_{\mathrm{ct}} = e^{-\beta E_1} \prod_{p=1}^n \langle \alpha_p | - V_{\ell_p} |\alpha_{p+1}\rangle e^{-\tau_p(E_p - E_{p+1})} d\tau_p, \tag{3.7}$$

where $\alpha_{n+1} = \alpha_1$ from the periodicity of the imaginary-time axis. If some diagonal elements of the local operator $\langle \alpha_p | - V_{\ell_p} | \alpha_{p+1} \rangle$ have negative values, we need to subtract a constant from the operator in order to avoid the negative signs. On

the other hand, if there exist off-diagonal elements with negative value, the QMC method may suffer from the notorious negative-sign problem. We will rewrite the spin-Peierls Hamiltonian (3.1) later so that any negative sign does not appear. Since this formulation is free from the decomposition error of imaginary time, we do not need to extrapolate the discretization step and physical quantities can be exactly calculated within a statistical error alone.

As we mentioned, the high-temperature series is another useful representation of the QMC method. If we set $H_0 = 0$ and integrate all τ_i in Eq. (3.5), one gets the representation of the high-temperature series; the partition function is expressed as

$$
\begin{aligned}
Z &= \sum_{n=0}^{\infty} \frac{\beta^n}{n!} \mathrm{tr}(-H)^n \\
&= \sum_{n=0}^{\infty} \sum_{(\alpha_1,\ldots,\alpha_n)} \sum_{(l_1,\ldots,l_n)} \frac{\beta}{n!} \prod_{p=1}^{n} \langle \alpha_p | - H_{\ell_p} | \alpha_{p+1} \rangle,
\end{aligned}
\tag{3.8}
$$

and the weight as

$$
w_{\mathrm{hs}} = \frac{\beta}{n!} \prod_{p=1}^{n} \langle \alpha_p | - H_{\ell_p} | \alpha_{p+1} \rangle.
\tag{3.9}
$$

This expression is used in the SSE method.

Let us see the case of our spin-Peierls model (3.1) in more detail. First, we subtract a constant C from the spin operator in the model in order to eliminate the negative sign as we will mention in Sect. 3.4 and decompose the Hamiltonian into two parts

$$
H = H^{\mathrm{sp}} + H^{\mathrm{p}} + const,
\tag{3.10}
$$

where

$$
H^{\mathrm{sp}} = \sum_r J \left(1 + \sqrt{\frac{\omega \lambda}{2}} (a_r^{\dagger} + a_r)(S_{r+1} \cdot S_r - C) \right)
\tag{3.11}
$$

$$
H^{\mathrm{p}} = \omega \sum_r \left(a_r^{\dagger} + CJ\sqrt{\frac{\lambda}{2\omega}} \right) \left(a_r + CJ\sqrt{\frac{\lambda}{2\omega}} \right),
\tag{3.12}
$$

and C is necessary to be greater than or equal to $1/4$ for $S = 1/2$ as shown later. We shift the boson operator:

$$
a_r^{\dagger} \;\rightarrow\; a_r^{\dagger} - CJ\sqrt{\frac{\lambda}{2\omega}}
\tag{3.13}
$$

$$
a_r \;\rightarrow\; a_r - CJ\sqrt{\frac{\lambda}{2\omega}}.
\tag{3.14}
$$

Then the Hamiltonian and parameters are redefined as

$$H = H^{\text{sp}} + H^{\text{p}} \tag{3.15}$$

$$H^{\text{sp}} = \sum_r J \left(1 + \sqrt{\frac{\omega \lambda}{2}} \left(a_r^\dagger + a_r - CJ\sqrt{\frac{2\lambda}{\omega}} \right) (S_{r+1} \cdot S_r - C) \right)$$

$$= \sum_r J \left(1 - CJ\lambda + \sqrt{\frac{\omega \lambda}{2}} (a_r^\dagger + a_r)(S_{r+1} \cdot S_r - C) \right) \tag{3.16}$$

$$= \sum_r \tilde{J} \left(1 + \sqrt{\frac{\omega \tilde{\lambda}}{2}} (a_r^\dagger + a_r)(S_{r+1} \cdot S_r - C) \right)$$

$$H^{\text{p}} = \omega \sum_r a_r^\dagger a_r, \tag{3.17}$$

where

$$\tilde{J} = J \left(1 - CJ\lambda \right) \tag{3.18}$$

$$\tilde{\lambda} = \frac{\lambda}{(1 - CJ\lambda)^2}. \tag{3.19}$$

Note that the spin-phonon coupling parameter λ must be smaller than $1/CJ$ so that negative signs do not appear. This parameter region is notwithstanding enough broad to investigate the relevant quantum phase transition in the spin-Peierls system.

3.3.2 Comparison to High-Temperature Series

Although there are two modern representations in the QMC method (the continuous-time path integral and the high-temperature series) as we saw, we adopt the continuous-time representation for the spin-Peierls model. One of the reasons is that it is inevitable to impose a cutoff of boson (phonon) occupation number in the SSE method in the high-temperature representation. Our original model (3.1) has the negative diagonal elements for the lattice term ($\langle \alpha | - \omega \sum_r a_r^\dagger a_r | \alpha \rangle = -\omega n_b$, where n_b is the total number of bosons) when we use the occupation-number basis in the high-temperature series (3.8). Thus we have to subtract a constant D from the operator ($a_r^\dagger a_r \rightarrow a_r^\dagger a_r - D$) in order to avoid the negative sign. If we restrict the Hilbert space of boson such that the occupation number has to be below the constant D, this cutoff introduces a systematic error. Then, we need to set the cutoff D to a larger value to some extent than the expectation value. The larger the cutoff is, however, the heavier the CPU-time cost becomes. Let us consider how energy is measured in the high-temperature series in order to figure out this reason. On one hand, the energy average of a canonical ensemble is expressed as

$$\langle E \rangle = -\frac{\partial \ln Z}{\partial \beta}. \tag{3.20}$$

On the other hand, from Eq. (3.8) the derivative is described in the high-temperature series as

$$-\frac{\partial \ln Z}{\partial \beta} = -\frac{1}{Z} \sum_{n=0}^{\infty} n \frac{\beta^{n-1}}{n!} \mathrm{tr}(-H)^n = -\frac{\langle n \rangle}{\beta}, \tag{3.21}$$

where $\langle n \rangle$ is the thermal average of the number of operators. Therefore, the energy is measured by the number of operators on the worldlines:

$$\langle E \rangle = -\frac{\langle n \rangle}{\beta}. \tag{3.22}$$

In the meanwhile, the CPU-time cost for one Monte Carlo step is proportional to $\langle n \rangle$ (note that the cost is proportional to $\Lambda > n$ in using the fixed-length SSE method with length Λ [25]) for sweeping the whole worldlines. If we set the cutoff to a significantly larger value than the occupation number of boson in simulations so that the systematic error can be ignored, the energy density for the lattice term is about ωD. Since the energy density for the spin term is J (we assume the spin interaction changes slightly by the spin-phonon coupling), the CPU time linearly increases in proportion as $N\beta(J + \omega D)$, where N is the number of sites.

On the other hand, we can eliminate the cutoff without additional CPU-time cost by using the continuous-time representation. Here, let us set $H_0 = H^{\mathrm{p}}$ and $V = H^{\mathrm{sp}}$ in the Hamiltonian (3.4). Since we include the lattice term into H_0, there is no problematic diagonal element in $V = H^{\mathrm{sp}}$ term. Therefore, the CPU-time cost in this representation increases to $N\beta J$. As an example, if we set the parameters $J = 1$, $\omega = 1/4$ and the cutoff $D = 40$, the CPU time of the SSE method using the high-temperature series becomes about 10 times longer than that of the continuous-time representation (note that if we set ω smaller, the average occupation number getting larger, and we need to set also the cutoff D larger). This argument about CPU-time cost from a truncation is generally valid for simulations of not only our spin-Peierls model but also any soft-core bosonic model including potential terms, such as the bose Hubbard model.

To sum up, the continuous-time representation is the much better choice than the SSE method for soft-core bosonic models since we can include the problematic diagonal operators into H_0. For the application to the spin-Peierls systems that include the phonon degree of freedom as a soft-core boson, we adopt the continuous-time representation because of the above rational reason.

3.4 Update Procedure

3.4.1 Worldline Configuration

In this subsection, we will see an example of worldline configurations. First, let us focus our attention on the spin operators in the (isotropic) spin-Peierls model (3.15):

$$
-H^{\mathrm{s}} = -\sum_r \tilde{J}\,(S_{r+1} \cdot S_r - C)
$$

$$
= -\sum_r \tilde{J}\,\left\{ \frac{1}{2}(S_{r+1}^+ S_r^- + S_{r+1}^- S_r^+) + S_{r+1}^z S_r^z - C \right\}
$$

$$
\equiv -\sum_r H_{r+1,r}^{\mathrm{s}}. \tag{3.23}
$$

We adopt the eigenstate of the local S^z as the basis. Then the matrix $H_{r+1,r}^{\mathrm{s}}$ for $S = 1/2$ is expressed as

$$
-H_{r+1,r}^{\mathrm{s}} = \tilde{J}
\begin{pmatrix}
-\frac{1}{4}+C & 0 & 0 & 0 \\
0 & \frac{1}{4}+C & -\frac{1}{2} & 0 \\
0 & -\frac{1}{2} & \frac{1}{4}+C & 0 \\
0 & 0 & 0 & -\frac{1}{4}+C
\end{pmatrix}
\begin{matrix}
|\uparrow\uparrow\rangle \\
|\uparrow\downarrow\rangle \\
|\downarrow\uparrow\rangle \\
|\downarrow\downarrow\rangle
\end{matrix}. \tag{3.24}
$$

Although the off-diagonal elements seem to give rise to negative signs, the sign of $S_{r+1}^+ S_r^- + S_{r+1}^- S_r^+$ does not matter to the physics on bipartite lattices; this inversion corresponds to the gauge rotation around z-axis in the spin state space. Then, we are allowed to invert the sign on the off-diagonal elements from $-\frac{1}{2}$ to $\frac{1}{2}$. The constant C must be greater than or equal to $1/4$ for $S = 1/2$ (S^2 for general S) spin in order to eliminate the negative signs on the diagonal elements. The constant is often chosen as $1/4$ because the matrix elements become binary (0 or $1/2$), which makes a program simple in practice. A typical worldline configuration of spins for 4-site chain is described in Fig. 3.1. The depicted configuration is corresponding to a state in the representation (3.6) for $V_\ell = H_{\ell+1,\ell}^{\mathrm{s}}$ such that $n = 6$, $\{\tau_i^6\}_{i=1}$, $(\ell_1, \ell_2, \ell_3, \ell_4, \ell_5, \ell_6) = (0, 2, 1, 2, 0, 2)$, and
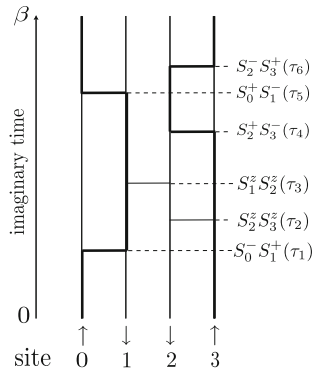
$$
|\alpha_1\rangle = |\uparrow\downarrow\downarrow\uparrow\rangle \tag{3.25}
$$

$$
|\alpha_2\rangle = |\alpha_3\rangle = |\alpha_4\rangle = |\downarrow\uparrow\downarrow\uparrow\rangle \tag{3.26}
$$

$$
|\alpha_5\rangle = |\downarrow\uparrow\uparrow\downarrow\rangle \tag{3.27}
$$

$$
|\alpha_6\rangle = |\uparrow\downarrow\uparrow\downarrow\rangle. \tag{3.28}
$$

Fig. 3.1 Example of the worldline configuration of 4-site spin chain. The symbols $S_1^z S_2^z$ and $S_2^z S_3^z$ represent the operators $-\tilde{J}(S_1^z S_2^z - C)$ and $-\tilde{J}(S_2^z S_3^z - C)$, respectively. The bold lines that are never cut on the worldlines expresses the sequence of up spin configuration, which means that the Hamiltonian conserves the total S^z

Note that a local operator V_{ℓ_p} and a state $|\alpha_p\rangle$ are not independent of each other.

Let us consider how we update this worldline configuration. As an example of failure, a local flip that changes only $|\alpha_1\rangle$ from $|\uparrow\downarrow\downarrow\uparrow\rangle$ to $|\downarrow\downarrow\downarrow\uparrow\rangle$ is not allowed because the Hamiltonian conserves the total S^z. Even if a model does not conserve a particle number, naive local updates like above is fatally inefficient in general. In the following sections, we will explain an efficient update method for continuous-time worldline configurations. The update procedure consists of two main update processes: the diagonal update and the off-diagonal update.

3.4.2 Diagonal Update

We need to update the number of operators and the shape of worldlines in the QMC method. In the diagonal update, the number of operators is updated, where diagonal operators in V term of the Hamiltonian (3.4) are inserted or removed. Let us start from the worldline configuration shown in Fig. 3.1 and see an example of operator removal. If we try to remove the off-diagonal operator $S_0^- S_1^+ (\tau_1)$, the trial could be accepted with a certain probability if we change the operator $S_0^+ S_1^- (\tau_5)$ to $S_0^z S_1^z (\tau_5)$ and related intermediate states $\{\alpha_{p=2}^5\}$ simultaneously in the case where $C > 1/4$. In general, however, it is quite difficult and not allowed in most cases to insert/remove an off-diagonal operator. As for diagonal operators, on the other hand, we can insert/remove them independently of other configurations. If the operator $S_2^z S_3^z (\tau_2)$ in the figure is removed, the worldline configuration changes to a state such that $n = 5$, $\{\tau_{i=1}^5\}$, $(\ell_1, \ell_2, \ell_3, \ell_4, \ell_5) = (0, 1, 2, 0, 2)$, and

$$|\alpha_1\rangle = |\uparrow\downarrow\downarrow\uparrow\rangle \tag{3.29}$$

$$|\alpha_2\rangle = |\alpha_3\rangle = |\downarrow\uparrow\downarrow\uparrow\rangle \tag{3.30}$$

$$|\alpha_4\rangle = |\downarrow\uparrow\uparrow\downarrow\rangle \tag{3.31}$$

$$|\alpha_5\rangle = |\uparrow\downarrow\uparrow\downarrow\rangle, \tag{3.32}$$

in the representation (3.6). Therefore, we try to insert/remove only diagonal operators for updating the number of operators.

Next, let us consider an appropriate probability of this update. As we mentioned, trials to insert/remove a diagonal operator are independent of each other at every imaginary time; namely, this is a Poisson process. Let us update the number of diagonal operators with the matrix element (intensity) v. Now assume that there are n_1 operators in time interval τ and they are indexed as $\tau_1, ..., \tau_{n_1}$. A weight contribution is described as

$$w(\{\tau_1, ..., \tau_{n_1}\}) = (v d\tau)^{n_1} \tag{3.33}$$

from Eq. 3.7 ($v = \langle \alpha_p | - V_{\ell_p} | \alpha_{p+1} \rangle$). We consider using an intensity v' (guiding weight) that may be different from the true value v because it is convenient to use an uniform intensity even if a true matrix element varies depending on imaginary time. Here, we consider removing some operators at first and inserting operators subsequently. A probability that the number of operators is changed from n_1 to k by removal is expressed by the probability density function (PDF) of a binomial distribution:

$$f(k\,;n, 1 - p_{\text{out}}) = \binom{n}{k} (1 - p_{\text{out}})^k \, p_{\text{out}}^{n-k}, \tag{3.34}$$

where

$$p_{\text{out}} = \min\left(1, \frac{v'}{v}\right). \tag{3.35}$$

Note that if $v = 0$, no operator exists, and no removal is tried. As for insertion, a probability that $n_2 - k + k'$ trial events occur with the intensity v' in time interval τ is described by the PDF of a Poisson distribution:

$$Pois(n_2 - k + k'; v'\tau) = \frac{e^{-v'\tau} (v'\tau)^{n_2-k+k'}}{(n_2 - k + k')!}. \tag{3.36}$$

Then, the trial is accepted by probability

$$p_{\text{in}} = \min\left(1, \frac{v}{v'}\right). \tag{3.37}$$

The probability that $n_2 - k$ insertions success among $n_2 - k + k'$ trials and $n_2 - k$ points with width $d\tau$ are chosen is written as

$$f(k'; n_2 - k + k', 1 - p_{\text{in}}) \left(\frac{d\tau}{\tau}\right)^{n_2 - k}$$

$$= \binom{n_2 - k + k'}{k'} (1 - p_{\text{in}})^k p_{\text{in}}^{n-k} \left(\frac{d\tau}{\tau}\right)^{n_2 - k}. \tag{3.38}$$

Then we define a probability that the number of diagonal operators is updated from n_1 to n_2 through k and $n_2 + k'$ as

$$p(n_1 \to k \to n_2 + k' \to n_2)$$
$$= f(k; n_1, 1 - p_{\text{out}}) Pois(n_2 - k + k'; v'\tau)$$
$$f(k'; n_2 - k + k', 1 - p_{\text{in}}) \left(\frac{d\tau}{\tau}\right)^{n_2 - k} n_2!, \tag{3.39}$$

where the final factorial ($n_2!$) is the number of events that times are indexed as $\{\tau_1, ..., \tau_{n_2}\}$. Finally, the detailed balance condition,

$$w(\{\tau_1, ..., \tau_{n_1}\}) p(n_1 \to k \to n_2 + k' \to n_2)$$
$$= w(\{\tau_1, ..., \tau_{n_2}\}) p(n_2 \to k \to n_1 + k' \to n_1), \tag{3.40}$$

where $0 \le k \le \min(n_1, n_2)$, $0 \le k'$, $v' > 0$, is satisfied from the above equations. It is the important point that using any value $v' > 0$ is allowed for this diagonal update. We show an example of this balance in the simplest case where $v' = v$. In this case, other values become simple as $p_{\text{out}} = p_{\text{in}} = 1$, $k = k' = 0$ and Eq. (3.40) is simplified as

$$(vd\tau)^{n_1} \frac{e^{-v\tau}(v\tau)^{n_2}}{n_2!} \left(\frac{d\tau}{\tau}\right)^{n_2} n_2!$$
$$= (vd\tau)^{n_2} \frac{e^{-v\tau}(v\tau)^{n_1}}{n_1!} \left(\frac{d\tau}{\tau}\right)^{n_1} n_1!. \tag{3.41}$$

We have considered a time interval τ and a diagonal matrix element v. In the diagonal operator, all we need to do is to insert/remove diagonal operators on every worldline segments with respective time interval and intensity. Instead of conducting the above update procedure on each segment, we adopt an exactly equivalent stochastic process that is easier to be implemented as following:

- Set a guiding rate (weight) v'_i to each local operator.
- Start from $\tau = 0$.
- Repeat

1. Generate τ_{proceed} from the exponential distribution of rate $v'_{tot} = \sum_i v'_i$; $\tau_{\text{procced}} \sim v'_{tot} \exp(-v'_{tot} \tau)$.
2. Set $\tau_{\text{next}} = \tau + \tau_{\text{proceed}}$.

3. If a diagonal operator with a matrix element $v_i(\tau_i)$ exists at τ_i such that $\tau < \tau_i < \tau_{\text{next}}$, remove it with probability $p_{\text{out}} = \min(1, v_i'/v_i(\tau_i))$.
4. Set $\tau = \tau_{\text{next}}$.
5. If $\tau < \beta$, choose a local operator with probability v_i'/v_{tot}', and insert it at τ with prob. $p_{\text{in}} = \min(1, v_i/v_i')$.

- Stop if $\tau \geq \beta$.
- Leave all off-diagonal operators on the worldlines untouched.

Since the exponential distribution is characterized by the memoryless property

$$\Pr(\tau > s + t | \tau > s) = \Pr(\tau > t) \qquad \forall s,\, t \geq 0, \tag{3.42}$$

we end up trying to insert/remove diagonal operators at every imaginary time independently by the above procedure.

In the case of the isotropic spin-Peierls model (3.15), we set $C = 1/4$ and $v_i' = 1/2$. The diagonal update is simplified by this choice, where we insert a local spin diagonal operator only if relevant spins are antiparallel and remove all pre-existing diagonal operators certainly.

In spite of this one-way sweep from 0 to β, the above update procedure ensures the detailed balance because of the independence. We note that a similar one-way sweep on the operator string in the SSE method indeed breaks the detailed balance because each trial of operator insertion/removal is not independent of each other (but dependent on the total number of operators as expressed in Eq. (3.9). Nevertheless, it satisfies the total balance in the whole one-way sweep since this is nothing but the sequential single spin update by fixed order.

Our formulation and method in this diagonal update is valid to any Poisson process in general. Although our time evolution is on imaginary-time axis, the mathematical formulation is the just same with the time evolution that follows any master equation. Thus our procedure is directly applicable to many kinds of equilibrium/nonequilibrium systems.

3.4.3 Off-Diagonal Update

3.4.3.1 What is Worm?

The off-diagonal update changes the shape of the worldlines, such as spin/boson configurations and operator types. It is not trivial to update them efficiently with keeping the periodicity in the imaginary-time direction. Naive local updates like insertion of pair off-diagonal operators is hardly accepted when the interval time is not short although this kind of local updates had been used for years. One of significant progresses of the QMC method was the developments of the nonlocal update methods; The standard method now is the loop algorithm or the worm (directed-loop) algorithm. In the case of quantum spin systems without external field, the loop algorithm is very efficient, which is free from the critical slowing down [6]. However,

the loop update becomes inefficient for soft-core bosonic systems because the size of forced-made cluster necessarily differs from the true correlation length.

In the meantime, there are many interesting systems that are difficult to be *locally* updated in the MCMC method because of strong constraints, such as a protein holding problem, a statistical test, not to mention correlated quantum systems. Recently, some efficient methods for these problems have been proposed. They are based on the idea that configuration space is extended so that the constraint is *partially* broken. As an example, an extended ensemble method for lattice proteins was proposed by Iba et al. [14], where a double occupation prohibited in the original ensemble is allowed. The worm algorithm, which was invented by Prokov'ev et al. [22] and later developed by Syljuasen et al. into more efficient one called the directed-loop algorithm [26], is also one of such approaches. In quantum spin systems, the worm is a pair of spin-ladder operators, S_i^+ and S_i^-; here i is a site index. In bosonic systems, the worm is a pair of creation and annihilation operators, $a_i^\dagger$ and a_i. In the worm update, we insert this worm on worldlines as kinks with a certain probability. In other words, an infinitesimal segment of worldline is flipped. Then we move a kink (one of the pair) stochastically. Namely, the successive segments of worldline is flipped one after another as illustrated in Fig. 3.2. When the moving kink comes back to the other, they destroy each other with a certain probability. In the worm algorithm, we extend the configuration space by breaking the constraint (conservation law) of the model so that two kinks exist on the worldlines. The application range of the conventional
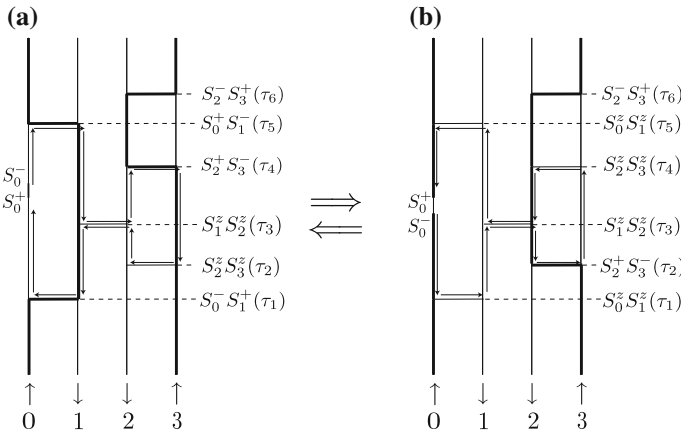
Fig. 3.2 Example of the spin-worm update (from inserting to vanishing). First one chooses a site and a time on the worldlines and inserts a pair of operators S_i^+ and S_i^- (spin ladder operators). Here i is a site index. In the figure, we choose site 0 and time τ_{insert} ($\tau_3 < \tau_{\text{insert}} < \tau_4$). Then one chooses a head of the worm and a worm-proceeding direction. When the worm head encounters an operator, a pathway is chosen with a certain probability. Now the head deterministically moves on the loop only by *turn* since we subtract constant $1/4$ from the local operators $S_{r+1} \cdot S_r$. When the head comes back to the tail, the worm vanishes from the worldlines with a certain probability

worm, however, is limited to particle number conserving systems. We will, then, extend the worm move so that also nonconserved particles can be correctly treated.

At first we will review the conventional worm update. It is actually a somewhat different perspective from usual, e.g., about the detailed balance. Since we have two degrees of freedom, spin and boson (phonon), in the spin-Peierls model (3.15), we consider having the two (spin and boson) sets of worldlines and updating them by using each worm.

3.4.3.2 Conventional Worm Move

Let us consider the spin worm update for the isotropic spin-Peierls model at first. It is just the same with the simple antiferromagnetic Heisenberg model. An example of the spin-worm update is shown in Fig. 3.2. We start with the worldline configuration in Fig. 3.1.

The worm update is as follows: First, a site and a time is chosen on the world-lines, and inserts a pair of operators. Here we choose site 0, and time τ_{insert} ($\tau_3 < \tau_{\text{insert}} < \tau_4$) as shown in Fig. 3.2a. Since the site configuration is up or down, the order of spin ladder operators (S_0^+ and S_0^-) has to be as in the figure. Next we choose the moving operator between the two. The mover is called the head of the worm, and the other is called the tail. Here we choose S_0^- as a head, and S_0^+ as a tail. Let us move the head upwards. The spin configuration between the head and the tail is being updated from down to up. How long the head goes is determined by the change in diagonal (exponential) weight in the representation (3.7). In our spin-Peierls model, we set $H_0 = H^p$, so that the weight of the configuration is not changed by the spin-worm move between the operators. In general, the transition probability between two configurations that have the same weight can be set to unity. Hence the head can certainly go to the next operator. Now the head encounters operator $S_0^+ S_1^-$ (τ_5). When the head visits an operator, we choose an exit (or a pathway) with a certain probability. Each pathway is named as in Fig. 3.3. Now by choosing *turn*, the operator is changed from $S_0^+ S_1^-$ to $S_0^z S_1^z$, and the head is changed from S_0^- to S_1^- (Fig. 3.4). Then the head moves to the next operator, and chooses the exit and so on. When the head comes back to the tail, the worm vanishes from the worldline with a certain probability. This successive update from the insertion to the vanishment is the one worm update. The worldline configuration is here changed from Fig. 3.2a, b by the worm move. Let us, next, think of appropriate transition probabilities of the worm update in general cases. Assume that a configuration is updated by the worm as $c \to (c_0, d_0) \to (c_1, d_1) \to (c_2, d_2) \to \cdots \to (c_N, d_N) \to c'$, where N is the number of operators the head visits, c and c' are configurations before and after the one worm update, c_i is the i-th extended worldline configuration includ-ing the worm and d_i is the worm-proceeding direction, up or down, after the i-th operator. We emphasize that the configuration that the head moves upwards is distin-guished from that it moves downwards. We define $w_{(c_i, d_i)}$ as the weight of (c_i, d_i) and $p_{(c_i, d_i) \to (c_{i+1}, d_{i+1})}$ as the transition probability from (c_i, d_i) to (c_{i+1}, d_{i+1}). When
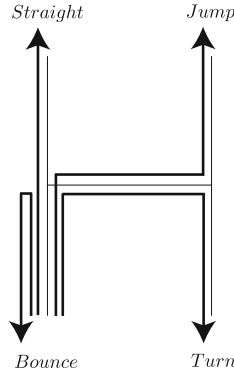
Fig. 3.3 Pathways of the worm head at a two-body operator. One exit is stochastically chosen according to the weight change
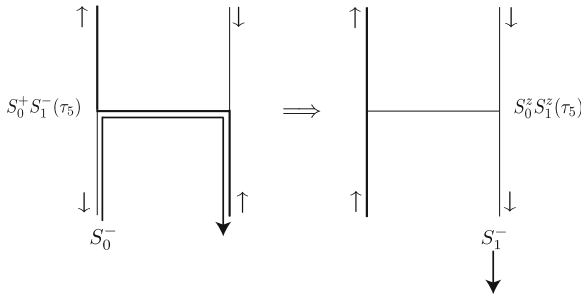
Fig. 3.4 Configuration change by the worm that chooses *turn*. The operator is changed from $S_0^+ S_1^-$ to $S_0^z S_1^z$, and the head is changed from S_0^- to S_1^-

the worm scatters at operators, an exit is chosen by a probability that satisfies the balance condition:

$$w_{(c_i,d_i)} = \sum_{(c_{i-1},d_{i-1})} w_{(c_{i-1},d_{i-1})} \, p_{(c_{i-1},d_{i-1}) \to (c_i,d_i)} \qquad 1 \le i \le N. \qquad (3.43)$$

When the worm is inserted or vanished, the probabilities are determined so that they satisfies these conditions:

$$w_{(c_0,d_0)} = \sum_c w_{(c)} \, p_w \qquad\qquad\qquad (3.44)$$

$$w_{(c')} = \sum_{(c_N,d_N)} w_{(c_N,d_N)} \, p_v, \qquad\qquad (3.45)$$

where $p_w = p_p p_h p_d$, we choose the worm-insertion point with the probability p_p, the head with p_h, and the proceeding direction with p_d at configuration c, and we vanish the worm with p_v after moving. Finally the configuration becomes c'. The balance condition between c and c' in one worm update is then expressed as

$$\sum_{N=1}^{\infty} \sum_{(c_0,d_0)\cdots(c_N,d_N)} \sum_{c} w_{(c)} p_w \prod_{i=0}^{N-1} p_{(i\to i+1)} p_v = w_{(c')}. \tag{3.46}$$

It is clear that this total balance is satisfied from the conditions (3.43), (3.44) and (3.45). Note that each worm-scattering process never satisfy the detailed balance because the backward transition from (c_i, d_i) to any (c_{i-1}, d_{i-1}) does not occur; that is, the moving direction is opposite. Also note that we can arbitrarily define the extended configuration including the worm in order to make the update efficient within the total balance. The artificial weight has to be reweighted in calculating off-diagonal correlations as we mention later.

In general, it is difficult to find qualified transition probabilities also taking the worm-proceeding direction into account. We have to, there, solve the huge simultaneous equation. If we assume that the direction does not matter to the configuration weight, however, we can easily determine appropriate probabilities. The condition (3.43) is reduced to a simpler form:

$$w_{(c_i)} = \sum_{c_{i-1},d_{i-1}} w_{(c_{i-1})} p_{(c_{i-1},d_{i_1})\to(c_i,d_i)}. \tag{3.47}$$

Here, it is crucial to avoid the *bounce* process. When the head bounces, it just cancels the last update; this is nothing but the rejection. Furthermore, the bounce process will enhance the diffusion property of the worm head, which hinders efficient sampling. We stress that our rejection-minimized methods that use the geometric allocation algorithms (in Sect. 2.3) brilliantly perform for eliminating the bounce process. Thus, the sampling efficiency is significantly improved by our optimized worms. This application of our optimization method is one of the important points for precise investigation of the spin-Peierls systems.

Note that, in the previous literature, the pseudo detailed balance

$$w_{(c_{i-1})} p_{(c_{i-1},d_{i-1})\to(c_i,d_i)} = w_{(c_i)} p_{(c_i,d'_i)\to(c_{i-1},d'_{i-1})} \tag{3.48}$$

is used, where the directions d'_{i-1} and d'_i are opposite to d_{i-1} and d_i, respectively. Still, the detailed balance of each worm scattering is not satisfied although this difference has never been stressed before. Nevertheless, with similar conditions assumed in the worm insertion/vanishment, the detailed balance condition of the one worm update

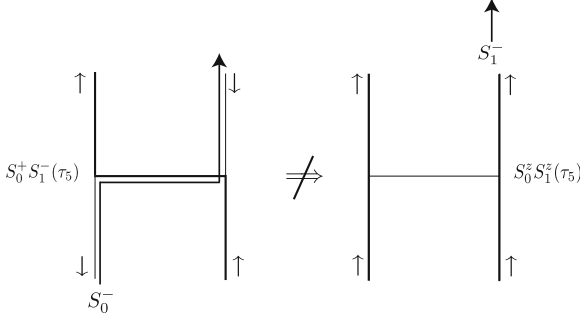$$w_{(c} p_{(c\to c')}) = w_{(c')} p_{(c'\to c)} \tag{3.49}$$

Fig. 3.5 Example that the worm cannot go *jump*. It is because the matrix element $\langle \uparrow\uparrow | - (S_0^z S_1^z - 1/4)| \uparrow\uparrow \rangle = 0$. We subtract constant $1/4$ from operator $S_{r+1} \cdot S_r$ in order to make the worm to go only *turn* in the conventional move

is derived. Although this property is one of interesting points of the worm algorithm, the detailed balance is not necessary as we know. Particularly for the boson worm update, the efficiency is indeed improved by breaking it in our simulations .

Next we shall see an example of the worm scattering probabilities of the spin worm. Let us set the subtracted constant C to $1/4$ and invert the negative off-diagonal elements of Eq. 3.24, which does not change the physics as mentioned in Sect. 3.4.1. Then the matrix forms as

$$- H_{r+1,r}^s = \tilde{J} \begin{pmatrix} 0 & 0 & 0 & 0 \\ 0 & \frac{1}{2} & \frac{1}{2} & 0 \\ 0 & \frac{1}{2} & \frac{1}{2} & 0 \\ 0 & 0 & 0 & 0 \end{pmatrix} \begin{matrix} |\uparrow\uparrow\rangle \\ |\uparrow\downarrow\rangle \\ |\downarrow\uparrow\rangle \\ |\downarrow\downarrow\rangle \end{matrix} . \tag{3.50}$$

In this case, the head cannot go *straight* or *jump* because the matrix element becomes zero, e.g., $\langle \uparrow\uparrow | - (S_0^z S_1^z - 1/4)| \uparrow\uparrow \rangle = 0$ by *jump* as in Fig. 3.5. Therefore the head must go *turn* or *bounce*. Since the matrix element of $- (S_i^z S_j^z - 1/4)$ and that of the off-diagonal operator $(S_i^+ S_j^- + S_i^- S_j^+)$ are the same value $1/2$, we can move the head by *turn* with probability unity. Hence the worm deterministically moves on the each loop as in Fig. 3.2. This update is exactly the same with the single loop update of the loop algorithm [7]. If we subtract a constant above $1/4$ in the model, the worm can go also *straight* and *jump*.

The remaining question is how many worms should be inserted in one Monte Carlo step. The update efficiency varies according to the number of the worms, namely, the ratio between the diagonal update and off-diagonal update. Although it is possible to update by not one but some worms simultaneously, we insert a new worm one by one after the previous worm vanishes. The efficiency of the multi-worm update needs to be investigated in the future. We perform several-time single worm updates in one

Monte Carlo step so that the total length of spin/boson worm trajectory averagely becomes $N\beta$ (the volume of the worldlines), where N is the number of sites and β is the inverse temperature. It is necessary, here, to tune the average of total path lengths. If we set a definite number of inserted worms in one Monte Carlo step, however, it is difficult to tune the length since the number is an integer. Instead of fixing, we stochastically determine the number at each Monte Carlo step from the Poisson distribution. Then we can tune the ratio as a continuous value by controlling the expecting value of the distribution.

3.4.3.3 Boson Worm Proceeding

The spin worm can certainly reach the next operator after scattering at an operator since the (exponential) weight that depends on

$$H_0 = H^p = \sum_r \omega a_r^\dagger a_r \qquad (3.51)$$

is not changed. This term, however, matters for the boson-worm move. Let us think of the worm-proceeding probability with the change in this weight. We consider the bosonic worm that is a pair of the creation operator $a^\dagger$ and the annihilation operator a on the occupation number basis. From the weight expression (3.7) in the continuous-time representation, the multiplied weight is $e^{-\tau\omega\Delta n}$ if the occupation number is changed in Δn during the interval time τ. When Δn is negative, the weight gets heavier. Thus, the head can certainly proceed in the time τ. On the other hand, when Δn is positive, the weight gets lighter. Hence, the probability that the head can proceed in τ is just the multiplied weight $e^{-\tau\omega\Delta n}$ from the Metropolis algorithm. The PDF of the stochastic process that the head goes in τ is expressed by

$$P(\tau) = \frac{e^{-\tau\omega\Delta n}}{\int_0^\infty d\tau e^{-\tau\omega\Delta n}} = \omega\Delta n e^{-\tau\omega\Delta n}. \qquad (3.52)$$

Therefore, this is the Poisson process again; the worm move is independent at each imaginary time. Then, the proceeding time can be generated by the exponential distribution.

In the simple model (3.15), there is no bosonic hopping term. For the dispersive phonon, however, such a kinetic term appears. Then also the bosonic worm scatters at the kinetic operators like the spin move we explained in the last subsection. We will introduce the hopping term for systems beyond the one-dimensional system later.

3.4.3.4 Warp Update

In the spin-Peierls model (3.15), we have to update the operator from $S_{r+1} \cdot S_r$ to $a_r S_{r+1} \cdot S_r$ or $a_r^\dagger S_{r+1} \cdot S_r$, or vice verse. However, the conventional worm update does not satisfy the ergodicity (irreducibility) in the present model, not including
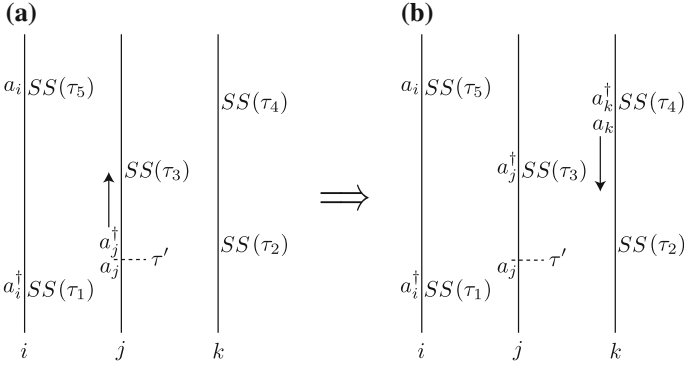
(a)   **(b)**

Fig. 3.6 Example of the warp update on the boson worldlines. The number i, j, and k are site indices, and these can be any site on the worldlines. An operator SS in the figure represents a spin operator linked to the boson worldline. In the boson worm update, it is not important which bond the spin operator is on

these updates. For ensuring the ergodicity, we introduce a new type of update, *the warp update*. Now suppose that we insert the worm at time τ' ($\tau_1 < \tau' < \tau_2$) on the boson worldline and move the head $a_j^\dagger$ upwards as illustrated in Fig. 3.6a. An operator SS in the figure represents a spin operator linked to the boson worldlines. In the boson worm update, the type of spin operator does not matter since the spin state is not changed during the update. When the head encounters $SS(\tau_3)$, we conduct the following update at once: We stop the head at operator $SS(\tau_3)$, which changes $SS(\tau_3)$ to $a_j^\dagger SS(\tau_3)$, insert a pair of a and $a\dagger$ at operator $SS(\tau_4)$, and move operator a_k as a new worm head, which also changes the operator from $SS(\tau_4)$ to $a_k^\dagger SS(\tau_4)$. By this update, the worm head *warps* from site j to site k (from time τ_3 to time τ_4), and the worldline configuration is updated from (a) to (b) in Fig. 3.6. Here site j and k can be any site on the worldlines. To sum up, when the head of boson worm $a^\dagger/a$ encounters an operator that has a spin term SS, we perform the following update:

- If the SS operator does not have a boson operator or has a conjugate operator to the head, do the following warp update. Otherwise, go straight or bounce.
- *warp update*
  - Choose an operator from all that includes a spin operator SS on the wold-lines.
  - Choose a pathway among candidate configurations with probabilities that satisfy the condition (3.47).

If the chosen operator is SS in the warp update, we have a choice that we insert a new worm at the operator SS on the worldline. If the chosen operator is $aSS/a^\dagger SS$, on the other hand, we have a choice that we move the trapped bosonic operator $a/a^\dagger$ as a new head. Note that this warp update can satisfy the ergodicity in the extended configuration space including the worm. This property is essential to measure the off-diagonal correlation functions as we mention in the next subsection. In practice,

how to determine the *warp* probability is not trivial since there are many possible pathways in this simultaneous update. Note that this warp trial is very often rejected if the simple Metropolis algorithm is used. However, we can indeed make the bosonic worm free from the bounce process at the operators by applying our geometric algorithms under the total balance condition (3.43) or (3.47).

3.4.4 Off-Diagonal Measurement

3.4.4.1 Correlation Function

In order to look into a lattice order in the spin-Peierls model (3.15), it is necessary to measure the correlation functions:

$$\langle q_r \, q_{r'} \rangle = \frac{1}{2\sqrt{mc}} \left\langle (a_r^\dagger + a_r)(a_{r'}^\dagger + a_{r'}) \right\rangle, \tag{3.53}$$

where the relation of the second quantization (3.2) is used. Here, $\langle a_r a_{r'} \rangle$ and $\langle a_r^\dagger a_{r'}^\dagger \rangle$ take nonzero values since the model does not conserve the boson number. Our method can precisely calculate also the lattice correlation by measuring boson operator correlations. Let us recall the definition of the thermal average:

$$\langle a_r a_{r'} \rangle = \frac{\operatorname{tr} a_r a_{r'} e^{-\beta H}}{\operatorname{tr} e^{-\beta H}}, \tag{3.54}$$

and take notice of each configuration that contributes to the denominator or the numerator in the right-hand side. It is original worldline configurations that contribute to the denominator. On the other hand, it is a part of the extended configurations with the worm that contribute to the numerator. The denominator is expressed as the sum of the weights of the original configurations, and the numerator is expressed as that of the partial extended configurations. Here, we need to be reminded that each configuration is visited with the frequency proportional to its defined weight in the Markov chain. This fact enables us to calculate the correlation function $\langle a_r a_{r'} \rangle$ by simply counting the frequency of visiting each configuration that contributes to the denominator or the numerator [22]. In order for this ratio to be unbiased, it is necessary to satisfy the ergodicity (irreducibility) in the extended configuration space. Our update method with the warp certainly ensures this condition.

In more detail, let us see an example of the way to calculate the correlation function $\langle a_j a_k \rangle$, where j and k are site indices. Now let us assume that after we inserted the boson worm on the worldline at imaginary time τ' (Fig. 3.7a), the worm warped from $SS(\tau_3)$ to $SS(\tau_4)$ (Fig. 3.7b) as mentioned in Sect. 3.4.3.4, and the worm head has moved downwards going straight at operator $SS(\tau_2)$. Then, the head passes the imaginary time τ' where the tail is on. When the head comes to just time τ', the extended configuration contributes to the numerator in the definition of $\langle a_j a_k \rangle$
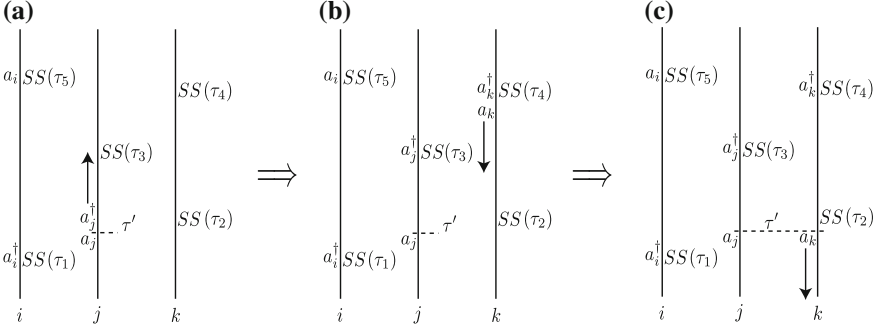
(a)   **(b)**   **(c)**

Fig. 3.7 Calculation of the correlation function $\langle a_j a_k \rangle$. When the worm head passes time τ' where the tail is on, we add the ratio of the weights $w_{\text{true}}/w_{\text{sim}}$, where the weight w_{true} is the weight when we assume the worm has the matrix element of the actual bosonic operator, and the weight w_{sim} is the weight that we use to construct the worm update

(Fig. 3.7c). Then, we store the ratio of the weights $w_{\text{true}}/w_{\text{sim}}$, where w_{true} is the weight of the configuration when we take into account the true matrix elements of the worm operators (head and tail), and the weight w_{sim} is the weight that we define to the extended configuration in the simulation. Although we can choose w_{sim} as the same with w_{true}, which eliminates the need of reweighting, it is better to optimize the weight w_{sim} so that the worm update becomes efficient. In our program, we set w_{sim} to $w_{\text{true}}/w_{\text{tail}}^2$, where w_{tail} is the true matrix element of the tail operator. By this select, the worm insertion and remove are accepted with probability 1 under the conditions (3.44) and (3.45), the bounce process can be completely eliminated at the operators, and the reweighting for off-diagonal correlations becomes easy since the factor is unchanged through one worm update. After several-time worm updates, we can finally evaluate the correlation function as $O_1/2O_2$, where observable O_1 is the sum of the reweighting factors $w_{\text{true}}/w_{\text{sim}}$ accumulated when the head a_j/a_k and the tail a_k/a_j exist at the same imaginary time, observable O_2 is the number of times that we *try* to insert the worm at the site j or k, and the factor 2 is the number of directions. The reason why we divide by O_2 is that we interpret the events of vanishing the worm or failing to insert the worm as meaning that one of original configurations is visited according to its original weight. The reason by 2, on the other hand, is because we doubly count the case where the head goes upwards and downwards (note that we assume that the direction does not matter to the weight). We emphasize that the conventional worm algorithm without the warp update cannot measure these correlation functions. For example, in the case where there is no other operator than illustrated in Fig. 3.7c on the whole worldlines, this extended configuration never appears during the simulation if we use the conventional worm update alone. Meanwhile, it is necessary to satisfy the ergodicity also in the extended configuration space including the worm for calculation of correlation functions. The present warp update is the most natural extension of the conventional worm update for satisfying the ergodicity of particle number nonconserving systems.

Although we have seen the example of calculation of the equal time correlation function $\langle a_j a_k \rangle$, we can similarly measure the dynamical correlation functions and other combination, e.g., $\langle a_j^\dagger a_k^\dagger \rangle$. When we intend to measure the dynamical correlation function $\langle a_j(\tau) a_k \rangle$, we sum up the reweighting factor just when the time interval between the head and the tail becomes τ.

3.4.4.2 One-body Operator

We will mention an another off-diagonal average with one-body operator here. We have seen that we can calculate effectively the off-diagonal correlation functions by using the worm with warp in the last section. Since the worm is the pair of operators, we can calculate two-point correlations by the worm. However, one-body off-diagonal averages, such as $\langle a \rangle$ and $\langle a^\dagger \rangle$, cannot be measured by the worm. In order to calculate these quantities, we introduce the *bug* update. The bug is a moving one-body operator on the worldlines as the worm without tail. Let us see an example of the bug update. When the configuration is as Fig. 3.8a (note that only a part of the configuration is illustrated), we insert a pair of bosonic operators (a_k and $a_k^\dagger$) at operator $SS(\tau_2)$ and pin one $a_k^\dagger$ to $SS(\tau_2)$, move the other a_k downwards as the bug with a certain probability (Fig. 3.8(a) $\rightarrow$ (b)). When the bug encounters operator $SS(\tau_1)$, we stochastically stop the bug at the operator (Fig. 3.8(b) $\rightarrow$ (c)). Next, let us see an another example of the bug update. When the configuration is as Fig. 3.8f, we move operator a_k of operator $a_k SS(\tau_1)$ upwards with a certain probability. When the bug encounters operator $a_k^\dagger SS(\tau_2)$, we vanish the bug and operator $a_k^\dagger$ stochastically. As we see, we insert or move the bug at operators SS or from $aSS/a^\dagger SS$ and stop or vanish the bug at operator SS or $a^\dagger SS/aSS$, respectively. Not having the tail, the bug can end at any operator including a spin term SS on the worldlines. This is the essential difference from the worm that necessarily ends at the insertion point. The probabilities in the bug update are determined in a manner similar to the worm. The difference is to include a configuration without the bug as a candidate. We also need to take into account the probability that the spin operator is chosen as a bug start point in the update.
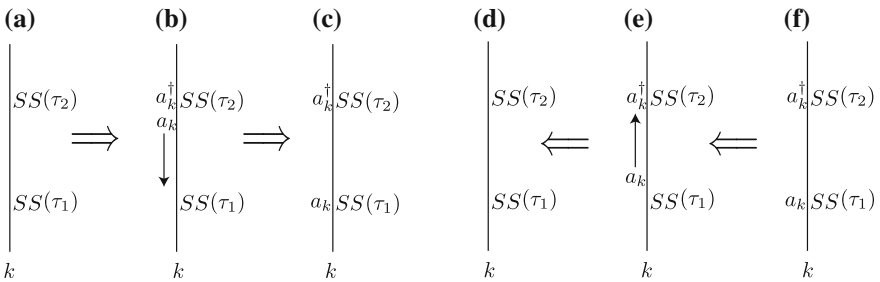

Fig. 3.8 Examples of the bug update where the bug moves from τ_2 to τ_1 and from τ_1 to τ_2

Through this bug move, we can measure one-body quantities $\langle a \rangle$ and $\langle a^\dagger \rangle$ in the same way as the two-body correlation functions (Sect. 3.4.4.1). In more detail, let us see an example of the way to calculate the average $\langle a \rangle$. When we intend to calculate the average $\langle a_k(\tau) \rangle$, where k is a site index, we simply count the frequency that the bug a_k passes through imaginary time τ on the worldline. Since the average $\langle a_k(\tau) \rangle$ is independent of the time from the cyclicity of the trace, it is better to integrate the total visiting time on site k and divide it by β. When the bug proceeds in $\Delta\tau$ (Fig. 3.8(b) $\rightarrow$ (c)), we store the value $\Delta\tau w_{\text{true}}/w_{\text{sim}}$, where w_{true} is the weight of the configuration including the true matrix element of a_k, and w_{sim} is the weight we define to the configuration in simulations. Finally, we can evaluate the average $\langle a_k \rangle$ as $O_1/2\beta O_2$, where observable O_1 is the sum of the reweighting factors $\Delta\tau w_{\text{true}}/w_{\text{sim}}$, observable O_2 is the number of times that we *try* to start the bug at site k, and the factor 2 is the number of directions in a similar way to the two-body correlation functions. Since the coordinate operator of the lattice degree of freedom is expressed as Eq. 3.2, we can calculate the average of position by measuring the averages $\langle a_r \rangle$ and $\langle a_r^\dagger \rangle$, which are available by our bug update. Also note that we do not warp the bug for simple calculations of the bug insertion/vanishment.

3.4.5 Programming Details

During the diagonal update we use some techniques in order to make the succeeding worm update easier and faster. One of them is the pre-determination of worm-insertion places. Instead of choosing an worm-starting point after the diagonal update, we insert worm-insertion points during the diagonal update. If we intend to make n points averagely, the weight for the exponential distribution should be $n\beta$. By this way, the ratio between the diagonal update amount and the off-diagonal update amount varies stochastically because the actual worm number fluctuates during the simulation. The merit of this pre-determination of insertion points is that we can store the information about the connection between the points and the surrounding operators before inserting the worms actually. Although it is normally costly to check if the worm comes back to the tail or not, we can do it easily by this manner.

Second is to insert the checkpoints at the both edge of the worldlines, that is, at imaginary time 0 and β. We need to check what time the worm passes in order to calculate correlation functions. If a case is considered where the worm goes through the imaginary-time boundary $\tau = 0$ and $\tau = \beta$, it costs some CPU time to get to know what time is passed. We can check this readily by inserting the end points of the worldlines. Though we insert the extra artificial points on the worldlines, they does not affect any physical quantities due to the memoryless property of worm move.

References

1. Beard, B. B., & Wiese, U. J. (1996). Simulations of discrete quantum systems in continuous Euclidean time. *Physical Review Letters*, *77*, 5130.
2. Bray, J., Hart, H. R., Interrante, L. V., Jacobs, I. S., Kasper, J. S., Watkins, G. D., et al. (1975). Observation of a spin-Peierls transition in a Heisenberg antiferromagnetic linear-chain system. *Physical Review Letters*, *35*, 744.
3. Chandrasekharan, S., Cox, J., Osborn, J., & Wiese, U. J. (2003). Meron-cluster approach to systems of strongly correlated electrons. *Nuclear Physics B*, *673*, 405.
4. Chandrasekharan, S., & Wiese, U. J. (1999). Meron-cluster solution of fermion sign problems. *Physical Review Letters*, *83*, 3116.
5. Cross, M. C., & Fisher, D. S. (1979). A new theory of the spin-Peierls transition with special relevance to the experiments on TTFCuBDT. *Physical Review B*, *19*, 402.
6. Evertz, H. G. (2003). The loop algorithm. *Advances in Physics*, *52*, 1.
7. Evertz, H. G., Lana, G., & Marcu, M. (1993). Cluster algorithm for vertex models. *Physical Review Letters*, *70*, 875.
8. Fukui, K., & Todo, S. (2009). Order-N cluster Monte Carlo method for spin systems with long-range interactions. *Journal of Computational Physics*, *228*, 2629.
9. Fukuyama, H., Tanimoto, T., & Saito, M. (1996). Antiferromagnetic long range order in disordered spin-Peierls systems. *Journal of the Physical Society of Japan*, *65*, 1182.
10. Geertsma, W., & Khomskii, D. (1996). Influence of side groups on 90 superexchange: A modification of the Goodenough-Kanamori-Anderson rules. *Physical Review B*, *54*, 3011–3014.
11. Handscomb, D. C. (1962). The Monte Carlo method in quantum statistical mechanics. *Proceedings of the Cambridge Philological Society*, *58*, 594.
12. Hase, M., Terasaki, I., & Uchinokura, K. (1993). Observation of the spin-Peierls transition in linear Cu^{2+} (spin-$\frac{1}{2}$) chains in an inorganic compound $CuGeO_3$. *Physical Review Letters*, *70*, 3651.
13. Henelius, P., Fröbrich, P., Kuntz, P. J., Timm, C., & Jensen, P. J. (2002). Quantum Monte Carlo simulation of thin magnetic films. *Physical Review B*, *66*, 094407.
14. Iba, Y., Chikenji, G., & Kikuchi, M. (1998). Simulation of lattice polymers with multi-self-overlap ensemble. *Journal of the Physical Society of Japan*, *67*, 3327–3330.
15. Kawashima, N., & Harada, K. (2004). Recent development of world-line Monte Carlo methods. *Journal of the Physical Society of Japan*, *73*, 1379.
16. Kühne, R. W., & Löw, U. (1999). Thermodynamical properties of a spin-$\frac{1}{2}$ Heisenberg chain coupled to phonons. *Physical Review B*, *60*, 12125.
17. Matsumoto, M., Todo, S., Yasuda, C., & Takayama, H. (2002). Ground state of $S = 1$ Heisenberg ladders. *Progress of Theoretical Physics*, *145*(Suppl.), 221.
18. McKenzie, R. H., Hamer, C. J., & Murray, D. W. (1996). Quantum Monte Carlo study of the one-dimensional Holstein model of spinless fermions. *Physical Review B*, *53*, 9676–9687.
19. Michel, F., Evertz, H.G. (2007). Lattice dynamics of the Heisenberg chain coupled to finite frequency bond phonons. cond-mat p. arXiv:0705.0799v2.
20. Onishi, H., & Miyashita, S. (2000). Temperature dependence of spin and bond ordering in a spin-Peierls system. *Journal of the Physical Society of Japan*, *69*, 2634–2641.
21. Onishi, H., & Miyashita, S. (2003). Quantum narrowing effect in a spin-Peierls system with quantum lattice fluctuation. *Journal of the Physical Society of Japan*, *72*, 392.
22. Prokof'ev, N. V., Svistunov, B. V., & Tupitsyn, I. S. (1998). Exact, complete, and universal continuous-time world-line Monte Carlo approach to the statistics of discrete quantum systems. *Soviet Physics JETP*, *87*, 310.
23. Raas, C., Löw, U., Uhrig, G. S., & Kühne, R. W. (2002). Spin-phonon chains with bond coupling. *Physical Review B*, *65*, 144438.
24. Rieger, H., & Kawashima, N. (1999). Application of a continuous time cluster algorithm to the two-dimensional random quantum Ising ferromagnet. *European Physical Journal B: Condensed Matter Physics*, *9*, 233.

25. Sandvik, A. W. (1999). Multichain mean-field theory of quasi-one-dimensional quantum spin systems. *Physical Review Letters*, *83*, 3069.
26. Sandvik, A. W. (1999). Stochastic series expansion method with operator-loop update. *Physical Review B*, *59*(R14), 157.
27. Sandvik, A. W., & Campbell, D. K. (1999). Spin-Peierls transition in the Heisenberg chain with finite-frequency phonons. *Physical Review Letters*, *83*, 195.
28. Seidel, A., Marianetti, C. A., Chou, F. C., Ceder, G., & Lee, P. A. (2003). $S = \frac{1}{2}$ chains and spin-Peierls transition in TiOCl. *Physical Review B*, *67*, 020405R.
29. Suzuki, M. (1976). Relationship between d-dimensional quantal spin systems and $(d + 1)$-dimensional Ising systems. *Progress of Theoretical Physics*, *56*, 1454.
30. Swendsen, R. H., & Wang, J. S. (1987). Nonuniversal critical dynamics in Monte Carlo simulations. *Physical Review Letters*, *58*, 86.
31. Syljuasen, O. F. (2003). Directed loop updates for quantum lattice models. *Physical Review E*, *67*, 046701.
32. Syljuasen, O. F., & Sandvik, A. W. (2002). Quantum Monte Carlo with directed loops. *Physical Review E*, *66*, 046701.
33. Uchinokura, K. (2002). Spin-Peierls transition in $CuGeO_3$ and impurity-induced ordered phases in low-dimensional spin-gap systems. *Journal of Physics: Condensed Matter*, *14*, R195–R237.
34. Werner, R., Gros, C., & Braden, M. (1999). Microscopic spin-phonon coupling constants in $CuGeO_3$. *Physical Review B*, *59*, 14356–14366.

Chapter 4
Quantum Monte Carlo Level Spectroscopy

4.1 Scaling from Finite-Size Data

We will introduce an efficient scaling method for investigating systems with strong finite-size effect and develop a combination with the QMC method in this chapter. In many continuous transitions, physical quantities diverge in a power-law form at transition point. The finite-size scaling method [5], where the critical exponents are fitted as parameters from data of finite-size systems according to the scaling hypothesis, can perform for such a continuous transition and correctly give the transition point and the universality class. However, for the Kosterlitz-Thouless (KT) transition, where physical quantities, e.g., the correlation length, exponentially diverge at the critical point, this conventional finite-size scaling method does not work because exponentially large system sizes are needed for the scaling. As an example, Seiler et al. [42] mistakenly concluded the universality class of the phase transition in the $Z(10)$ clock model as not the KT transition, which is analytically confirmed, but the continuous transition following a power-law form. Also Edwards et al. [14] pointed out that it is extremely difficult to distinguish between the KT and power-law scaling scenarios from reachable system-size data; the critical exponents can be wrongly fitted by a power-law form even if it is actually the KT transition.

For overcoming the difficulty of the KT-transition analysis in one-dimensional quantum systems, the level spectroscopy was invented [34–38]. Let us consider the $S = 1/2$ frustrated J_1-J_2 spin chain model described as

$$H = J_1 \sum_r (S_r^x S_{r+1}^x + S_r^y S_{r+1}^y + \Delta S_r^z S_{r+1}^z) + J_2 \sum_r (S_r^x S_{r+2}^x + S_r^y S_{r+2}^y + \Delta S_r^z S_{r+2}^z).$$
(4.1)

This model is an effective model of our spin-Peierls model and a good example where the level spectroscopy powerfully performs. Now, let us consider the isotropic case $\Delta = 1$. The ground state phase diagram is characterized by the ratio $\alpha = J_2/J_1$. For $\alpha = 0$, the system is reduced to the simple Heisenberg spin; the ground state is the Tomonaga-Luttinger (TL) liquid state, and the excitation is gapless, which is

obtained by des Cloizeaux and Pearson [11]. On the other hand, for $\alpha = 1/2$, the system is at the Majumdar-Ghosh point [31]; the ground state is simply the direct product of local spin singlets and doubly degenerated, and the excitation has a gap. Therefore, the quantum phase transition between the liquid phase and the dimer phase occurs in $0 \leq \alpha \leq 1/2$.

Several theoretical approaches have been applied to determine the transition point. Haldane [19] transformed the isotropic model into the effective spinless fermion model via the Jordan-Wigner transformation. Taking the continuum limit and applying the renormalization group argument, he predicted the phase transition point at $\alpha = 1/6$. Kuboki and Fukuyama [30] further transformed the fermions into the phase Hamiltonian by means of the bosonization method. They predicted the critical value is $\alpha = 1/3$, pointing out Haldane had an invalid treatment for an oscillating term of the fermionic field. In the meantime, Tonegawa and Harada [46] numerically diagonalized the finite-size original spin Hamiltonian. They concluded the phase boundary exists at $\alpha = 0.30 \pm 0.01$, finding the point where the singlet-triplet gap becomes zero. Due to the strong finite-size effect (logarithmic correction from marginal term), however, it is difficult to judge that the gap becomes zero or finite after extrapolating it to the thermodynamic limit.

In order to improve the accuracy of the extrapolation, Okamoto and Nomura [38] discussed the level crossing of the excitation energies. In the liquid phase of the J_1-J_2 model, the first excitation is labeled as the $S = 1$ triplet state that has the wavenumber $k = \pi$, being predicted by the spin wave theory. In the dimer phase, on the other hand, the first excitation is labeled as the $S = 0$ singlet state that has also the wavenumber $k = \pi$. This excitation gap gets exponentially small as the system size becomes large, and the ground state is doubly degenerate in the thermodynamic limit. Therefore, these different excitation gaps intersect at the transition point. Okamoto and Nomura [38] showed the two gaps linearly cross on α axis and the size dependence of the crossing point is free from the logarithmic correction. Extrapolating the point obtained by the exact diagonalization method, they clarified the critical point as $\alpha = 0.2411 \pm 0.0001$. Also for anisotropic cases, such quantities without logarithmic correction can be made by combining several critical dimensions, as we will show for the spin-Peierls model in Chap. 5. As the above discussion, the elimination of the problematic correction terms is the key strategy in the level spectroscopy.

4.2 J_1-J_2 and Sine-Gordon Model

We will, next, consider the phase diagram of the J_1-J_2 model (4.1) for $\Delta \geq 0$. Let us follow the discussion of Ref. [35]. The spin degree of freedom in the one-dimensional quantum model is transformed to the spinless fermion by the Jordan-Wigner transformation. With the abelian bosonization technique to the fermion, the original Hamiltonian (4.1) can be mapped into the quantum sine-Gordon model [30]:

$$H_{\mathrm{SG}} = \frac{v}{2\pi} \int dx \left[K(\pi\Pi)^2 + \frac{1}{K}(\partial_x\phi)^2 \right] + \frac{2g_\phi}{(2\pi a)^2} \int dx \cos\sqrt{8}\phi, \quad (4.2)$$

where the commutation relation

$$\left[\phi(x), \Pi(x')\right] = i\delta(x - x') \quad (4.3)$$

holds, and a is the lattice constant. The spin velocity v, and the Luttinger parameter K, and the coupling constant g_ϕ are related to α, Δ through

$$v = 2\sqrt{AC} \qquad K = \frac{1}{2\pi}\sqrt{\frac{C}{A}} \qquad g_\phi = -2\pi^2 a^2 D, \quad (4.4)$$

where

$$A = \frac{a}{8\pi}\left(1 + \frac{3\Delta}{\pi} + \frac{(6+\Delta)\alpha}{\pi}\right) \quad (4.5)$$

$$C = 2\pi a\left(1 - \frac{\Delta}{\pi} - \frac{(2-\Delta)\alpha}{\pi}\right) \quad (4.6)$$

$$D = \frac{1}{2a}(\Delta - (2+\Delta)\alpha). \quad (4.7)$$

These expressions are reliable only near $\Delta = 0$ and $\alpha = 0$. The quantities v and K for $\alpha = 0$ can be exactly evaluated from the Bethe ansatz [7] as

$$v = Ja\frac{\pi\sqrt{1-\Delta^2}}{2\cos^{-1}\Delta} = Ja\frac{\sin(\pi\eta)}{2(1-\eta)} \quad (4.8)$$

$$K = \frac{\pi}{\pi - \cos^{-1}\Delta} = \frac{1}{\eta}. \quad (4.9)$$

where, η is the critical exponent of two-point spin-correlation functions. The dual field $\theta(x)$ is defined as $\partial_x\theta(x) = \pi\Pi(x)$. Here we compactify the scalar boson fields as $\phi \equiv \phi + \sqrt{2}\pi$, and $\theta \equiv \theta + \sqrt{2}\pi$, which restores the $U(1)$ symmetry of the spinless fermion field.

For the free field theory, the operator $\exp(\pm im\sqrt{2}\phi)$ has the scaling dimension $Km^2/2$, and the operator $\exp(\pm in\sqrt{2}\theta)$ has $n^2/2K$, where integer variables m and n are magnetic and electric charges, respectively, in the Coulomb gas picture [23]. At the Heisenberg point ($\Delta = 1$), the Luttinger parameter $K = 1$, and the scaling dimension of the cosine interaction term becomes 2; that is, it is a marginal operator. From the relations (4.4) and (4.7), the next-nearest interaction reduces the marginal operator. When the marginal term becomes zero, the phase transition occurs. It is, however, not possible to determine the accurate phase boundary from only these relations (although Kuboki et al. [30] concluded the transition point from this formula).
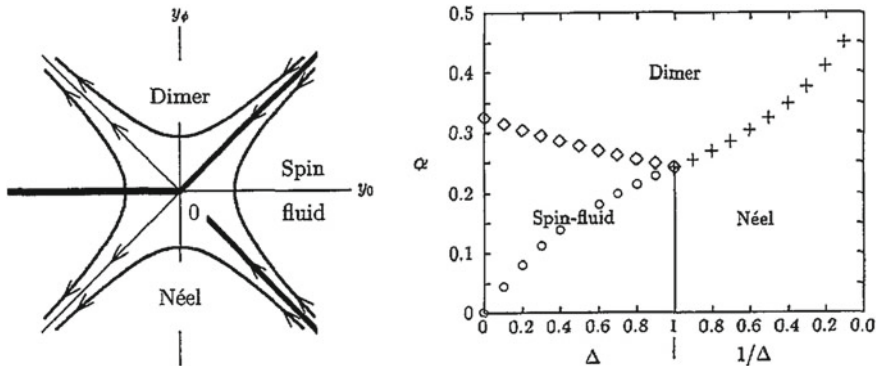
Fig. 4.1 Renormalization flow (*left*) in the quantum sine-Gordon model and the phase diagram (*right*) of the J_1-J_2 model (4.1). In the left figure, the corresponding phases of the J_1-J_2 model are shown. Although the renormalization-group equation (4.10) does not produce the accurate transition point, it is possible to determine the phase boundary from the level crossing by the numerical diagonalization method. These figures are taken from Ref. [35]

Nevertheless, the renormalization group analysis illuminates the aspect of the phase diagram.

The renormalization-group equations up to the lowest order are

$$\frac{dy_0(\ell)}{d\ell} = -y_\phi^2(\ell) \qquad \frac{dy_\phi(\ell)}{d\ell} = -y_\phi(\ell)y_0(\ell), \qquad (4.10)$$

where

$$y_0(0) = \frac{g_0}{\pi u} \qquad y_\phi(0) = \frac{g_\phi}{\pi u} \qquad K = 1 + \frac{g_0}{2\pi u}. \qquad (4.11)$$

The renormalization flow is shown in Fig. 4.1. For the finite spin system, ℓ is related to the number of site L by $e^\ell = L$. There are three phases: the TL liquid phase, the dimer phase, and the Néel phase. The quantum phase transition between the TL liquid phase and the dimer/Néel phase becomes the KT type. By contrast, the transition between the Néel phase and the dimer phase belongs to the Gaussian universality class, where the critical exponent continuously varies. Meanwhile, as a numerical method for determining the fixed point from finite-size data, the phenomenological renormalization-group method have been applied to many systems [33]. It is, however, noteworthy that Inoue and Nomura [21] showed *analytically* the phenomenological renormalization-group equation gives a wrong fixed point owing to the finite-size corrections for the KT transition.

Then, Nomura and Okamoto [35] developed the level spectroscopy and determined the phase boundary. Moreover, they accurately identified the universality class of the phase transitions, showing the logarithmic correction can be eliminated in a combination of the scaling dimensions of the relevant, irrelevant, and marginal operators. The tactically combined quantities enable us to take a correct extrapolation to

the thermodynamic limit. As we will see in Chap. 5, we can investigate the phase transition of the spin-Peierls model with the help of this level spectroscopy.

4.3 Accurate Gap Estimation

We will introduce a new estimator sequence in this section for accurately calculating an excitation gap, which is utilized for the level spectroscopy. For small systems, it is easy to get the gap by the exact diagonalization method. For large systems, however, the diagonalization is not feasible. In the meanwhile, it is not trivial to get precise spectrum information from QMC data. Note that it is impossible so far, in most cases, to simulate dynamics of large quantum systems.[1] We need to obtain the gap from equilibrium simulations, but it cannot be expressed as an expectation value of a certain operator.

The spectral information is hidden in the imaginary-time (dynamical) correlation function:

$$
\begin{aligned}
C(\tau) &:= \langle \hat{O}^\dagger(\tau)\hat{O} \rangle \\
&= \frac{1}{Z} \mathrm{tr} \left[e^{\tau H} \hat{O}^\dagger e^{-\tau H} \hat{O} e^{-\beta H} \right] \\
&= \frac{1}{Z} \sum_{\ell,\ell'} \langle \ell | e^{-(\beta-\tau)E_\ell} \hat{O}^\dagger | \ell' \rangle \langle \ell' | e^{-\tau E_{\ell'}} \hat{O} | \ell \rangle \\
&= \frac{1}{Z} \sum_{\ell,\ell'} \left| \langle \ell' | \hat{O} | \ell \rangle \right|^2 e^{-\tau(E_{\ell'}-E_\ell)} e^{-\beta E_\ell},
\end{aligned}
\tag{4.12}
$$

where $\hat{O}(\tau) = e^{\tau H} \hat{O} e^{-\tau H}$ is an operator at τ, $\langle \hat{A} \rangle = \mathrm{tr} \left[A e^{-\beta H} \right] / Z$ is the thermal average of $\hat{A}$ (β is the inverse temperature), $Z = \mathrm{tr} \left[e^{-\beta H} \right]$ is the partition function, E_ℓ and $|\ell\rangle$ are the eigenvalue and eigenstate of the Hamiltonian as $H|\ell\rangle = E_\ell|\ell\rangle$, respectively. The set of eigenvectors $\{|\ell\rangle\}$ is complete in the Hilbert space and the identity operator $\sum_\ell |\ell\rangle\langle\ell| = 1$ is inserted. We use a Fourier transformed operator:

$$
\hat{O}_k = \frac{1}{\sqrt{N}} \sum_r \hat{O}_r e^{ikr},
\tag{4.13}
$$

where N is the number of sites in a lattice system. Let us here consider the hermitian operators for simplicity, Then, because the following relation satisfies for the hermitian operators

$$
\left| \langle \ell | \hat{O} | \ell' \rangle \right|^2 = \left| \langle \ell | \hat{O}^\dagger | \ell' \rangle \right|^2,
\tag{4.14}
$$

---

[1] These days some quantum dynamics have been investigated [18, 48] by the real-time QMC simulation using the dynamical mean-field theory and the Keldysh formalism. The difficulty of the negative sign is alleviated by reducing the expansion order.

the correlation function (4.12) is rewritten as

$$C(\tau) = \frac{1}{Z} \sum_{\langle \ell, \ell' \rangle} \left| \langle \ell | \hat{O} | \ell' \rangle \right|^2 \left[e^{-\tau(\Delta E)_{\ell\ell'}} e^{-\beta E_\ell} + e^{\tau(\Delta E)_{\ell\ell'}} e^{-\beta E_{\ell'}} \right]$$

$$= \frac{1}{Z} \sum_{\langle \ell, \ell' \rangle} \left| \langle \ell | \hat{O} | \ell' \rangle \right|^2 \frac{2}{e^{-\frac{\beta}{2}(E_\ell + E_{\ell'})}} \cosh \left[\left(\tau - \frac{\beta}{2} \right) (\Delta E)_{\ell\ell'} \right], \quad (4.15)$$

where $(\Delta E)_{\ell\ell'} = E_{\ell'} - E_\ell$, and $\langle \ell, \ell' \rangle$ is a pair of the eigenstates $|\ell\rangle$ and $|\ell'\rangle$, respectively.

Let us consider the Fourier transformation at the Matsubara frequency $\omega_j = 2\pi j/\beta$ (j is an integer):

$$\tilde{C}(\omega_j) := \int_0^\beta d\tau C(\tau) e^{i\tau\omega_j}$$

$$= \frac{1}{Z} \sum_{\langle \ell, \ell' \rangle} \left| \langle \ell | \hat{O} | \ell' \rangle \right|^2 \frac{2}{e^{-\frac{\beta}{2}(E_\ell + E_{\ell'})}} \int_0^\beta d\tau \cosh \left[\left(\tau - \frac{\beta}{2} \right) (\Delta E)_{\ell\ell'} \right] e^{i\tau\omega_j}$$

$$= \frac{1}{Z} \sum_{\langle \ell, \ell' \rangle} \left| \langle \ell | \hat{O} | \ell' \rangle \right|^2 \frac{2}{e^{-\frac{\beta}{2}(E_\ell + E_{\ell'})}} \sinh \left(\frac{\beta}{2} (\Delta E)_{\ell\ell'} \right) \frac{2(\Delta E)_{\ell\ell'}}{\omega_j^2 + (\Delta E)_{\ell\ell'}^2}$$

$$= \frac{1}{Z} \sum_{\langle \ell, \ell' \rangle} \left| \langle \ell | \hat{O} | \ell' \rangle \right|^2 \left(e^{-\beta E_\ell} - e^{-\beta E_{\ell'}} \right) \frac{2(\Delta E)_{\ell\ell'}}{\omega_j^2 + (\Delta E)_{\ell\ell'}^2}. \quad (4.16)$$

When the periodic boundary condition holds in the real space, the similar expressions with Eqs. (4.15) and (4.16) are derived also for $k \neq \pi$. By taking the limit $\beta \to \infty$, the asymptotic forms of the correlation functions become

$$C(\tau) \quad \to \quad \sum_\ell \left| \langle \ell | \hat{O} | gs \rangle \right|^2 e^{-\tau(\Delta E)_\ell} \quad (4.17)$$

$$\tilde{C}(\omega) \quad \to \quad \sum_\ell \left| \langle \ell | \hat{O} | gs \rangle \right|^2 \frac{2(\Delta E)_\ell}{\omega^2 + (\Delta E)_\ell^2}. \quad (4.18)$$

In the expression, we write the ground state as $|gs\rangle$ and the excitation energy of state $|\ell\rangle$ as $(\Delta E)_\ell$. The states $|\ell\rangle$ satisfying the condition $\langle \ell | \hat{O} | gs \rangle \neq 0$ are labeled as $(\Delta E)_1 \leq (\Delta E)_2 \leq \cdots$. Here, we assume the conditions

$$\hat{O}|gs\rangle \neq 0 \quad (4.19)$$

$$\langle gs | \hat{O} | gs \rangle = 0 \quad (4.20)$$

in order for the following method to work. For example, in the case where the latter equation is not satisfied, the susceptibility $\tilde{C}(0)$ trivially diverges.

If we take the analytic continuation from the Matsubara frequencies to the real axis, we will get the spectral function. Such a transformation, however, is known as an ill-posed problem and numerically very difficult like the inverse Laplace transformation, where the result is not stable to a small input perturbation. Nevertheless, some effective methods have been proposed to acquire the spectrum information from the QMC data. One example, which is probably the simplest way to know the lowest gap, is to measure dumping of the imaginary-time correlation; the lowest excitation gap dominates in large τ limit, and the dumping factor becomes $(\Delta E)_1$ expressed as Eq. (4.17). Another example is the maximum entropy method [17, 20, 40, 43, 44], where one assumes the spectral function form and reconciles the assumption and noisy data by means of the Bayesian inference. It is often possible to elicit the whole spectral information by this approach. Although this method is of interest from the viewpoint of statistics, the accuracy depends greatly on the assumption and parameters. Particularly, it is extremely difficult to obtain the lowest gap value.

We, then, extend the moment method [12] to estimate the gap, focusing the attention on the correlations at the Matsubara frequencies (4.18). Again note that the problem is to estimate the gap $(\Delta E)_\ell$ or the imaginary-time correlation length $\xi_\ell = 1/(\Delta E)_\ell$, given the correlations $\tilde{C}(\omega_j)$ that necessarily have a statistical error. Particularly let us consider estimating ξ_1 or $(\Delta E)_1$. Here, we cannot directly solve the nonlinear simultaneous equation (4.16) or (4.18). Let us consider the simplest case where the index ℓ takes only one state in Eq. (4.18). The correlation is simply expressed as

$$\tilde{C}^{(0)}(\omega_j) = \frac{b_1 \xi_1}{1 + \omega_j^2 \xi_1^2}, \tag{4.21}$$

where $b_1 = 2\left|\langle 1|\hat{O}|gs\rangle\right|^2$. Similarly, we define $b_\ell = 2\left|\langle \ell|\hat{O}|gs\rangle\right|^2$ below. This is nothing but the Ornstein-Zernike form, which expresses a correlation function derived from the mean-field treatment generally [8, 12]. Thus, the correlation length can be extracted as the so-called second moment

$$\hat{\xi}^{(0)} = \frac{1}{\omega_j}\sqrt{\frac{\tilde{C}(0)}{\tilde{C}(\omega_j)} - 1}. \tag{4.22}$$

Here the smallest frequency $\omega_j = \omega_1$ is usually used. This quantity becomes the exact correlation length ξ_1 when the correlation $\tilde{C}$ forms as $\tilde{C}^{(0)}$. In fact, it is also written as exactly the second moment

$$\xi_1^2 \sim \int d\tau\, \tau^2 \tilde{C}^0(\tau), \tag{4.23}$$

where $\tilde{C}^{(0)}(\tau) = \int d\omega\, \tilde{C}^{(0)}(\omega)e^{i\tau\omega} \sim e^{-\tau/\xi_1}$. This approximated correlation length $\hat{\xi}^{(0)}$ is used in many QMC simulations. We have to carefully, however, take notice

that this estimator has not only statistical error but also systematic error. For $\beta \to \infty$, the systematic error is expressed as

$$\frac{\hat{\xi}^{(0)}}{\xi_1} \to 1 - \frac{1}{2} \sum_{\ell>1} \frac{b_\ell \, \xi_\ell}{b_1 \, \xi_1} + O\left(\left(\frac{\xi_\ell}{\xi_1}\right)^2\right). \tag{4.24}$$

In the meantime, the correlation length is utilized for finding the transition point and the critical exponent of many continuous transitions; the ratio ξ_1/L intersects at the transition point. Here we can use $\hat{\xi}^{(0)}/L$ instead. It is because the correction $\hat{\xi}^{(0)}/\xi_1$ is constant and does not depend on the system size although the lengths ξ_ℓ all diverge in proportional to L at the critical point. This finite-size scaling, however, does not work for the KT transition since the critical phase extend over the transition point.

For the level spectroscopy, even the above constant correction hinders us from extrapolating correctly. Let us consider eliminating the correction term in Eq. (4.24). As shown in the expression, $\hat{\xi}^{(0)}$ has the corrections from the first order of the ratio ξ_ℓ/ξ_1 (that's why the second moment corresponds to the 0-th order approximation). Then, we consider including the first order terms of ξ_ℓ in Eq. (4.18), and approximating the correlation function as

$$\tilde{C}^{(2)}(\omega_j) = \frac{b_1 \xi_1}{1 + \omega_j^2 \xi_1^2} + \sum_{\ell>1} b_\ell \xi_\ell. \tag{4.25}$$

We can elicit a higher order gap estimator [45] from this expression as

$$\hat{\xi}^{(2)} = \frac{1}{\omega_2} \sqrt{3 \frac{\tilde{C}(0) - \tilde{C}(\omega_1)}{\tilde{C}(\omega_1) - \tilde{C}(\omega_2)} - 1}. \tag{4.26}$$

If the correlation $\tilde{C}$ formed as $\tilde{C}^{(2)}$, this quantity would become the exact correlation length ξ_1. The actual systematic error for $\beta \to \infty$ is expressed as

$$\frac{\hat{\xi}^{(2)}}{\xi_1} \to 1 - \frac{1}{2} \sum_{\ell>1} \frac{b_\ell}{b_1} \left(\frac{\xi_\ell}{\xi_1}\right)^3 + O\left(\left(\frac{\xi_\ell}{\xi_1}\right)^4\right), \tag{4.27}$$

where the correction terms appear only over the second order of ξ_ℓ/ξ_1.

In a similar way, when we approximate the correlation as

$$\tilde{C}^{(4)}(\omega_j) = \frac{b_1 \xi_1}{1 + \omega_j^2 \xi_1^2} + \sum_{\ell>1} b_\ell \xi_\ell (1 - \omega_j^2 \xi_\ell^2), \tag{4.28}$$

a further higher order estimator

$$\hat{\xi}^{(4)} = \frac{1}{\omega_3} \sqrt{10 \frac{3\tilde{C}(0) - 4\tilde{C}(\omega_1) + \tilde{C}(\omega_2)}{5\tilde{C}(\omega_1) - 8\tilde{C}(\omega_2) + 3\tilde{C}(\omega_3)} - 1} \tag{4.29}$$

can be constructed.

For general order $n = 2p$ ($p \geq 2$), considering a generalized approximated correlation function

$$\tilde{C}^{(n)}(\omega_j) = \frac{b_1\xi_1}{1 + \omega_j^2\xi_1^2} + \sum_{\ell>1} b_\ell\xi_\ell \left(1 - \omega_j^2\xi_\ell^2 + \cdots + (-1)^{p-1}\omega_j^{2(p-1)}\xi_\ell^{2(p-1)}\right), \tag{4.30}$$

we obtain an gap estimator as

$$\hat{\xi}^{(n)} = \frac{1}{\omega_{p+1}} \sqrt{\alpha^{(n)} R^{(n)} - 1}, \tag{4.31}$$

where

$$\alpha = \frac{x_1 \prod_{k=1}^{p} k^2}{\sum_{i=1}^{p+1} y_i \prod_{k\neq i} k^2} \tag{4.32}$$

$$R^{(n)} = \frac{x_1\tilde{C}(0) + x_2\tilde{C}(\omega_1) + \cdots + x_{p+1}\tilde{C}(\omega_p)}{y_1\tilde{C}(\omega_1) + y_2\tilde{C}(\omega_2) + \cdots + y_{p+1}\tilde{C}(\omega_{p+1})}. \tag{4.33}$$

The coefficiencies are the solution of the following Vandelmonde linear problem:

$$V^t(1, 2^2, 3^2, \ldots, p^2)\tilde{x} = (-x_1, 0, 0, \ldots, 0)^t \tag{4.34}$$

$$V^t(1, 2^2, 3^2, \ldots, (p+1)^2)y = (0, 0, 0, \ldots, 0, s)^t \tag{4.35}$$

$$s = \sum_{k=1}^{p+1} k^n y_k, \tag{4.36}$$

where the Vandelmonde matrix is defined as:

$$V(z_1, z_2, \ldots, z_N) = \begin{bmatrix} 1 & z_1 & z_1^2 & \cdots & z_1^{N-1} \\ 1 & z_2 & z_2^2 & \cdots & z_2^{N-1} \\ \vdots & \vdots & \vdots & \ddots & \vdots \\ 1 & z_N & z_N^2 & \cdots & z_N^{N-1} \end{bmatrix}, \tag{4.37}$$

and the vectors as

$$\tilde{x} = (x_2, \ldots, x_{p+1})^t \tag{4.38}$$

$$y = (y_1, y_2, \ldots, y_{p+1})^t. \tag{4.39}$$

Note that the dimension of the solution vector space $x = (x_1, \tilde{x}^t)^t$ and y is one. Nonetheless, the product $\alpha^{(n)} R^{(n)}$ is unique. The systematic error becomes

$$\frac{\hat{\xi}^{(n)}}{\xi_1} \rightarrow 1 - O\left(\left(\frac{\xi_\ell}{\xi_1}\right)^{(n+1)}\right) \quad (\beta \rightarrow \infty). \tag{4.40}$$

This estimator is presumably unique when we are allowed to use only $\tilde{C}(0)$, $\tilde{C}(\omega_1) \cdots$ $\tilde{C}(\omega_{p+1})$, on condition that the terms until (n)-th order of the ratio ξ_ℓ/ξ_1 are correctly included. Because the statistical error of a linear combination increases as the number of used estimators, this is an optimal estimator for the gap calculation. We can calculate the first excitation gap more accurately; the systematic error of the estimators becomes zero in $\beta \rightarrow \infty$ and $n \rightarrow \infty$. Note that the higher-order estimator has a larger statistical error. Thus, we need to carefully confirm the convergence as we will see in the following example.

Let us check the validity of the estimators. Figure 4.2 shows the estimated triplet gap w.r.t. temperature T in the spin-Peierls model (3.15) with parameters $L = 4$, $\omega = 4$, $\lambda = 1/2$, $D = 4$, where D is the cutoff of the boson occupation number and it is restricted less than D in the simulation. One hand, the conventional second moment seems to converge to a wrong value at $T = 0$ because of the systematic error. The improved gap estimator, on the other hand, converges to the exact value. Surprisingly,
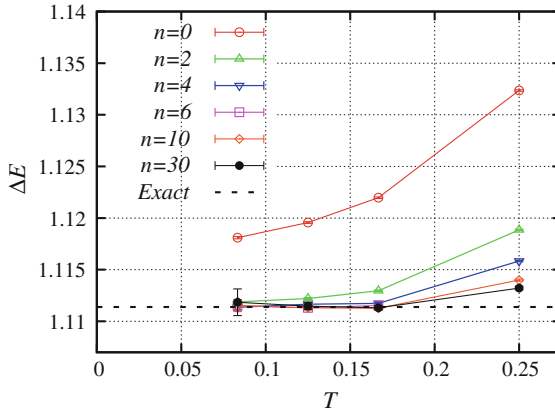

Fig. 4.2 Triplet gap ($S = 1$) of the spin-Peierls model 3.15 w.r.t. temperature with parameters $L = 4$, $\omega = 4$, $\lambda = 1/2$, $D = 4$, where D is the cutoff of the boson occupation number. The boson number in the simulation is restricted less than D. The periodic boundary condition is used, and the true value calculated by the exact diagonalization method is shown together. The each-order estimator is calculated by different simulations. The higher order gap estimators converge to the exact value much more rapidly than the usual second moment $n = 0$

the higher order estimators already converge in relatively high temperature. As we see, the introduced gap estimators powerfully perform and enable us to apply the correct level spectroscopy analysis.

4.4 Demonstration in Alternating-Bond Model

We demonstrate, in this section, the usefulness of the level spectroscopy in the following $S = 1$ alternating-bond model:

$$H = \sum_{r=1}^{N} J(1 - \delta(-1)^r)[S_r^x S_{r+1}^x + S_r^y S_{r+1}^y + \Delta S_r^z S_{r+1}^z]. \qquad (4.41)$$

In order to understand the phase diagram with the hidden $Z_2 \times Z_2$ symmetry, we introduce the one-dimensional quantum Ashkin-Teller model

$$H_{\text{AT}} = -\beta \sum_{r=1}^{N} [\sigma_r^z \sigma_{r+1}^z + \tau_r^z \tau_{r+1}^z + \lambda \sigma_r^z \sigma_{r+1}^z \tau_r^z \tau_{r+1}^z] - \sum_{r=1}^{N} [\sigma_r^x + \tau_r^x + \lambda \sigma_r^x \tau_r^x],$$

$$(4.42)$$

where $\sigma_r^{x,z}$, $\tau_r^{x,z}$ are Pauli matrices. This Hamiltonian is invariant under $\sigma^z \leftrightarrow -\sigma^z$ and $\tau^z \leftrightarrow -\tau^z$ transformations, holding $Z_2 \times Z_2$ symmetry. A duality transformation

$$\tilde{\sigma}_{r+1/2}^x = \sigma_r^z \sigma_{r+1}^z, \qquad \tilde{\sigma}_{r+1/2}^z = \prod_{\ell < r} \sigma_\ell^x, \qquad (4.43)$$

$$\tilde{\tau}_{r+1/2}^x = \tau_r^z \tau_{r+1}^z, \qquad \tilde{\sigma}_{r+1/2}^z = \prod_{\ell < j} \tau_\ell^x \qquad (4.44)$$

gives the relation between the parameters as

$$H_{\text{AT}}(\lambda, \beta) = \beta H_{\text{AT}}(\lambda, 1/\beta). \qquad (4.45)$$

On the line $\beta = 1$, the system has the self-duality as in Fig. 4.3. According to Kohmoto, den Nijs and Kadanoff [27], the quantum Ashkin-Teller model (4.42) can be mapped to the $S = 1/2\ XXZ$ chain model with bond alternation, which is the same form with the Hamiltonian (4.41), through the relation $\Delta = \lambda, \delta = (1-\beta)/(1+\beta))$. The Gaussian critical line corresponds to the $\delta = 0$ line ($1/\sqrt{2} < \Delta < 1$), and the bifurcation point ($\Delta = 1, \delta = 0$) to the 2D Ising critical lines exists as in Fig. 4.3. The universality class of the point is the $k = 1, SU(2)$ Wess-Zumino-Witten (WZW) model [2, 49].

An effective model of the spin-$S\ XXZ$ chain model with bond alternation [41] or the quantum Ashkin-Teller model [22] is the double-frequency sine-Gordon model:
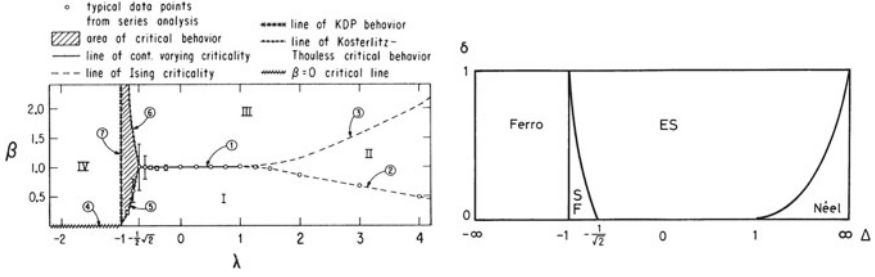
Fig. 4.3 Phase diagram of the quantum Ashkin-Teller model (*left*) and the $S = 1/2$ alternating-bond model (*right*). In the *left* panel, there is the Gaussian critical line ($\beta = 1$, $-1/\sqrt{2} < \lambda < 1$) of continuously varying critical exponents. At the end of the line ($\beta = 1$, $\lambda = 1$), this line breaks up into two 2D Ising critical lines. The Gaussian critical line separates the fully ordered and the fully disordered phases of the $Z_2 \times Z_2$ symmetry, and a partial symmetry is broken over the Ising critical lines. The *left* figure is taken from Ref. [27], and the *right* figure from Ref. [39]

$$H_{SG2} = \frac{v}{2\pi} \int dx \left[K(\pi \Pi)^2 + \frac{1}{K} (\partial_x \phi)^2 \right] + \frac{y_1 v}{2\pi a^2} \int dx \cos \sqrt{2}\phi$$
$$+ \frac{y_2 v}{2\pi a^2} \int dx \cos \sqrt{8}\phi. \tag{4.46}$$

The correspondence to the bond alternation model is as $y_1 \propto \delta$, (4.8), and (4.9). To the quantum Ashkin-Teller model, on the other hand, it is as

$$y_1 \propto \frac{1 - \beta}{1 + \beta}, \qquad K = \frac{\pi}{\arccos \lambda}, \tag{4.47}$$

shown in Ref. [27]. Delfino et al. [13] and Fabrizio et al. [15] showed that the renormalization-group trajectory flows to the Gaussian fixed point when the $\cos \sqrt{2}$ term is relevant but the $\cos \sqrt{8}$ term is irrelevant. Then the fixed point is changed to the Ising type once the $\cos \sqrt{8}$ term becomes also relevant. This property is essential to also the criticality of the spin-Peierls model; the static alternation changes the universality class of the phase transition.

Here, we demonstrate the level spectroscopy for the isotropic case ($\Delta = 1$) of the $S = 1$ alternating-bond model, combining with the QMC technique and the new gap estimators introduced in the last section. The phase transition from the Haldane phase to the dimer phase occurs at a finite alternation δ_c. Affleck and Haldane [1, 3] mapped this model to the nonlinear $O(3)$ σ-model. They showed that the topological angle θ is given by $\theta = 2\pi S(1 - \delta)$ and the system should be massless when $\theta/2\pi$ is half odd integer. Numerically, Kato and Tanaka [24] obtained the critical point at $\delta_c = 0.25 \pm 0.01$ and $c \sim 1$ by using the density matrix renormalization group. Yamamoto [50] showed a consistent result by the QMC method. Totsuka et al. [47] identified the universality class as the $SU(2)$ $k = 1$ WZW model. More precisely, Kohono et al. [28] estimated $\delta_c = 0.2595(5)$ by the QMC calculation for

the susceptibility, and Nakamura et al. [32] obtained $\delta_c = 0.25997(3)$ by using the interesting order parameter that characterizes the valence-bond states.

As a noteworthy research, Kitazawa et al. [26] identified $\delta_c = 0.2598$ by observing the level crossing from small-size data $L \leq 16$, where L is the number of spins. They clarified the critical dimensions corresponding to each symmetry operation from the renormalization equations as in Fig. 4.4 and succeeded in eliminating the logarithmic correction. In the right table, q, S_T^z, P, and T represent the wavenumber, the total S^z, the parity of the space inversion, and the spin reversal, respectively. We observe the level crossing of the two excitations [25], ($S_T^z = 0$, $P = 1$, $T = 1$) and ($S_T^z = 0$, $P = -1$, $T = -1$) under the $\Phi = \pi$ twisted boundary condition (TBC) [16, 29]:

$$S_{L+1}^x = S_1^x \cos \Phi - S_1^y \sin \Phi \tag{4.48}$$
$$S_{L+1}^y = S_1^x \sin \Phi + S_1^y \cos \Phi. \tag{4.49}$$

In the QMC method, under the TBC, the sign of the weight becomes negative when the winding number of the worldlines is odd. Then we simulate under the periodic boundary condition (PBC) and reweight the averages as conducted for the usual negative sign problem. Figure 4.5 shows the ground state ($S_T = 0$, $S_T^z = 0$, where S_T represents the total spin) energy and the singlet gap labeled as $S_T = 1$, $S_T^z = 0$ under the TBC measured from the ground state energy under the PBC. These energy gaps meet at the critical point; that is the system is gapless under the TBC (doubly degenerated). Note that the wavenumber of the doublet excitation state ($S_T = 1$, $S_T^z = \pm 1$) is shifted, under the TBC [29], in π/L and it has a gap. It is clear that the conventional second moment ($n = 0$ in the figure) has a large gap from the peak of the ground state energy near the transition point, but the higher-order estimators get close to it. We, here, need to be reminded that the parities of the space inversion and the spin reversal for the ground state and the singlet excited state under the TBC are changed across the transition point [26]. That is, for the singlet state, the symmetries are even in the Haldane phase, but odd in the dimer phase. For the ground state, on the other hand, they are odd in the Haldane phase but even in the dimer phase, which is clear in the Schwinger boson picture [4]. Therefore, the first excitation state that belongs to each parity switches with each other.

The level-crossing point between the two excitations, ($S_T^z = 0$, $P = 1$, $T = 1$) and ($S_T^z = 0$, $P = -1$, $T = -1$) under the TBC, is shown w.r.t. $1/L^2$ in Fig. 4.6 together with the crossing point $z_L = 0$, where z_L is the order parameter proposed by Nakamura et al. [32]. They identified the transition point by extrapolating the crossing point $z_L = 0$ to $L \to \infty$. As for our calculation, we expected that the transition point is located near $\delta = 0.26$ from Fig. 4.5 as expected from the previous results. Then, we estimated the crossing point of the two excitations by interpolating the data at $\delta = 0.25$ and 0.27. On one hand the $z_L = 0$ point suffers from the logarithmic correction and does not seem to converge to the true value from these size data (they concluded $\delta_c = 0.25997(3)$ from the simulations up to $L = 320$). We see, on the other hand, the crossing point converges near the expected value very
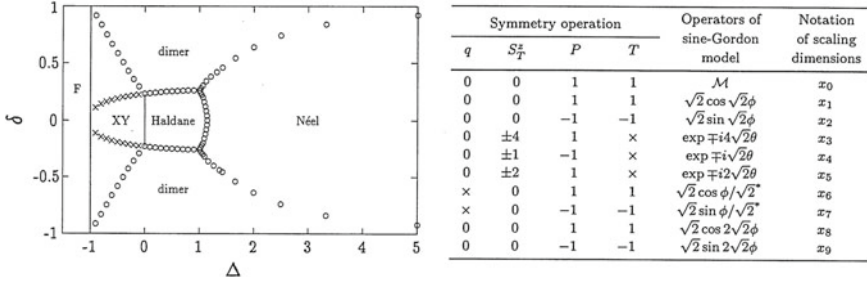
Fig. 4.4 Phase diagram of the $S = 1$ alternating-bond model (*left*) and the table of the relation between the symmetry operations and the operators in the sine-Gordon model (*right*). We demonstrate the level crossing at the phase transition between the Haldane phase and the dimer phase for $\Delta = 1$. The symbols q, S_T^z, P, and T are explained in the body text. The two operators with * in the *right* are defined under the $\Phi = \pi$ twisted boundary condition. The top operator $\mathcal{M}$ is a special marginal operator that is the Lagrangian density for the free field theory. These figures are taken from Ref. [26]
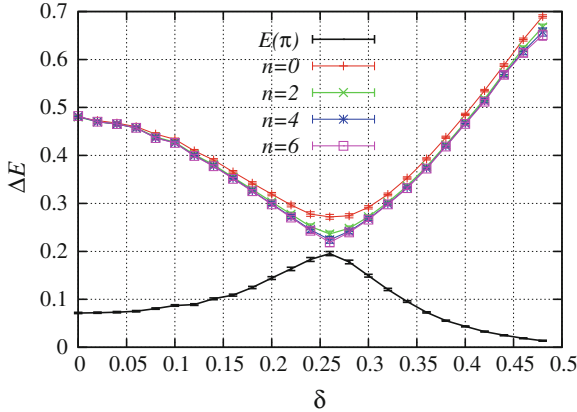
Fig. 4.5 Ground state under the TBC ($E(\pi)$) and the singlet $k = \pi$, $S_T = 1$, $S_T^z = 0$ excited state energy under the TBC ($n = 0, 2, 4, 6$) measured from the ground state energy under the PBC for $L = 12$ and $\beta = 1.5L$. The ground state energy $E(\pi)$ rises up, but the singlet gap dips down at the transition point. The former energy catches the state with the symmetry ($S_T^z = 0$, $P = -1$, $T = -1$) in the Haldane phase, but ($S_T^z = 0$, $P = 1$, $T = 1$) in the dimer phase. On the other hand, the singlet state does the state with the symmetry ($S_T^z = 0$, $P = 1$, $T = 1$) in the Haldane phase, but ($S_T^z = 0$, $P = -1$, $T = -1$)

rapidly. Remarkably, the crossing point does not much depend on the order of the gap estimator. It is because of the special symmetry near this transition point, which is manifested in the invariance of the renormalization group equation [23, 26] under the transformation $y_1 \to -y_1$. We should calculate the higher orders for general cases. Moreover, we can identify the universality class by the level spectroscopy using the several excitation gaps although we do not show here. As we have seen, the level
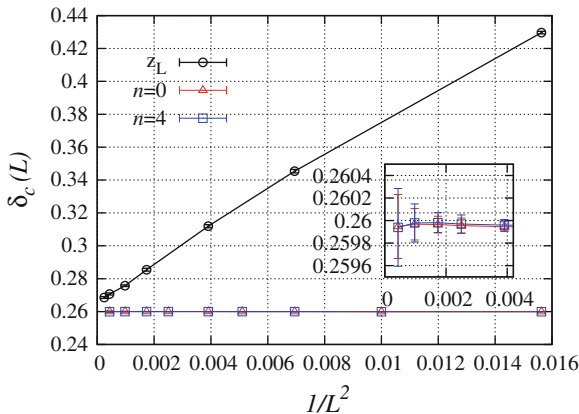
Fig. 4.6 Level crossing point between the two excitations, ($S_T^z = 0$, $P = 1$, $T = 1$) and ($S_T^z = 0$, $P = -1$, $T = -1$) under the TBC together with the crossing point $z_L = 0$, where z_L is the order parameter proposed by Nakamura et al. [32]. The level crossing powerfully detects the transition point even in small systems

crossing or spectroscopy is drastically powerful for systems with strong finite-size effect.

Finally, we mention an application of the meron cluster algorithm [6, 9, 10]. The TBC produces the sign problem since the worldline configuration with an odd winding number has a negative weight. In order to overcome the sign problem, the meron cluster algorithm was invented and applied to a $O(3)$ model with topological term [6] and some fermionic systems [9, 10]. The meron is defined as a cluster that inverts the sign of the weight by flip (the absolute value is not changed). The idea of the meron algorithm is that the sampled state is restricted to only configurations without the merons because configurations with the merons does not contribute to any statistical average. Note that the simulation where the configuration is strictly restricted to the space without any meron suffers slowing down of the sample efficiency; that is the ergodicity is practically broken. Then, actually, the configurations with the merons are allowed, and averages are reweighted by means of the multicanonical method. This intriguing cluster algorithm is also applicable to the quantum spin system under the TBC, as our case in this section. This application of the meron algorithm will perform well in combination with the level spectroscopy.

References

1. Affleck, I. (1985). The quantum Hall effects, σ-models at $\theta = \pi$ and quantum spin chains. *Nuclear Physics B*, *257*, 397–406.
2. Affleck, I., Gepner, D., Schulz, H. J., & Ziman, T. (1989). Critical behaviour of spin-s Heisenberg antiferromagnetic chains: Analytic and numerical results. *Journal of Physics A: Mathe-*

matical and General, 22, 511.

3. Affleck, I., & Haldane, F. D. M. (1987). Critical theory of quantum spin chains. *Physics Review B*, 36, 5291–5300.

4. Arovas, D. P., Auerbach, A., & Haldane, F. D. M. (1988). Extended Heisenberg models of antiferromagnetism: Analogies to the fractional quantum Hall effect. *Physics Review Letters*, 60, 531–534.

5. Barber, M. N. (1983). Finite-size scaling. In C. Domb & J. L. Lebowitz (Eds.), *Phase transitions and critical phenomena* (pp. 146–268). New York: Academic Press.

6. Bietenholz, W., Pochinsky, A., & Wiese, U. J. (1995). Meron-cluster simulation of the θ vacuum in the 2D O(3) model. *Physics Review Letters*, 75, 4524.

7. Cabra, D. C., Honecker, A., & Pujol, P. (1998). Magnetization plateaux in N-leg spin ladders. *Physics Review B*, 58, 6241–6257.

8. Cardy, J. L. (1996). *Scaling and renormalization in statistical physics*. Cambridge: Cambridge University Press.

9. Chandrasekharan, S., Cox, J., Osborn, J., & Wiese, U. J. (2003). Meron-cluster approach to systems of strongly correlated electrons. *Nuclear Physics B*, 673, 405.

10. Chandrasekharan, S., & Wiese, U. J. (1999). Meron-cluster solution of fermion sign problems. *Physics Review Letters*, 83, 3116.

11. des Cloizaux, J., Pearson, J. J. (1962). Spin-wave spectrum of the antiferromagnetic linear chain. *Physics Review*, 128, 2131.

12. Cooper, F., Freedman, B., Preston, D. (1982). Solving $\phi_{1,2}^4$ field theory with Monte Carlo. *Nuclear Physics B*, 210(FS6), 210–228.

13. Delfino, G., & Mussardo, G. (1998). Non-integrable aspects of the multi-frequency sine-Gordon model. *Nuclear Physics B*, 516, 675–703.

14. Edwards, R., Goodman, J., & Sokal, A. (1991). Multi-grid Monte Carlo (ii). two-dimensional XY model. *Nuclear Physics B*, 354, 289–327.

15. Fabrizio, M., Gogolin, A., & Nersesyan, A. (2000). Critical properties of the double-frequency sine-Gordon model with applications. *Nuclear Physics B*, 580, 647–687.

16. Fáth, G., & Sólyom, J. (1993). Isotropic spin-1 chain with twisted boundary condition. *Physics Review B*, 47, 872–881.

17. Gubernatis, J. E., Jarrell, M., Silver, R. N., & Sivia, D. S. (1991). Quantum Monte Carlo simulations and maximum entropy: Dynamics from imaginary-time data. *Physics Review B*, 44, 6011–6029.

18. Gull, E., Werner, P., Parcollet, O., Troyer, M. (2008). Continuous-time auxiliary-field Monte Carlo for quantum impurity models. *Europhysics Letters*, 82, 57003.

19. Haldane, F. D. M. (1982). Spontaneous dimerization in the $S = \frac{1}{2}$ Heisenberg antiferromagnetic chain with competing interactions. *Physics Review B*, 25, 4925.

20. Huscroft, C., Gass, R., & Jarrell, M. (2000). Maximum entropy method of obtaining thermodynamic properties from quantum Monte Carlo simulations. *Physics Review B*, 61, 9300–9306.

21. Inoue, H., & Nomura, K. (1999). Magnetization plateau in the 1D S=1/2 spin chain with alternating next-nearest-neighbour coupling. *Physics Letters A*, 262, 96–102.

22. Kadanoff, L. P. (1980). Singularities near the bifurcation point of the Ashkin-Teller model. *Physics Review B*, 22, 1405–1408.

23. Leo, Kadanoff. (1978). P.: Lattice Coulomb gas representations of two-dimensional problems. *Journal of Physics A: Mathematical and General*, 11, 1399–1417.

24. Kato, Y., & Tanaka, A. (1994). Numerical study of the $S = 1$ antiferromagnetic spin chain with bond alternation. *Journal of the Physical Society of Japan*, 63, 1277–1280.

25. Kitazawa, A. (1997). Twisted boundary conditions of quantum spin chains near the Gaussian fixed points. *Journal of Physics A: Mathematical and General*, 30, L285–291.

26. Kitazawa, A., & Nomura, K. (1997). Critical properties of $S = 1$ bond-alternating XXZ chains and hidden $Z_2 \times Z_2$ symmetry. *Journal of the Physical Society of Japan*, 66, 3944–3956.

27. Kohmoto, M., den Nijs, M., & Kadanoff Leo, P. (1981). Hamiltonian studies of the $d = 2$ Ashkin-Teller model. *Physics Review B*, 24, 5229.

28. Kohno, M., Takahashi, M., & Hagiwara, M. (1998). Low-temperature properties of the spin-1 antiferromagnetic Heisenberg chain with bond alternation. *Physics Review B*, *57*, 1046–1051.
29. Kolb, M. (1985). Symmetry and boundary condition of planar spin systems. *Physics Review B*, *31*, 7494–7496.
30. Kuboki, K., & Fukuyama, H. (1987). Spin-Peierls transition with competing interactions. *Journal of the Physical Society of Japan*, *56*, 3126–3134.
31. Majumdar, C. K., & Ghosh, D. K. (1969). On next-nearest-neighbor interaction in linear chain, Part I. *Journal of Mathematical Physics*, *10*, 1388–1398. doi:10.1063/1.1664978.
32. Nakamura, M., & Todo, S. (2002). Order parameter to characterize valence-bond-solid states in quantum spin chains. *Physics Review Letters*, *89*, 077, 204.
33. Nightingale, M. P. (1976). Scaling theory and finite systems. *Physica A*, *83*, 561.
34. Nomura, K. (1995). Correlation functions of the 2D sine-Gordon model. *Journal of Physics A: Mathematical and General*, *28*, 5451–5468.
35. Nomura, K., & Okamoto, K. (1994). Critical properties of $S = \frac{1}{2}$ antiferromagnetic XXZ chain with next-nearest-neighbour interactions. *Journal of Physics A: Mathematical and General*, *27*, 5773.
36. Nomura, K., & Okamoto, K. (2001). BKT transition and level spectroscopy. *Butsuri*, *56*, 836.
37. Nomura, K., & Okamoto, K. (2002). BKT transition and level spectroscopy. *Proceedings French-Japanese Symposium on Quantum Properties of Low-Dimensional Antiferromagnets* (cond-mat/020172).
38. Okamoto, K., & Nomura, K. (1992). Fluid-dimer critical point in $S = \frac{1}{2}$ antiferromagnetic Heisenberg chain with next nearest neighbor interactions. *Physics Letters A*, *169*, 433.
39. Okamoto, K., & Sugiyama, T. (1988). Ground-state of spin-1/2 alternating Heisenberg-XY ferromagnet in one dimension. *Journal of the Physical Society of Japan*, *57*, 1610–1620.
40. Sandvik, A. W. (1998). Stochastic method for analytic continuation of quantum Monte Carlo data. *Physics Review B*, *57*, 10287–10290.
41. Schulz, H. J. (1986). Phase diagrams and correlation exponents for quantum spin chains of arbitrary spin quantum number. *Physics Review B*, *34*, 6372.
42. Seiler, E., Stamatescu, I., Patrascioiu, A., & Linke, V. (1988). Critical behaviour, scaling and universality in some two-dimensional spin models. *Nuclear Physics B*, *305*, 623–660.
43. Silver, R. N., Sivia, D. S., & Gubernatis, J. E. (1990). Maximum-entropy method for analytic continuation of quantum Monte Carlo data. *Physics Review B*, *41*, 2380–2389.
44. Skilling, J. (1989). Classic maximum entropy. In J. Skilling (Ed.) *Maximum entropy and Bayesian methods* (p. 45). Boston: Kluwer Academic.
45. Todo, S., & Kato, K. (2001). Cluster algorithms for general-S quantum spin systems. *Physics Review Letters*, *87*, 047203.
46. Tonegawa, T., & Harada, I. (1987). Ground-state properties of the one-dimensional isotropic spin-1/2 Heisenberg antiferromagnet with competing interactions. *Journal of the Physical Society of Japan*, *56*, 2153–2167.
47. Totsuka, K., Nishiyama, Y., Hatano, N., & Suzuki, M. (1995). Isotropic spin-1 chains with bond alternation: Analytic and numerical studies. *Journal of Physics: Condensed Matter*, *7*, 4895.
48. Werner, P., Oka, T., & Millis, A. J. (2009). Diagrammatic Monte Carlo simulation of nonequilibrium systems. *Physics Review B*, *79*, 035320.
49. Witten, E. (1984). Non-abelian bosonization in two dimensions. *Communications in Mathematical Physics*, *92*, 455–472.
50. Yamamoto, S. (1994). Ground-state properties of $s = 1$ antiferromagnetic Heisenberg chains with bond alternation. *Journal of the Physical Society of Japan*, *63*, 4327–4330.

Chapter 5
XXZ Spin-Peierls Chain

5.1 Background of Spin-Peierls System

The spin-lattice interaction introduces spin frustration as we mentioned in Chap. 1. As a system dominated by the spin-lattice interaction, a spin-Peierls system has caught the attention for a long time. The low-energy physics is described by the S = 1/2 one-dimensional antiferromagnetic ($\Delta > 0$) *XXZ* or Heisenberg chain model coupled with the lattice degree of freedom in the harmonic potential as

$$H = \sum_r J\left(1 + \sqrt{\frac{\omega\lambda}{2}}\left(a_r + a_r^\dagger\right)\right)(S_{r+1}^x S_r^x + S_{r+1}^y S_r^y + \Delta S_{r+1}^z S_r^z) + \sum_r \omega a_r^\dagger a_r.$$

(5.1)

Here we use the dispersionless (Einstein) phonon in this chapter. The validity for the real materials, such as $CuGeO_3$ [2, 25, 28, 46, 50, 53], is discussed in Refs. [21, 62]. When the decrease in energy by dimerization, forming spin singlet pairs, exceeds the increase by lattice distortion, the spin-Peierls system turns into the dimer phase, which is called the spin-Peierls transition. This formation of the singlet pairs, certainly, results from the quantum nature of the spin degree of freedom; that is, such a dimer order cannot take place for classical spin models. The investigation of this nontrivial system consisting of the multiple degree of freedom will give us an important understanding of frustrated quantum spin systems.

In the spin-Peierls system, the quantum effect of the lattice degree of freedom is controversial. The hybridization of the two degrees of freedom depends on the difference of the energy scales. The adiabatic limit corresponds to the case where the phonon energy scale is much lower than the spin energy scale (actually formed spin-gap scale) and the quantum nature of the lattice degree of freedom can be ignored [16]. In this limit, the lattice degree of freedom is nothing but a classical parameter in the model, and the phase diagram is the same with the $S = 1/2$ alternating-bond spin model (4.41), where there is no spin frustration. This spin model can be mapped to the sine-Gordon model, and the spin-lattice coupling, which is relevant in the theory, instantaneously drives the ground state into the dimer phase. This result is totally

consistent with the Cross-Fisher theory [16]. On the other hand, the antiadiabaticity produces the effective spin frustration, which is manifest after tracing out the phonon degree of freedom. The role of quantum nature of lattice has been investigated by many theoretical approaches: the perturbation expansion [30], the linked cluster expansion [52], the Lanczos diagonalization method [3, 4, 8, 61], the flow equation method [44, 45, 54], the unitary transformation [59, 60, 64], and the density matrix renormalization group (DMRG) [9, 14, 27, 41, 59]. In the antiadiabatic limit, a simple effective model is the J_1-J_2 model [30] whose phase diagram was explained in Sect. 4.2 by mapping to the sine-Goldon model. The main role of the next-nearest interaction is to reduce the marginal term in the field theory. Then, the Kosterlitz-Thouless (KT) [29] transition from the Tomonaga-Luttinger (TL) liquid phase to the dimer phase occurs [19] when the marginal term becomes zero.

Here, let us write down the parameter in the effective spin Hamiltonian in the antiadiabatic limit in according to Ref. [18, 60] using the Schrieffer-Wolff transformation. The ratio $\alpha = J_2/J_1$ of the effective J_1-J_2 model after tracing out the phonon degree of freedom in the spin-Peierls model (5.1) for $\Delta = 1$ becomes

$$\alpha_{\text{eff}} \simeq \frac{\lambda/4\omega + 3\lambda^2/64\omega - 37\lambda^2/384\omega^2}{1 + \lambda/4 - \lambda/4\omega - 3\lambda^2/32\omega + 28\lambda^2/384\omega^2}, \tag{5.2}$$

up to the second order of λ and $1/\omega$.

We investigate the phase diagram and transition in the crossover region between the two limits in this chapter. For the intermediate region, the self-consistent harmonic approximation [15, 17, 36] and the renormalization group (RG) method [5, 13, 15, 19, 51] have been applied to an effective action derived by tracing out the phonon degree of freedom. Particularly, Sun et al. [51] solved numerically the RG equations of an effective bosonized action and obtained the phase diagram of the *XXZ* spin-Peierls model over the whole adiabaticity. About this analysis, however, Citro et al. [15] expected that the result was not correct because an invalid scaling [57] was used. The phase diagram needs to be investigated by a more reliable approach. Also experimentally, some realistic materials have been found where the ratio of the spin and phonon energy scales is away from the two limits, such as $CuGeO_3$ and $MEM(TCNQ)_2$ [26, 55, 56]; the mechanism of the phase transitions are still contentious [22, 42, 43]. Accurate calculation for the intermediate region, however, has been difficult because of the complexity of the system. The conventional quantum Monte Carlo (QMC) methods [31, 34, 35, 40, 45, 48] cannot calculate it efficiently as we explained in Chap. 3. For overcoming the difficulty, we have developed the QMC method for nonconserved particles, extending the worm (directed-loop) algorithm. We have successfully eliminated the cumbersome bounce (rejection) process of the bosonic worm scattering that has been a bottle neck in the method. Moreover, we have, now, the level spectroscopy that will powerfully extract the transition point and critical phenomena of the KT transition. Making the most of these novel methods, we unambiguously elucidate the critical phenomena of the *XXZ* spin-Peierls chain, which has been discussed for a long time, in the following sections.

5.2 Isotropic Case

5.2.1 Conventional Analyses

The phase boundary for the isotropic case $\Delta = 1$ has been investigated by the several methods [41, 44, 45, 59, 60]. As analytical calculation, an effective spin model is derived by using the flow equation [54] or the unitary transformation [60] and the boundary is determined as the point where the ratio $\alpha = J_2/J_1$ becomes 0.2411 [38]. Numerically, the vanishing of the spin gap [14] or the level crossing of the excitations [41, 59] is investigated by the density matrix renormalization group method.

By the QMC method, however, it has been difficult to determine the transition point accurately. For the isotropic point, the phase transition is expected to be the KT type [13]. The Binder ratios [6, 7] for different sizes, which intersect at the critical point, just merges over the KT transition since the TL liquid phase is everywhere critical. Figure 5.1 shows the spin stiffness and the Binder ratio of the staggered operator $m = \sum_r (-1)^r S^z_{r+1} S^z_r$ w.r.t. the spin-phonon coupling. The stiffness is defined as

$$\rho_s = \frac{1}{L} \frac{\partial^2 F(\phi)}{\partial \phi^2}, \tag{5.3}$$

which is the spin-rotation susceptibility of the free energy (the ground state energy at $T = 0$). This quantity can be measured as the winding-number fluctuation in the QMC method [23, 24]. The Binder ratio is defined as the moment ratio

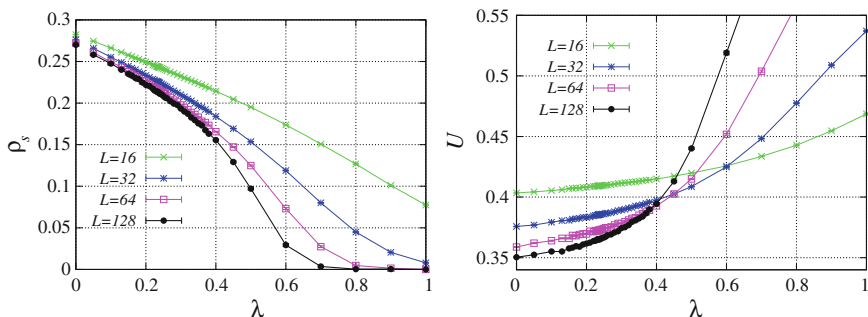$$U = \frac{\langle m^2 \rangle^2}{\langle m^4 \rangle}, \tag{5.4}$$

Fig. 5.1 Spin stiffness (*left*) and the Binder ratio (*right*) w.r.t. the spin-phonon coupling λ for $\Delta = 1$, $\omega = 1/4$, $\beta = 2L$. It is extremely difficult to find the transition point from these data

which becomes 1/3 for a disordered phase and 1 for a fully ordered phase in the thermodynamic limit. This staggered operator functions as the dimer order parameter.

About our simulations, we set $J = 1$ through this thesis. Here, we use the energy unit as

$$J_{\text{eff}} = J \left(1 + \alpha \langle q \rangle\right)$$
$$= J \left(1 + \sqrt{\frac{\omega\lambda}{2}} (\langle a + a^{\dagger} \rangle)\right) \tag{5.5}$$

for the stiffness. Quantities are sampled typically during more than 10^6 Monte Carlo steps after 10^5 thermalization steps (burn-in period). We run more than 10 or 60 simulations independently for each parameter. The error is estimated by the binning analysis [32] using much larger bin sizes than actual correlation time. The bare phonon excitation gap is set $\omega = 1/4$ here for the comparison with the previous calculation [48].

In general, it is extremely difficult to find the merge point of the Binder ratio. A moderately better way to detect the KT transition point by the Monte Carlo method [20, 23, 24, 39, 58] is to observe the universal jump of the spin stiffness [37, 49]. Although the dumping is seen in the figure, it is necessary to simulate very large systems to confirm the discontinuous jump at the critical point. As we have seen, the usual Monte Carlo analysis cannot catch the KT transition point of the spin-Peierls model.

For the isotropic case, Sandvik et al. [48] determined the boundary by the QMC method as the special point where the staggered spin susceptibility grows in proportion to the system size, which is defined as

$$\chi_{s^z} = \frac{1}{L} \sum_{i,j} (-1)^{i-j} \int_0^{\beta} d\tau \langle S_i^z(\tau) S_j^z \rangle. \tag{5.6}$$

This behavior comes from the absence of the marginal operator after mapping to the sine-Gordon model (4.2); in the TL liquid phase except the critical point, the marginal operator gives the logarithmic correction to the correlation functions [11]. We plot the spin susceptibility (5.6) and the dimer susceptibility,

$$\chi_{sd} = \frac{1}{L} \sum_{i,j} (-1)^{i-j} \int_0^{\beta} d\tau \left\langle (S_i \cdot S_{i+1})(\tau)(S_j \cdot S_{j+1}) \right\rangle, \tag{5.7}$$

for several sizes w.r.t. the spin-phonon coupling in Fig. 5.2. There seems, as expected, a crossing point of the both quantities detecting the vanishment of the logarithmic correction. Although this analysis is effective, it is still difficult to determine the precise boundary because the intersection is slightly shifting as the system size increase.
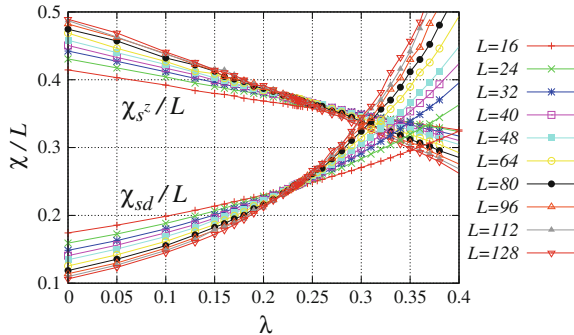
Fig. 5.2 Spin (staggered) susceptibility (5.6) and the dimer susceptibility (5.7) w.r.t. the spin-phonon coupling for $\omega = 1/4$, $\beta = 2L$. The both quantities are expected to intersect at the transition point because of the absence of the marginal term, but the crossing point is slightly shifting as the system size increases. We can estimate the point as $\lambda_c \sim 0.23$, which is consistent with the previous calculation [48] as $0.1764 < \lambda_c < 0.2304$

5.2.2 Precise Phase Boundary by Level Spectroscopy

We determine the precise phase boundary for the isotropic case by observing the level crossing calculated by the QMC technique. As Okamoto and Nomura [38] introduced for the first time, we calculate the energy gaps of the $S = 1$ triplet state and $S = 0$ singlet state with wavenumber $k = \pi$. In the QMC method, the triplet gap is easily accessible. The correlation functions (4.12) and (4.16) with $\hat{O} = S_\pi^z \propto \sum_r S_r^z e^{ikr}\big|_{k=\pi}$ can be calculated by simple measurements of the current worldline configuration because it is a diagonal operator. The singlet state is ruled out by this operation; that is,

$$\langle S = 0|S_k^z|gs \rangle = 0, \tag{5.8}$$

where the ground state and a $S = 0$ singlet state are expressed as $|gs\rangle$ and $|S = 0\rangle$, respectively. For the singlet excitation, on the other hand, it is not trivial what operator we should use. In our spin-Peierls model, we can elicit the $S = 0$ singlet excitation by using several operators, such as, $(S \cdot S)_k$, $(qS \cdot S)_k$, n_k, q_k, and so on. It should be pointed out that the systematic error and the convergence of the gap estimators strongly depend on the used operator although the same gap and state are taken. It is because the spectral weight, which is expressed as b_ℓ after Eq. (4.21), is different according to the operator. Figure 5.3 shows the singlet-gap estimator ($n = 2$), which was defined as Eq. (4.26) in Sect. 4.3, w.r.t. temperature for different parameters. It is seen that the convergence rate for $T \to 0$ of the estimators strongly depends on the operator and parameter. Thus, we choose practically the lowest gap, comparing the several gap estimators below.

About the detail calculations, we calculate the correlation function at the Matsubara frequencies ($\omega_j = 2\pi j/\beta$) of $(S \cdot S)_k$ and $(qS \cdot S)_k$ by integrating the
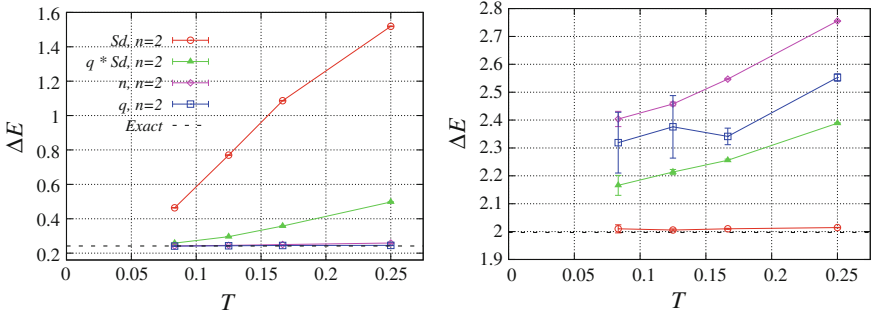
Fig. 5.3 Singlet-gap estimators ($n = 2$) by the several operators w.r.t. temperature for $L = 4$, $\lambda = 1/2$, $D = 4$, $\omega = 1/4$ (*left*) and $\omega = 4$ (*right*). The boson-occupation number in the simulations is restricted less than the cutoff D. For small ω, the first excited state has the bosonic origin. For large value, on the other hand, it has the spin origin. Thus, the actual convergence rate for $T \to 0$ strongly differ. The exact values calculated by the diagonalization are shown together
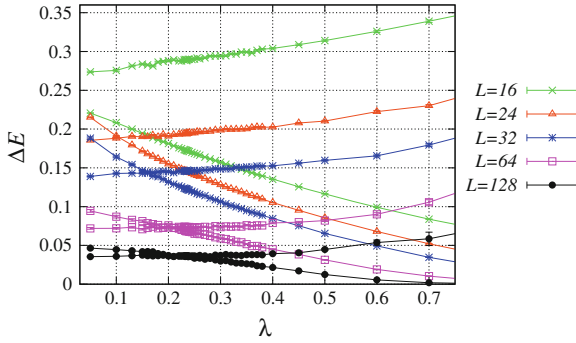
Fig. 5.4 Triplet and singlet gaps ($n = 2$) of the several system sizes w.r.t. the spin-phonon coupling for $\omega = 1/4$, $\beta = 2L$. The two gaps intersect at a spin-phonon coupling depending on the system size

phase factor ($e^{i\tau\omega_j}$) of the operator at imaginary time τ on the worldlines; they are one of the operators of the Hamiltonian. The diagonal operator n_k is measured by the same way as S_k^z. The off-diagonal operator q_k is measured by the bosonic worm; when the worm head moves on the worldlines from τ_1 to τ_2, it gets the integrated phase $\int_{\tau_1}^{\tau_2} d\tau e^{i\tau\omega_j}$. Then, we reweight it by the same way with other off-diagonal measurements explained in Sect. 3.4.4.1.

The calculated triplet and singlet gaps are shown in Fig. 5.4 for $\omega = 1/4$, $\beta = 2L$. The first excited state is changed from the triplet to the singlet, and the two gaps intersect at a spin-phonon coupling depending on the system size. Then, the crossing point int the thermodynamic limit is precisely extrapolated from the finite-size data as shown in Fig. 5.5. The finite-size correction term is derived from the irrelevant operators [10–12, 47] and the dominant correction is from the operators of critical dimension $x = 4$.
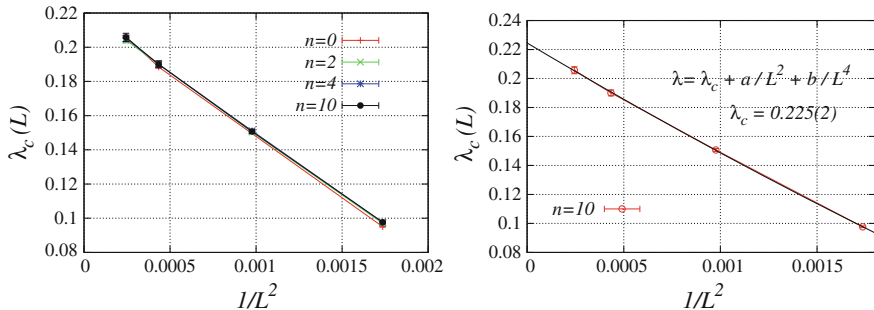
Fig. 5.5 Extrapolation of the level-crossing point of the gap estimators for each order *n* (*left*) and the fitting to the quadratic function for $n = 10$ (*right*). It is seen that there is a strong finite-size effect on the crossing point, but the finite-size data are well scaled as the form derived from the dimension analysis of the irrelevant operators. On the *left panel*, the level crossing points between the same order estimators for the triplet and the dimer excitations are shown

We check the correctness of the estimated transition point by calculating the critical dimensions of the operators and identifying the universality class. From the conformal field theory [10], the critical dimension is related, for the periodic boundary condition (PBC), to the excitation gap as

$$(\Delta E)_\ell(L) = \frac{2\pi v x_\ell}{L}, \tag{5.9}$$

where v is the spin velocity. We call the excitation of $S = S^z = 0$ as the dimer excitation, $S = 1, S^z = 0$ as the Néel excitation, and $S = 1, S^z = \pm 1$ as the doublet excitation below. For the isotropic case, now, the Néel and the doublet excitation form the triplet excitation. First, we calculate the velocity from the triplet excitation of the smallest wavenumber:

$$v(L) = \frac{L}{2\pi} \Delta E_{k=\frac{2\pi}{L}} = v + O(L^{-2}). \tag{5.10}$$

Figure 5.6 shows the calculated velocities for each system size and the extrapolation for $L \to \infty$. We set the spin-phonon coupling as $\lambda = 0.225$. The all (except $n = 0$) order estimators seem to converge to the same value, which is expected from the excitation spectrum in the liquid phase; there is no continuum excitation just above the lowest excitation of the smallest wavenumber in the bulk limit. Thus, the systematic correction of the gap estimator vanishes in the limit.

Then, we define a quantity corresponding to the critical dimension as

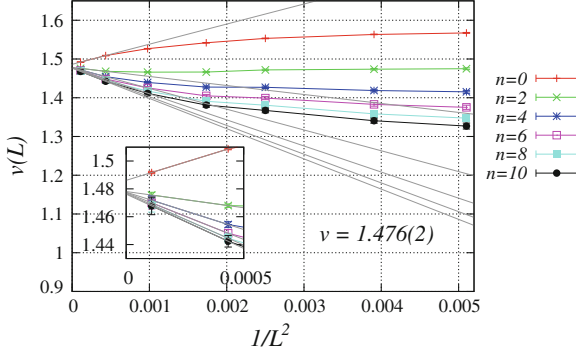$$x_\ell = \frac{L}{2\pi v} (\Delta E)_\ell \tag{5.11}$$

Fig. 5.6 Spin velocity estimation by the extrapolation from the triplet energy gaps of the smallest wavenumber $k = 2\pi/L$. We set the parameters as $\lambda = 0.225$, $\beta = 1.5L$. The linear fitting lines using the two largest size data are shown together
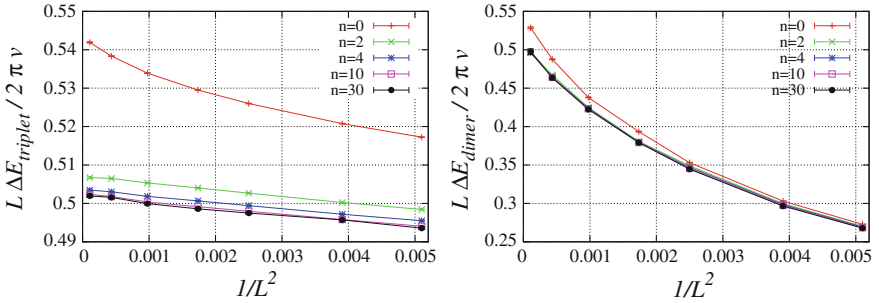

Fig. 5.7 Critical dimensions of the triplet and singlet excitation. They converges to a value close to 1/2 in the thermodynamic limit, which is consistent with the $k = 1$ $SU(2)$ WZW model. Remarkably, the conventional second moment ($n = 0$) fails to get the correct value

using the lowest excitations $(\Delta E)_\ell$ with $k = \pi$. Figure 5.7 shows the calculated critical dimensions of the triplet and singlet excitations, where the dimension is well estimated from the higher order estimators for each system size. The both seem to converge to a value close to 1/2 derived from the $k = 1$ $SU(2)$ Wess-Zumino-Witten (WZW) [1, 63] model. This is expected from the analogy with the J_1-J_2 model. Let us check also the central charge from the finite-size correction of the ground state energy [1, 11, 33] as

$$E_0(L) = E_0 - \frac{\pi v}{6L^2}\left(c + \frac{b}{(\ln L)^3}\right) + \text{higher order.} \qquad (5.12)$$

The estimated value is shown in Fig. 5.8, calculated from the two fitting. We estimate the central charge as $c = 1.01(2)$, which is consistent with the free-boson (sine-Gordon) field theory ($c = 1$).
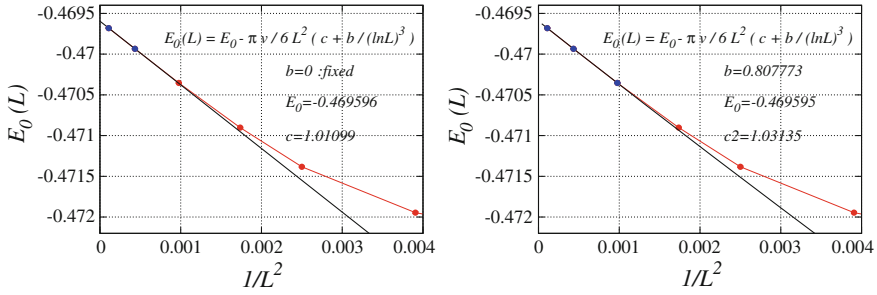
Fig. 5.8 Central charge estimation from the ground state energy expressed as Eq. (5.12). On the *left panel*, the two largest-size data (*blue dots*) are used for the fitting. In the *right*, on the other hand, the three largest-size data (*blue dots*) are used by taking the logarithmic correction term into account. We estimate the central charge as $c = 1.01(2)$, which is consistent with $c = 1$ of the free-boson (sine-Gordon) field theory

The critical dimensions and the central charge are both totally consistent with the $k = 1$ $SU(2)$ WZW model. Therefore, we confirm the the power of our level spectroscopy analysis by the QMC method and accuracy of the transition point, which we estimate here as $\lambda_c = 0.225(2)$. This value is much more precise than the previous calculation [48] as $0.1764 < \lambda_c < 0.2304$ in our model. In the meantime, if we apply the unitary (Schrieffer-Wolff) transformation [60] from the spin-Peierls model to the effective spin model, the obtained transition point here corresponds to $J_2/J_1 \sim 0.18$ from Eq. (5.2); it is smaller than 0.2411 in about 25 %. The level spectroscopy analysis can quantitatively treat the spin-Peierls model beyond the simple effective spin model.

5.3 Liquid-Dimer Transition

Next, we consider the *XY* anisotropic case $0 < \Delta < 1$. In this parameter region, also, it is expected that the KT transition occurs from the TL liquid phase to the dimer phase as the spin-phonon coupling is strengthened. At the critical point, the logarithmic correction appears in contrast to the isotropic case. Figure 5.9 shows the spin stiffness and the susceptibilities for $\Delta = 3/4, \omega = 1/4$. In the right figure, the doublet susceptibility defined as

$$\chi_{s^+} = \frac{1}{L}\sum_{i,j}(-1)^{i-j}\int_0^\beta d\tau \langle S_i^+(\tau)S_j^-\rangle. \tag{5.13}$$

is shown together with the dimer susceptibility (5.7). This quantity is measured by the spin worm; the integrated phase factor is summed when the worm head moves on
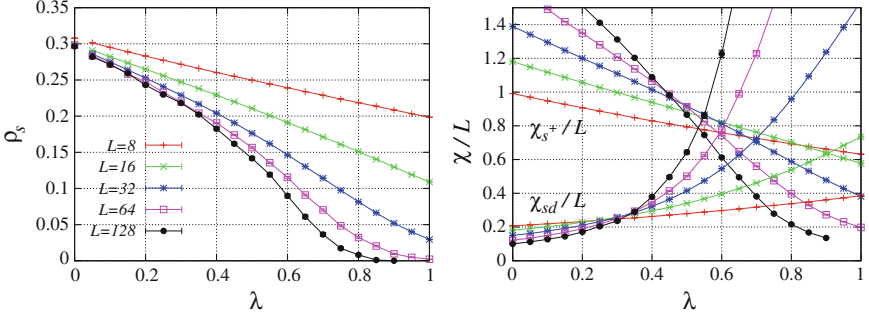
Fig. 5.9 Spin stiffness (*left*) and the doublet/dimer staggered susceptibility (*right*) w.r.t. the spin-phonon coupling for $\Delta = 3/4, \omega = 1/4, \beta = 1.5L$. The stiffness data implies the KT transition, but it is difficult to elicit the transition point. In contrast to the isotropic case, there is a logarithmic correction at the transition point which we see as the intersection shift in the susceptibility data
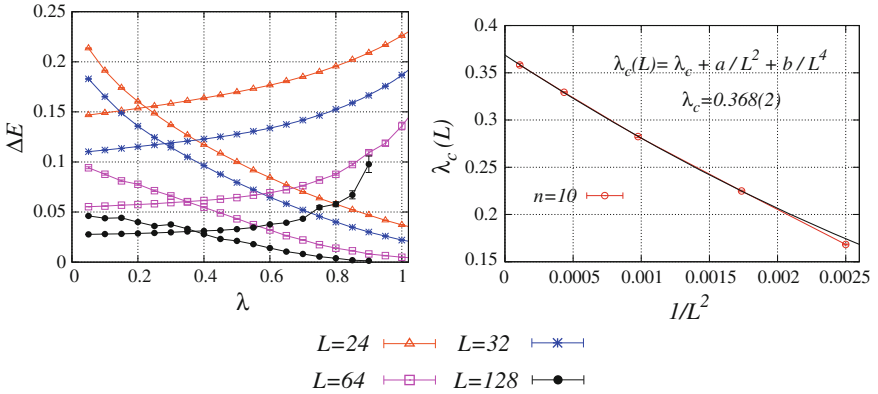

Fig. 5.10 Level crossing between the doublet and dimer excitations against the spin-phonon interaction axis (*left*) and the extrapolation of the crossing point (*right*)

the worldlines. Note that we have to add another phase π that is related to the gauge rotation on the z-axis; the sign of the wave function is actually changed for the QMC simulation. Thus we reweight the sign to get the original correlation functions.

It is almost no way to analyze this phase transition for the easy-plane parameter region by the conventional method. Utilizing the level spectroscopy, we can correctly investigate also this case. Figure 5.10 shows the level crossing between the doublet and dimer excitations together with the extrapolation. As the isotropic case, we can extrapolate a transition point in the thermodynamic limit.

The calculated spin velocity is shown in Fig. 5.11 when we set the spin-phonon coupling $\lambda = 0.364$ (later 0.368). The velocity is estimated from the Néel excitation with the smallest wavenumber, which is statistically better than the doublet excitation. Note that the lowest dispersion curve of the doublet and Néel excitation will be the
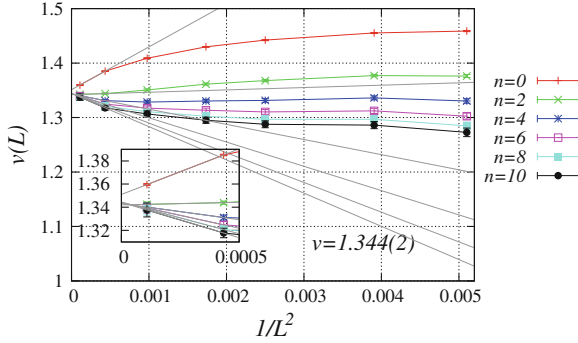
Fig. 5.11 Spin velocity estimation from the finite-size data of the Néel excitation when we set the spin-phonon coupling as $\lambda = 0.364$, $\beta = 1.5L$
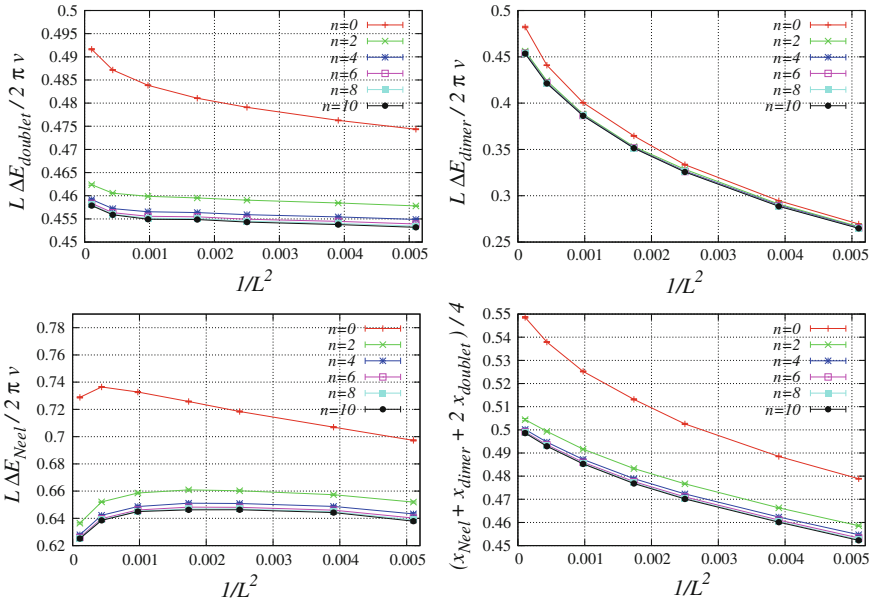

Fig. 5.12 Critical dimensions of the doublet (*upper left panel*), the dimer (*upper right panel*), and the Néel (*lower left panel*) excitation together with the combined quantity (*lower right panel*). There seem some logarithmic correction in each excitation, e.g., the rapid decrease of the Néel critical dimension in the large-size data. For the combined quantity, however, it seems to converge to 1/2 in proportion to $1/L^2$ without logarithmic correction. Note that the second moment ($n = 0$) has so large systematic error that the extrapolated value is not correct

same as the simple *XXZ* spin model. Then, the critical dimensions of the doublet, the dimer and the Néel excitation are shown in Fig. 5.12 together with a combined quantity defined as $(x_{neel} + x_{dimer} + 2x_{doublet})/4$. If the critical point belongs to the $k = 1$ $SU(2)$ WZW model, the each critical dimension will behave as mentioned in
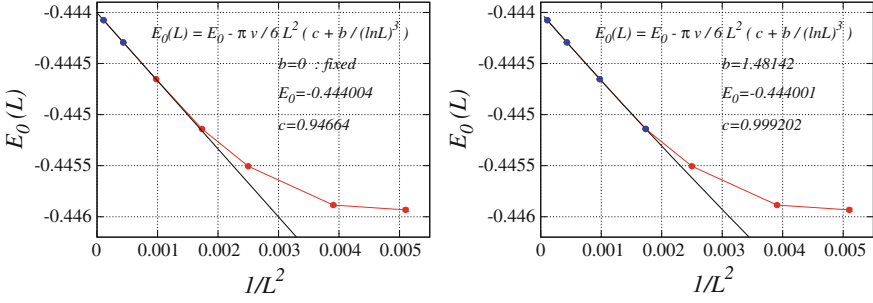
Fig. 5.13 Central charge estimation for $\Delta = 3/4, \omega = 1/4, \lambda = 0.364, \beta = 1.5L$. On the *left panel*, the two largest-size data (*blue dots*) are used with $b = 0$ in the expression. On the *right panel*, the four largest-size data (*blue dots*) are used. We estimate the charge as $c = 0.95(5)$, which is consistent with the $SU(2)$ WZW model

Fig. 5.14 Combined critical dimension for $\lambda = 0.368$. It seems to converge to a slightly larger value than 1/2. From such a check, we estimate the error of the transition point as $\lambda_c = 0.365(3)$
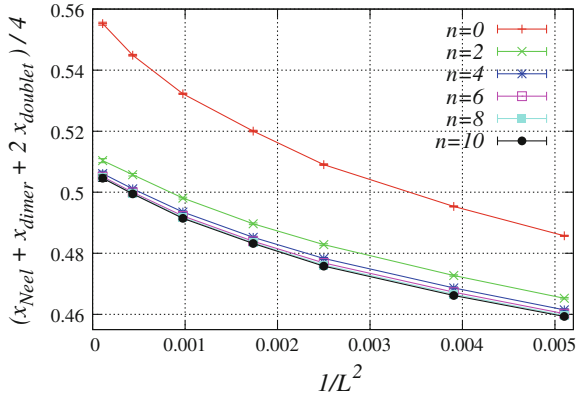
Ref. [1]

$$x_{doublet} = x_{dimer} = \frac{1}{2} - \frac{1}{4 \ln L} \tag{5.14}$$

$$x_{neel} = \frac{1}{2} + \frac{3}{4 \ln L}. \tag{5.15}$$

Thus the logarithmic correction is eliminated in the combined dimension. In the figure, although the each dimension seems to have some logarithmic correction (rapid variation in the large-size data), the combined quantity smoothly converges to 0.5 without logarithmic correction.

We check also the central charge as in Fig. 5.13. The charge is estimated as $c = 0.95(5)$. From the above calculations, we conclude this phase transition is the $k = 1$ $SU(2)$ WZW type. The emergent $SU(2)$ symmetry appears here, which the original Hamiltonian does not hold. This is the same scenario with the J_1-J_2 and sine-Gordon model.

Let us also check the accuracy of our analysis. Figure 5.14 shows the combined dimension in the case where we set the spin-phonon coupling as $\lambda = 0.368$. The combined quantity seems to converge to a slightly larger value than 1/2. From such a check, we estimate the critical point as $\lambda_c = 0.365(3)$.

5.4 Néel-Dimer Transition

Next we investigate the Ising-anisotropy ($\Delta > 1$) case. Figure 5.15 shows the Binder ratio of the Néel and dimer excitation for $\Delta = 3/2$. It is seen that there is a transition point where the ratios become invariant of the system size. Although this transition does not seem the KT type, it is still difficult to determine the precise transition point.

We observe the level crossing of the Néel and dimer excitation. The extrapolation of the crossing point is shown in Fig. 5.16, where the finite-size data are scaled well.
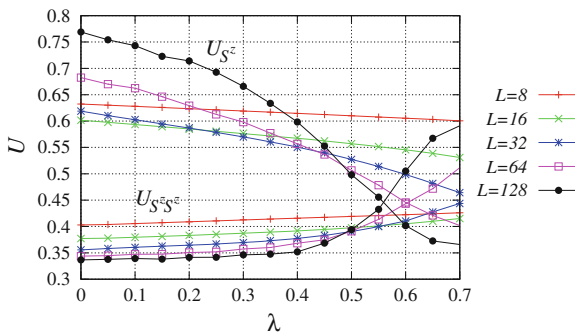

Fig. 5.15 Binder ratio of $S_{k=\pi}^z$ and $(S^z S^z)_{k=\pi}$ for $\Delta = 3/2, \omega = 1/4, \beta = 1.5L$. The both seem to become invariant around $\lambda = 0.5$, but it is difficult to determine the precise transition point
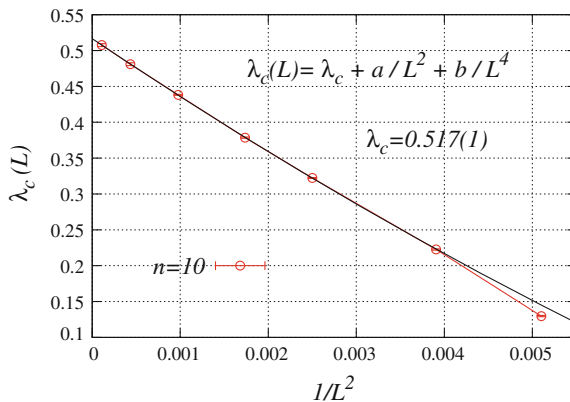

Fig. 5.16 Extrapolation of the level crossing point between the Néel and dimer excitation for $\Delta = 3/2, \omega = 1/4, \beta = 1.5L$. The higher order estimator $\hat{\xi}^{(10)}$ (4.31) is used
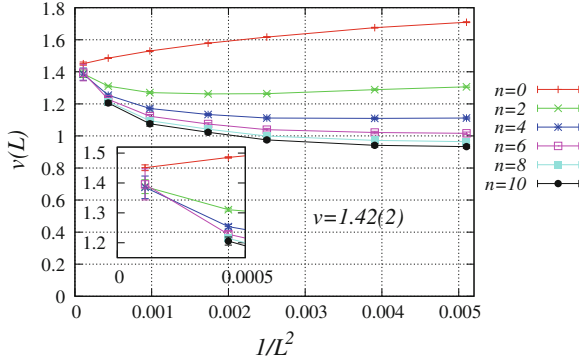
Fig. 5.17 Estimation of the spin velocity by the extrapolation from the finite-size data
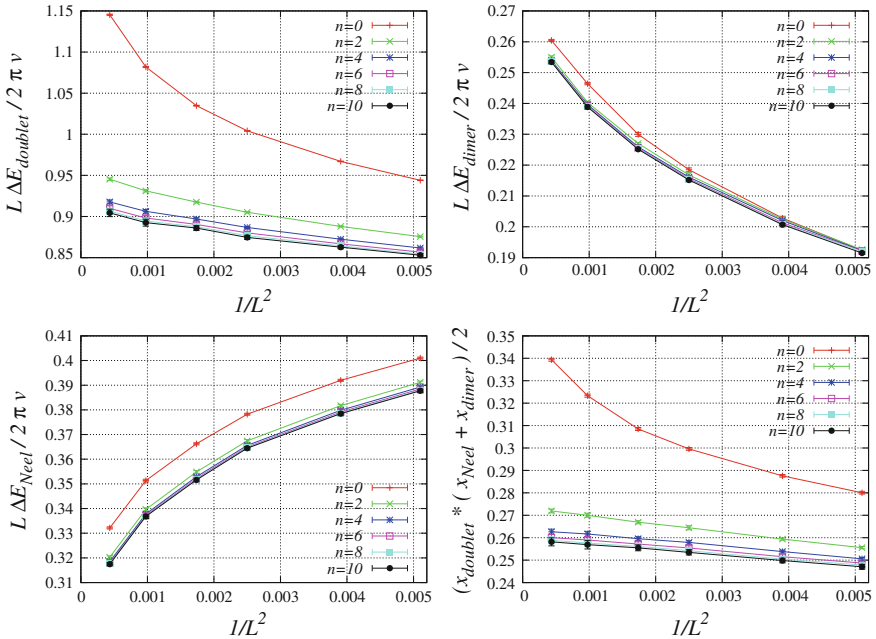

Fig. 5.18 Critical dimensions for $\Delta = 3/2$, $\omega = 1/4$, $\lambda = 0.517$, $\beta = 1.5L$. The dimensions of the dimer and Néel become the same value in $L \to \infty$ at the transition point in this Ising anisotropic case. The convergence to a value close to 1/4, about the combined dimension, implies that this transition is the Gaussian universality class

Assuming the transition point as $\lambda_c = 0.517$, let us check the universality class. First, we estimate the spin velocity by the extrapolation as shown in Fig. 5.17. Then, we calculate the critical dimensions, using the estimated velocity. If this transition point is the Gaussian universality (free boson) class, the critical dimensions become
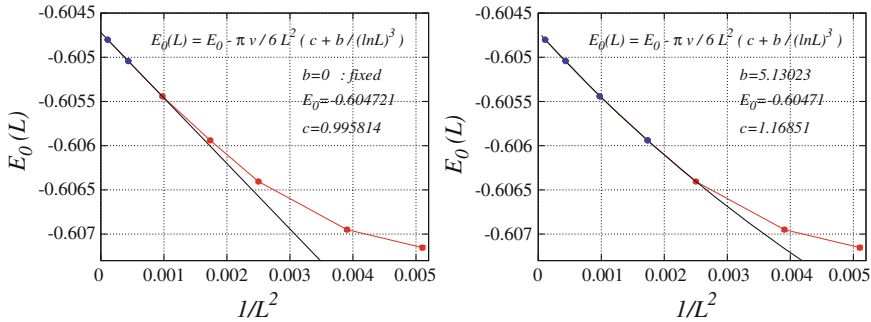
Fig. 5.19 Estimation of the central charge for $\Delta = 3/2, \omega = 1/4, \lambda = 0.517$. The two largest data (*blue dots*) are used on the *left panel* with $b = 0$, and the four largest data (*blue dots*) are used on the *right panel* taking the logarithmic-correction term into account. We can estimate the value $c \sim 1.0$, which is consistent with the free-boson field theory
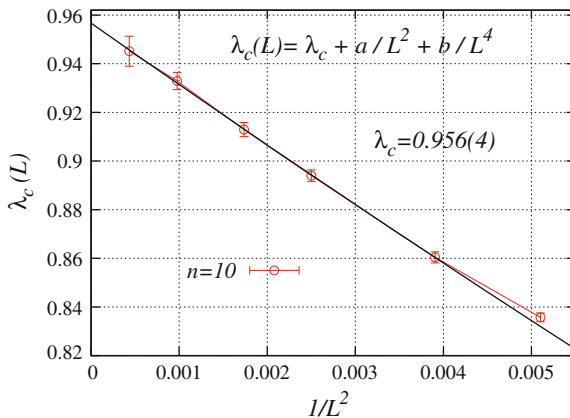

Fig. 5.20 Extrapolation of the level crossing point between the Néel and dimer excitation for $\Delta = 1.1, \omega = 1, \beta = 1.5L$. The higher order estimator $\hat{\xi}^{(10)}$ (4.31) is used

$$x_{doublet} \, x_{neel} = 1/4 \tag{5.16}$$

$$x_{neel} = x_{dimer}. \tag{5.17}$$

In the first equation, the Luttinger parameter is canceled. Then, we check the convergence of a combined dimension $x_{double} \, (x_{neel} + x_{dimer})$. The right bottom panel in Fig. 5.18 shows it converges to a value close to 1/4 as expected.

We check also the central charge. Figure 5.19 shows the charge is estimated as $c \sim 1.0$, as expected. Thus, we conclude this phase transition is the Gaussian universality class and the transition point is $\lambda_c = 0.517(2)$.

In the meanwhile, Sun et al. [51] obtained the phase diagram of the *XXZ* spin-Peierls model by numerically solving the renormalization group equation for an effective model. The most interesting point of their conclusion is that the two phase
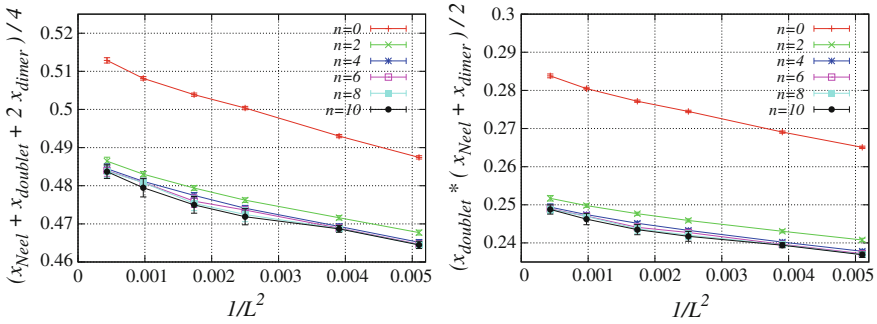
Fig. 5.21 Combined critical dimensions for $\Delta = 1.1, \omega = 1, \lambda = 0.956, \beta = 1.5L$. The *left panel* shows this
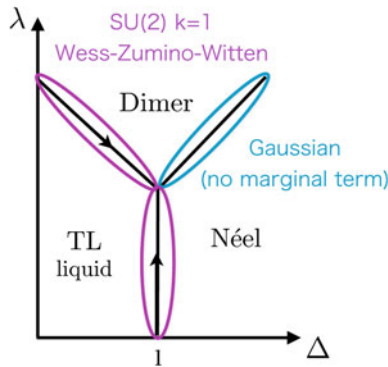

Fig. 5.22 Phase diagram of the *XXZ* spin-Peierls model. The arrow indicates the flow of the renormalization. The Gaussian line is a set of fixed points, and the critical exponents (dimensions) continuously varies on the line. Compare it with the phase diagrams of the J_1-J_2 model in the antiadiabatic limit (Fig. 4.1) and the alternating-bond model in the adiabatic limit (Fig. 4.3)

transitions occur as the spin-phonon interaction increases for small Ising anisotropy: the Néel phase, the TL liquid phase, and the dimer phase. In other words, the liquid phase runs off the edge of the Heisenberg point $\Delta = 1$. Then, we set parameters as $\Delta = 1.1, \omega = 1$, and the apply the same analysis with the case of $\Delta = 3/2$. We confirm the doublet-excitation gap is always larger than the Néel excitation gap, which is corresponding to the Luttinger parameter $K < 1$ in Eq. (4.2). The level crossing point of the Néel and the dimer excitation is well extrapolated as shown in Fig. 5.20. We check the combined critical dimensions that catch the SU(2) WZW model or the Gaussian universality as in Fig. 5.21. Although the comparison of the values is tricky, we can see the extrapolated value is not 1/2 on the left panel, but very close to 1/4 on the right panel. Therefore, we conclude this transition is not the WZW model but the Gaussian universality class. We expect the liquid phase ends at the isotropic line $\Delta = 1$.

Finally, we discuss the crossover between the two limits. As we show the universality classes by the level spectroscopy, we expect the phase diagram of the *XXZ* spin-Peierls model as Fig. 5.22. Although we have investigated mainly the relatively adiabatic region $\omega = 1/4$, we expect this phase diagram is qualitatively valid for any adiabaticity of the phonon. Since this phase diagram is totally consistent with the J_1-J_2 model as shown in Fig. 4.1, which is an effective model in the antiadiabatic limit, it will be continuously connected to the adiabatic limit, where the phase boundary is $\lambda_c \to 0$ for $\Delta \leq 1$. The Gaussian universality line for $\Delta > 1$ remains in the adiabatic limit, and it becomes the Ising universality class if we consider the static alternation as discussed in Sect. 4.4 and shown in Fig. 4.3. Now let us remind that we have calculated the spin-Peierls model without the negative sign, and we obtain the phase diagram consistent with the frustrated spin model. Thus, we can correctly investigate the critical phenomena of the frustrated quantum spin system without any approximation. In other words, we are successful in avoiding the cumbersome negative sign by introducing the quantum phonon. This fact encourages us to apply our method to more complex systems. We will investigate multi-chain and two-dimensional spin-Peierls systems in Chap. 6.

References

1. Affleck, I., Gepner, D., Schulz, H. J., & Ziman, T. (1989). Critical behaviour of spin-s Heisenberg antiferromagnetic chains: Analytic and numerical results. *Journal of Physics A: Mathematical and General*, *22*, 511.
2. Arai, M., Fujita, M., Motokawa, M., Akimitsu, J., & Bennington, S. M. (1996). Quantum spin excitations in the spin-Peierls system CuGeO$_3$. *Physical Review Letters*, *77*, 3649.
3. Augier, D., & Poilblanc, D. (1998). Dynamical properties of low-dimensional CuGeO$_3$ and NaV$_2$O$_5$ spin-Peierls systems. *European Physical Journal B: Condensed Matter Physics*, *1*, 19–28.
4. Augier, D., Poilblanc, D., Sørensen, E., & Affleck, I. (1998). Dynamical effects of phonons on soliton binding in spin-Peierls systems. *Physical Review B*, *58*, 9110–9113.
5. Bakrim, H., & Bourbonnais, C. (2007). Quantum vs classical aspects of one dimensional electron-phonon systems revisited by the renormalization group method. *Physical Review B*, *76*, 195115.
6. Binder, K. (1981). Critical properties from Monte Carlo coarse graining and renormalization. *Physical Review Letters*, *47*, 693–696.
7. Binder, K., & Landau, D. P. (1984). Finite-size scaling at first-order phase transitions. *Physical Review B*, *30*, 1477–1485.
8. Büchner, B., Fehske, H., Kampf, A. P., & Wellein, G. (1999). Lattice dimerization in the spinPeierls compound CuGeO$_3$. *Physica B: Condensed Matter*, *259–261*, 956.
9. Bursill, R. J., McKenzie, R. H., & Hamer, C. J. (1999). Phase diagram of a Heisenberg spin-Peierls model with quantum phonons. *Physical Review Letters*, *83*, 408.
10. Cardy, J. L. (1984). Conformal invariance and universality in finite-size scaling. *Journal of Physics A: Mathematical and General*, *17*, L385.
11. Cardy, J. L. (1986). Logarithmic corrections to finite-size scaling in strips. *Journal of Physics A: Mathematical and General*, *19*, L1093.
12. Cardy, J. L. (1986). Operator content of two-dimensional conformally invariant theories. *Nuclear Physics B*, *270*, 186.

13. Caron, L. G., & Bourbonnais, C. (1984). Two-cutoff renormalization and quantum versus classical aspects for the one-dimensional electron-phonon system. *Physical Review B*, *29*, 4230–4241.
14. Caron, L. G., & Moukouri, S. (1996). Density matrix renormalization group applied to the ground state of the *XY* spin-Peierls system. *Physical Review Letters*, *76*, 4050.
15. Citro, R., Orignac, E., & Giamarchi, T. (2005). Adiabatic-antiadiabatic crossover in a spin-Peierls chain. *Physical Review B*, *72*, 024434.
16. Cross, M. C., & Fisher, D. S. (1979). A new theory of the spin-Peierls transition with special relevance to the experiments on TTFCuBDT. *Physical Review B*, *19*, 402.
17. Dashen, R. F., Hassiacher, B., & Neveu, A. (1974). Nonperturbative methods and extended-hadron models in field theory. I. semiclassical functional methods. *Physical Review D*, *10*, 4114–4129.
18. Fehske, H., Holicki, M., & Weiße, A. (2000). Lattice dynamical effects on the peierls transition in one-dimensional metals and spin chains. *Advances in Solid State Physics*, *40*, 235–250.
19. Fradkin, E., & Hirsch, J. E. (1983). Phase diagram of one-dimensional electron-phonon systems. I. the Su-Schrieffer-Heeger model. *Physical Review B*, *27*, 1680–1697.
20. Fukui, K., & Todo, S. (2009). Order-*N* cluster Monte Carlo method for spin systems with long-range interactions. *Journal of Computational Physics*, *228*, 2629.
21. Geertsma, W., & Khomskii, D. (1996). Influence of side groups on 90 Figa superexchange: A modification of the Goodenough-Kanamori-Anderson rules. *Physical Review B*, *54*, 3011–3014.
22. Gros, C., & Werner, R. (1998). Dynamics of the Peierls-active phonon modes in $CuGeO_3$. *Physical Review B*, *58*, R14677.
23. Harada, K., & Kawashima, N. (1997). Universal jump in the helicity modulus of the two-dimensional quantum XY model. *Physical Review B*, *55*, R11949.
24. Harada, K., & Kawashima, N. (1998). Kosterlitz-thouless transition of quantum XY model in two dimensions. *Journal of the Physical Society of Japan*, *67*, 2768.
25. Hase, M., Terasaki, I., & Uchinokura, K. (1993). Observation of the spin-Peierls transition in linear Cu^{2+} (spin-$\frac{1}{2}$) chains in an inorganic compound $CuGeO_3$. *Physical Review Letters*, *70*, 3651.
26. Huizinga, S., Kommandeur, J., Sawatzky, G. A., Thole, B. T., Kopinga, K., de Jonge, W. J. M., et al. (1979). Spin-Peierls transition in N-methyl-N-ethyl-morpholinium-ditetracyanoquinodimethanide [MEM-$(TCNQ)_2$]. *Physical Review B*, *19*, 4723–4732.
27. Jeckelmann, E., Zhang, C., & White, S. R. (1999). Metal-insulator transition in the one-dimensional Holstein model at half filling. *Physical Review B*, *60*, 7950–7955.
28. Kikuchi, J., Matsuoka, T., Motoya, K., Yamauchi, T., & Ueda, Y. (2002). Absence of edge localized moments in the doped spin-Peierls system $CuGe_{1-x}Si_xO_3$. *Physical Review Letters*, *88*, 037603.
29. Kosterlitz, J. M., & Thouless, D. J. (1973). Ordering, metastability and phase transitions in two-dimensional systems. *Journal of Physics C*, *6*, 1181.
30. Kuboki, K., & Fukuyama, H. (1987). Spin-Peierls transition with competing interactions. *Journal of the Physical Society of Japan*, *56*, 3126–3134.
31. Kühne, R. W., & Löw, U. (1999). Thermodynamical properties of a spin-$\frac{1}{2}$ Heisenberg chain coupled to phonons. *Physical Review B*, *60*, 12125.
32. Landau, D. P., & Binder, K. (2005). *A guide to Monte Carlo simulations in statistical physics* (2nd ed.). Cambridge: Cambridge University Press.
33. Ludwig, A. W. W., & Cardy, J. L. (1987). Perturbative evaluation of the conformal anomaly at new critical points with applications to random systems. *Nuclear Physics B*, *285*, 687.
34. McKenzie, R. H., Hamer, C. J., & Murray, D. W. (1996). Quantum Monte Carlo study of the one-dimensional Holstein model of spinless fermions. *Physical Review B*, *53*, 9676–9687.
35. Michel, F., & Evertz, H. G. (2007). Lattice dynamics of the Heisenberg chain coupled to finite frequency bond phonons. cond-mat p. arXiv:0705.0799v2.
36. Nakano, T., & Fukuyama, H. (1981). Dimerization and solitons in one-dimensional XY-Z antiferromagnets. *Journal of the Physical Society of Japan*, *50*, 2489–2499.

37. Nelson, D. R., & Kosterlitz, J. M. (1977). Universal jump in the superfluid density of two-dimensional superfuilds. *Physical Review Letters*, *39*, 1201–1204.

38. Okamoto, K., & Nomura, K. (1992). Fluid-dimer critical point in $S = \frac{1}{2}$ antiferromagnetic Heisenberg chain with next nearest neighbor interactions. *Physics Letters A*, *169*, 433.

39. Olsson, P., & Minnhagen, P. (1991). On the helicity modulus, the critical temperature and Monte Carlo simulations for the two-dimensional XY-model. *Physica Scripta*, *43*, 203–209.

40. Onishi, H., & Miyashita, S. (2003). Quantum narrowing effect in a spin-Peierls system with quantum lattice fluctuation. *Journal of the Physical Society of Japan*, *72*, 392.

41. Pearson, C. J., Barford, W., & Bursill, R. J. (2010). Quantized lattice dynamic effects on the spin-Peierls transition. *Physical Review B*, *82*, 144408.

42. Pouget, J. P. (2001). Microscopic interactions in $CuGeO_3$ and organic spin-Peierls systems deduced from their pretransitional lattice fluctuations. *European Physical Journal B: Condensed Matter Physics*, *20*, 321–333.

43. Pouget, J. P., Ravy, S., Schoeffel, J., Dhalenne, G., & Revcolevshi, A. (2004). Spin-Peierls lattice fluctuations and disorders in $CuGeO_3$ and its solid solutions. *European Physical Journal B: Condensed Matter Physics*, *38*, 581–598.

44. Raas, C., Bühler, A., & Uhrig, G. S. (2001). Effective spin models for spin-phonon chains by flow equations. *European Physical Journal B: Condensed Matter Physics*, *21*, 369–374.

45. Raas, C., Löw, U., Uhrig, G. S., & Kühne, R. W. (2002). Spin-phonon chains with bond coupling. *Physical Review B*, *65*, 144438.

46. Regnault, L. P., Renard, J. P., Dhalenne, G., & Revcolevschi, A. (1995). Coexistence of dimerization and antiferromagnetism in Si-doped $CuGeO_3$. *Europhysics Letters*, *32*, 579–584.

47. Reinicke, P. (1987). Analytical and non-analytical corrections to finite-size scaling. *Journal of Physics A*, *20*, 5325.

48. Sandvik, A. W., & Campbell, D. K. (1999). Spin-Peierls transition in the Heisenberg chain with finite-frequency phonons. *Physical Review Letters*, *83*, 195.

49. Shastry, B. S., & Sutherland, B. (1990). Twisted boundary conditions and effective mass in Heisenberg-Ising and Hubbard rings. *Physical Review Letters*, *65*, 243–246.

50. Simonet, V., Grenier, B., Villain, F., Flank, A. M., Dhalenne, G., Revcolevschi, A., et al. (2006). Effect of structural distortions on the magnetism of doped spin-Peierls $CuGeO_3$. *European Physical Journal B: Condensed Matter Physics*, *53*, 155–167.

51. Sun, P., Schmeltzer, D., Bishop, A. R. (2000). Analytic approach to the one-dimensional spin-Peierls system in the entire frequency range. *Physical Review B*, *62*, 11,308–11,311.

52. Trebst, S., Elstner, N., & Monien, H. (2001). Renormalization of the spin-Peierls transition due to phonon dynamics. *Europhysics Letters*, *56*(2), 268–274.

53. Uchinokura, K. (2002). Spin-Peierls transition in $CuGeO_3$ and impurity-induced ordered phases in low-dimensional spin-gap systems. *Journal of Physics: Condensed Matter*, *14*, R195–R237.

54. Uhrig, G. S. (1998). Nonadiabatic approach to spin-Peierls transitions via flow equations. *Physical Review B*, *57*, R14004.

55. van Bodegom, B., Larson, B. C., & Mook, H. A. (1981). Diffuse x-ray and inelastic neutron scattering study of the spin Peierls transition in N-methyl-N-ethyl-morpholinium bistetracyanoquinodimethane [MEM (TCNQ)$_2$]. *Physical Review B*, *24*, 1520–1523.

56. Visser, R. J. J., Oostra, S., Vettier, C., & Voiron, J. (1983). Determination of the spin-Peierls distortion in N-methyl-N-ethyl-morpholinium ditetracyanoquinodimethanide [MEM(TCNQ)$_2$]: Neutron diffraction study at 6 K. *Physical Review B*, *28*, 2074–2077.

57. Voit, J., & Schulz, H. J. (1988). Electron-phonon interaction and phonon dynamics in one-dimensional conductors. *Physical Review B*, *37*, 10,068–10,085.

58. Weber, H., & Minnhagen, P. (1988). Monte Carlo determination of the critical temperature for the two-dimensional XY mode. *Physical Review B*, *37*, 5986.

59. Weiße, A., Hager, G., Bishop, A. R., & Fehske, H. (2006). Phase diagram of the spin-Peierls chain with local coupling: Density-matrix renormalization-group calculations and unitary transformations. *Physical Review B*, *74*, 214426.

60. Weiße, A., Wellein, G., & Fehske, H. (1999). Quantum lattice fluctuations in a frustrated Heisenberg spin-Peierls chain. *Physical Review B*, *60*, 6566.

61. Wellein, G., Fehske, H., & Kampf, A. P. (1998). Peierls dimerization with nonadiabatic spin-phonon coupling. *Physical Review Letters*, *81*, 3956.
62. Werner, R., Gros, C., & Braden, M. (1999). Microscopic spin-phonon coupling constants in $CuGeO_3$. *Physical Review B*, *59*, 14,356–14,366.
63. Witten, E. (1984). Non-abelian bosonization in two dimensions. *Communications in Mathematical Physics*, *92*, 455–472.
64. Zheng, H. (1997). Quantum lattice fluctuations in the ground state of an XY spin-Peierls chain. *Physical Review B*, *56*, 14,414–14,422.

Chapter 6
Multi-Chain Spin-Peierls Systems

6.1 Simulation for Dispersive Phonon

We consider the multi-chain and the two-dimensional spin-Peierls systems in this chapter. Let us connect the spin-Peierls chain by the lattice interaction. The Hamiltonian is expressed as

$$H = \sum_{\mathbf{r}} J \left(1 + \alpha q_{\mathbf{r}}\right) S_{\mathbf{r}+\mathbf{e_x}} \cdot S_{\mathbf{r}} + \sum_{\mathbf{r}} \left[\frac{p_{\mathbf{r}}^2}{2m} + \frac{c}{2} \left(q_{\mathbf{r}}^2 + \gamma_y (q_{\mathbf{r}+\mathbf{e_y}} - q_{\mathbf{r}})^2 \right. \right.$$
$$\left. \left. + \gamma_{xy}(q_{\mathbf{r}+\mathbf{e_x}+\mathbf{e_y}} - q_{\mathbf{r}})^2 + \gamma_{xy}(q_{\mathbf{r}-\mathbf{e_x}+\mathbf{e_y}} - q_{\mathbf{r}})^2 \right) \right], \tag{6.1}$$

where x axis is the spin-chain direction and y axis is perpendicular to the chain direction. The parameters $\gamma_x > 0$ and $\gamma_{xy} > 0$ are the ratio of the spring constant between atoms, and the other parameters are defined as before, in Chap. 3. We consider an optimal phonon mode with a gap $\omega = \sqrt{cm}$ and the isotropic case ($\Delta = 1$). This extension from the one-dimensional model is reasonable because the usual lattice structure does not have a strong low-dimensional feature in contrast to the electron interaction that would have it depending strongly on the orbital shape; that is why the atoms form the lattice. Our purpose in this chapter is to correctly investigate an effectively frustrated two-dimensional spin model by means of the developed methods in this thesis.

We, here, rewrite the Hamiltonian for efficient QMC simulation. Let us perform the Fourier transformation for the lattice degree of freedom and the second quantization in the reciprocal space. Then we again perform the inverse Fourier transformation to the real space. Finally the Hamiltonian (6.1) is exactly transformed as

$$H = \sum_{\mathbf{r}} J \left(1 + \alpha \sum_{\mathbf{r}'} R(\mathbf{r} - \mathbf{r}')(a_{\mathbf{r}'} + a_{\mathbf{r}'}^{\dagger})\right) S_{\mathbf{r}+\mathbf{e_x}} \cdot S_{\mathbf{r}} + \sum_{\mathbf{r}} \sum_{\mathbf{r}'} K(\mathbf{r} - \mathbf{r}') a_{\mathbf{r}}^{\dagger} a_{\mathbf{r}'}, \tag{6.2}$$

where the coefficients $R(\mathbf{r} - \mathbf{r}')$ and $K(\mathbf{r} - \mathbf{r}')$ give the nonlocal spin-phonon and the phonon-phonon interaction, respectively. They are defined as

$$R(\mathbf{r} - \mathbf{r}') = \frac{1}{N} \sum_{\mathbf{k}} \sqrt{\frac{1}{2m\omega_{\mathbf{k}}}} e^{i\mathbf{k}\cdot(\mathbf{r} - \mathbf{r}')} \tag{6.3}$$

$$K(\mathbf{r} - \mathbf{r}') = \frac{1}{N} \sum_{\mathbf{k}} \omega_{\mathbf{k}} e^{i\mathbf{k}\cdot(\mathbf{r} - \mathbf{r}')}, \tag{6.4}$$

where $\omega_{\mathbf{k}}$ is the phonon dispersion:

$$\omega_{\mathbf{k}} = \sqrt{\frac{c}{m}\left(1 + 2\gamma_y(1 - \cos k_y) + 2\gamma_{xy}(1 - \cos(k_x + k_y)) + 2\gamma_{xy}(1 - \cos(k_y - k_x)))\right.}. \tag{6.5}$$

Here, the amplitude of $R(r)$ and $K(r)$ is dumped exponentially with $r = |\mathbf{r}|$. About the signs, $R(r) > 0 \ \forall r$, $K(0) > 0$, and $K(r) < 0 \ (r \neq 0)$. Remind us that the number of the spin-phonon interaction operators on the worldlines is always even. Thus, the sign of $R(r)$ does not matter if they are the same. On the other hand, the boson hopping (off-diagonal) terms $K(r)(r \neq 0)$ multiplied by $(-\beta)$ gives a positive weight. Although the diagonal term $(K(0))$ is positive, we can avoid the negative weight by including the term into H_0 in the continuous-time representation (3.5) as we did in Chap. 3. Therefore, no negative sign appears. Note that the sign problem emerges for very strong spin-phonon coupling region, but such a parameter set is beyond the scope of this model.

In order for the hopping term to appear on the worldline, we prepare a combined operator $L(\mathbf{r} - \mathbf{r}')$ as

$$L(\mathbf{r} - \mathbf{r}') = \frac{K(\mathbf{r} - \mathbf{r}')}{2}\left(\frac{a_{\mathbf{r}}^{\dagger} a_{\mathbf{r}} + a_{\mathbf{r}'}^{\dagger} a_{\mathbf{r}'} + 1}{2} + a_{\mathbf{r}}^{\dagger} a_{\mathbf{r}'} + a_{\mathbf{r}} a_{\mathbf{r}'}^{\dagger}\right). \tag{6.6}$$

Using this operator, we rewrite the lattice term in the model as

$$\sum_{\mathbf{r}}\sum_{\mathbf{r}'} K(\mathbf{r} - \mathbf{r}') a_{\mathbf{r}}^{\dagger} a_{\mathbf{r}'} = \sum_{\mathbf{r}}\left(K(0) + \frac{K_{\text{off}}}{2}\right) a_{\mathbf{r}}^{\dagger} a_{\mathbf{r}} + \sum_{\mathbf{r}\neq\mathbf{r}'} L(\mathbf{r} - \mathbf{r}'), \tag{6.7}$$

where

$$K_{\text{off}} = -\sum_{\mathbf{r}\neq\mathbf{r}'} K(\mathbf{r} - \mathbf{r}'). \tag{6.8}$$

We can efficiently change the type of operators on the worldlines by the worm thanks to this operator separation; the weights of the diagonal part and the off-diagonal part

of $L(\mathbf{r} - \mathbf{r}')$ are always in the same order. In more detail, we insert $L(\mathbf{r} - \mathbf{r}')$ as

$$L(\mathbf{r} - \mathbf{r}')_{\text{diagonal}} = \frac{K(\mathbf{r} - \mathbf{r}')}{4} \left(a_{\mathbf{r}}^{\dagger} a_{\mathbf{r}} + a_{\mathbf{r}'}^{\dagger} a_{\mathbf{r}'} + 1 \right) \tag{6.9}$$

during the diagonal update. Then we alter it by the worm to

$$L(\mathbf{r} - \mathbf{r}')_{\text{off-diagonal 1}} = \frac{K(\mathbf{r} - \mathbf{r}')}{2} a_{\mathbf{r}}^{\dagger} a_{\mathbf{r}'} \tag{6.10}$$

or

$$L(\mathbf{r} - \mathbf{r}')_{\text{off-diagonal 2}} = \frac{K(\mathbf{r} - \mathbf{r}')}{2} a_{\mathbf{r}} a_{\mathbf{r}'}^{\dagger}. \tag{6.11}$$

In the simulation for $S = 1/2$ and $\Delta = 1$, we set the diagonal exponential term (H_0) and perturbation term (V) in Eq. (3.5) as

$$H = H_0 + V \tag{6.12}$$

$$H_0 = \sum_{\mathbf{r}} \left(K(\mathbf{0}) + \frac{K_{\text{off}}}{2} \right) a_{\mathbf{r}}^{\dagger} a_{\mathbf{r}}. \tag{6.13}$$

$$V = \sum_{\mathbf{r}} \tilde{J}(1 + \tilde{\alpha} \sum_{\mathbf{r}'} R(\mathbf{r} - \mathbf{r}')(a_{\mathbf{r}'} + a_{\mathbf{r}'}^{\dagger}))(S_{\mathbf{r}+\mathbf{e}_{\mathbf{x}}} \cdot S_{\mathbf{r}} - \frac{1}{4})$$
$$+ \sum_{\mathbf{r} \neq \mathbf{r}'} L(\mathbf{r} - \mathbf{r}'), \tag{6.14}$$

where

$$\tilde{J} = J - \frac{J^2 \alpha^2}{4c} \tag{6.15}$$

$$\tilde{J}\tilde{\alpha} = J\alpha. \tag{6.16}$$

In the simulation, we control the parameter $\omega = \sqrt{c/m}$, and $\lambda = \alpha^2/c$ as the same with before. The differences from the one-dimensional simulation are only the following two points: the boson hopping term and the (exponentially-decaying) non-local interactions. In the diagonal update, we insert/remove the diagonal operators of the Hamiltonian as mentioned in Sect. 3.4.2. The matrix elements of $L(\mathbf{r} - \mathbf{r}')$ vary on the imaginary time and have no upper weight because the phonon is now expressed as a soft-core boson. Then we set a guiding weight, at each Monte Carlo step, for the insertion/removal of the diagonal terms of $L(\mathbf{r} - \mathbf{r}')$; that is, we use a constant intensity instead of the exact value at each imaginary time for efficiency, which is allowed as we explained in the section. When we choose an operator for the insertion, we use an efficient algorithm called *Walker's method of alias* [2] and succeed in significantly reducing the CPU time cost coming from the non-local interaction. In the off-diagonal update, on the other hand, the bosonic worm hops

to a different site. When the worm warps or the bug starts/finishes, we consider the interaction between different spin sites and boson sites with weights $R(\mathbf{r} - \mathbf{r}')$.

6.2 Unfrustrated Multi Chain

Let us consider, first, an unfrustrated case where $\gamma_y \neq 0$, $\gamma_{xy} = 0$. We investigate if an order takes place by introducing the interchain phonon interaction to the liquid chain. The parameters are set as $\omega = 1/4$, $\lambda = \gamma_y$, $\beta = L$ and we vary λ and γ_y simultaneously. Let us see the two-chain (ladder) case. Figure 6.1 shows a moment ratio defined as

$$U_1 = \frac{\langle m_\beta \rangle^2}{\langle m_\beta^2 \rangle},\tag{6.17}$$

where

$$m_\beta(k) = \frac{1}{N} \sum_{\mathbf{r},\mathbf{r}'} \int_0^\beta d\tau\, \hat{O}^\dagger{}_{\mathbf{r}}(\tau)\, \hat{O}_{\mathbf{r}'}\, e^{i\mathbf{k}\cdot(\mathbf{r}-\mathbf{r}')}.\tag{6.18}$$

We use the dimer operator $\hat{O}_{\mathbf{r}} = S_{\mathbf{r}+\mathbf{e_x}} \cdot S_{\mathbf{r}}$ in the expression. This ratio functions as the same with the Binder ratio. In the figure, the dimer order $\mathbf{k} = (\pi, 0)$ develops as the spin-phonon coupling increases, but it is difficult to conclude the transition point from this data.
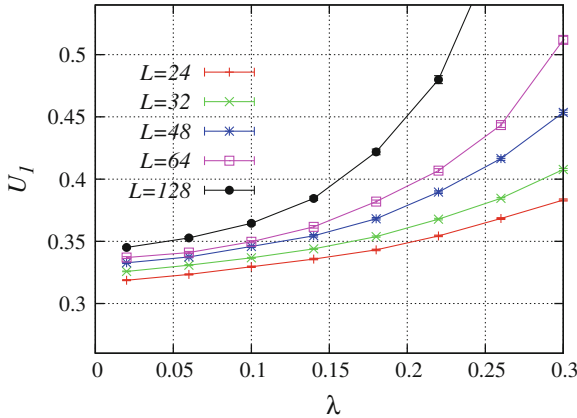

Fig. 6.1 Moment ratio (6.17) of the dimer order parameter $\hat{O}_{\mathbf{r}} = S_{\mathbf{r}+\mathbf{e_x}} \cdot S_{\mathbf{r}}$ of $\mathbf{k} = (\pi, 0)$ for $\omega = 1/4$, $\beta = L$, $\gamma_x = \lambda$, $\gamma_{xy} = 0$. The dimer order develops rapidly as the spin-phonon coupling increases
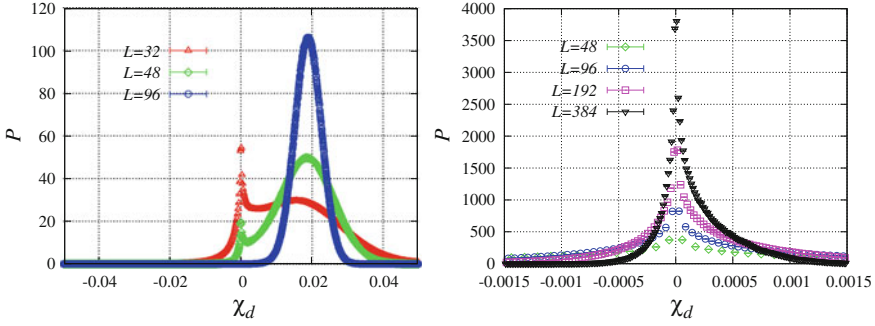
Fig. 6.2 Histogram of the dimer order parameter (6.19) for $\lambda = \gamma_y = 0.5$ (*left*) and $\lambda = \gamma_y = 0.1$ (*right*). The value is normalized so that the integration becomes 1 in the continuous limit. For the strong coupling, the order $(\pi, 0)$ clearly develops. Also for the weak coupling, the asymmetry of the distribution is observed, which indicates it is the ordered phase

Then, we define an order parameter as

$$\chi_d = m_\beta(\pi, 0) - m_\beta(\pi, \pi), \tag{6.19}$$

using $\hat{O}_\mathbf{r} = S_{\mathbf{r}+\mathbf{e_x}} \cdot S_\mathbf{r}$. This quantity, which is nothing but the difference of the susceptibility between $\mathbf{k} = (\pi, 0)$ and $\mathbf{k} = (\pi, \pi)$, detects the dimer pattern. Figure 6.2 shows the histogram of this order parameter for different parameters. The value is normalized so that the integration becomes 1 in the continuous limit. For the both cases ($\lambda = \gamma_y = 0.5, \lambda = \gamma_y = 0.1$), the asymmetry of the distribution is observed. From the above simulations, we expect that the dimer order takes place for infinitesimal interchain phonon coupling.

We discuss the mechanism of the instantaneous effect. The interchain interaction effectively introduces the biquadratic spin interaction, which is derived from the perturbation. An effective ladder model, then, is expressed as

$$H = \sum_{j=1, 2} \sum_n \left[J_1 S_{j, n} \cdot S_{j, n+1} + J_2 S_{j, n} \cdot S_{j, n+2} \right]$$
$$+ \sum_n J_4 (S_{1, n} \cdot S_{1, n+1})(S_{2, n} \cdot S_{2, n+1}). \tag{6.20}$$

The graphical picture of the model is depicted in Fig. 6.3. Here, $J_1, J_2 > 0$, and $J_4 < 0$ [6]. In the continuum limit with the bosonization, this Hamiltonian decouples into four massive real fermionic fields, or equivalently, four noncritical 2D Ising models with underlying $SU(2) \times Z_2$ symmetry [9]. Nersesyan and Tsvelik [6] discussed the phase diagram of the spin model with the J_4 term and also the interchain bilinear spin interaction. On one hand, the J_2 term corresponds to the marginal operator in the theory as discussed in Sect. 4.2. The J_4 term, on the other hand, is relevant (the dimension is 1). Therefore, the interchain phonon interaction instantaneously
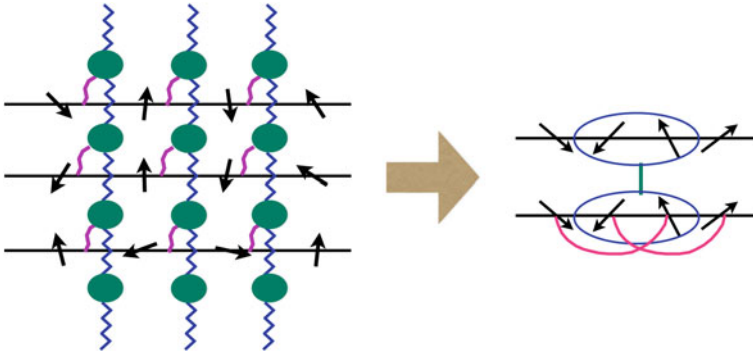
Fig. 6.3 Picture of the effective spin model (6.20) after tracing out the phonon degree of freedom. In addition to J_1 and J_2 (interactions within the chain), the interchain phonon interaction introduces the J_4 term in the model

introduces the gap and the spinon confinement [4]. This explanation will be valid for unfrustrated multi-chains and the two-dimensional system (infinite chain).

6.3 Frustrated Multi Chain

Next, we investigate the frustration effect of the spin-Peierls model in this section. The frustration of the interchain interaction can restore the characteristic one-dimensional features. As one of them, the *spinon deconfinement* in the frustrated spin models has been discussed in many papers [1, 5, 7, 10, 11]. We set the parameters of the interchain phonon interaction as $\gamma_y = 2\gamma_{xy}$; that is, the interaction is fully frustrated. The lattice-interaction bonds are shown in Fig. 6.4 (the spins are omitted).

The left panel in Fig. 6.5 shows the histogram of the order parameter (6.19) for the frustrated ladder $\gamma_y = 2\gamma_{xy} = 0.04$, $\lambda = 0.1$, $\omega = 1/4$, $\beta = L$. No order and asymmetry is observed in the distribution. For a strong spin-phonon coupling
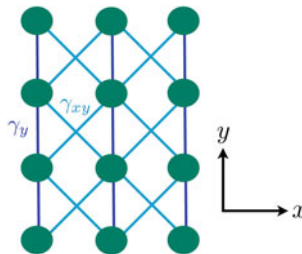

Fig. 6.4 Picture of the lattice-interaction bonds in the model (6.1). The spin chain extends in x direction, which in not drawn in the figure. When the ratio is as $\gamma_y = 2\gamma_{xy}$, the interchain interaction is fully frustrated
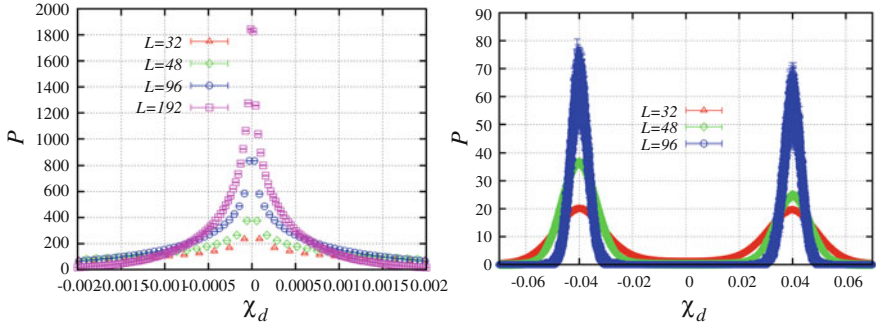
Fig. 6.5 Histogram of the order parameter for the frustrated ladder for $\lambda = 0.1$ (*left*) and $\lambda = 1.2$ (*right*). On the *left panel*, there seems no order and asymmetry in the distribution. On the *right panel*, the double-peak structure appears. Thus the ground state is the liquid state for the small spin-phonon coupling and the dimer state for the large coupling. The double-peak structure corresponds to the 4-degenerated ground state
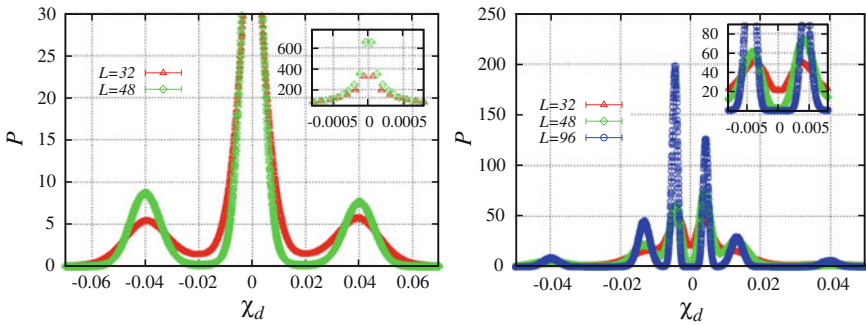

Fig. 6.6 Histogram of the order parameter for the frustrated 4-chain (*left*) and 6-chain (*right*) system. The number of peaks (6.21) is consistent with the 2^n-degenerated ground-state case for $n = 4, 6$

$\lambda = 1.2$ on the right panel, on the other hand, the double-peak structure appears. This structure shows the uncorrelation between the chains and the 4 degenerated ground state; that is, the 2 states with $\mathbf{k} = (\pi, 0)$ and the 2 states with $\mathbf{k} = (\pi, \pi)$ have the same energy ($Z_2 \times Z_2$). In order to confirm this degeneracy, we also investigate the histogram for the 4-chain and 6-chain system as shown in Fig. 6.6. Here, if we assume the 2^n degeneracy for the n-chain system, we can show the number of peaks $a(n)$ should be

$$a(n) = \begin{cases} k(k+1) & n = 4k - 2 \\ k(k+1) + 1 & n = 4k. \end{cases} \tag{6.21}$$

We see the number of peaks in the figure matches the above expression: $a(4) = 3$ and $a(6) = 6$ (we confirmed also more chain cases). Thus, the quantum phase transition is

Fig. 6.7 Level crossing between the $S = 1$ triplet gap and the $S = 0$ singlet gap for the frustrated ladder with $\gamma_y = 2\gamma_{xy} = 0.1$, $\omega = 1/4$, $\beta = L$. The index n corresponds to the order of the gap estimator as Eq. (4.31). The transition point is roughly extrapolated as $\lambda_c \sim 0.37$, which differs from the single chain case
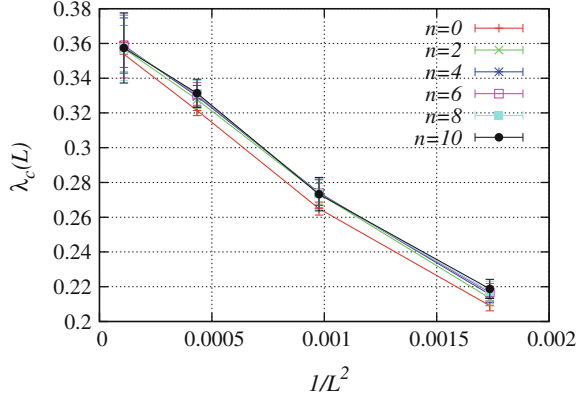
expected to occur at a finite coupling constant with the spontaneously Z_{2^n} symmetry braking.

We then observe the level crossing between the $S = 1$ triplet excitation gap and the $S = 0$ singlet excitation gap for $\gamma_y = 2\gamma_{xy} = 0.1$ as shown in Fig. 6.7. Since the chains are uncorrelated, the singlet excitations in y direction are degenerated. The crossing point is scaled as the same way with the one-dimensional case. We can estimate the transition point as $\lambda_c \sim 0.37$. Remarkably, this value differs from the single-chain case $\lambda_c = 0.225(2)$ in Sect. 5.2. Nevertheless, the interchain phonon interaction does not introduce the chain-chain correlation. In the meanwhile, Batista and Trugman [1] showed the exact ground state of a frustrated two-dimensional spin system and the spinon deconfinement at the transition point between the two valence bond crystal phases. We expect, also in this model, the spinon is not confined by the frustration effect of the interchain interaction in contrast to the unfrustrated case. Thus the level crossing and spectroscopy analysis will be effective for this case as the same with the single-chain system.

6.4 Two-Dimensional System

Furthermore, we investigate the two-dimensional (infinite chain) frustrated system. It is expected that the phase diagram is qualitatively the same with the frustrated ladder system because the chains are uncorrelated. Figure 6.8 shows the level crossing between the triplet gap and singlet gap for $L = 4W$, $\gamma_y = 2\gamma_{xy} = 0.04$, $\omega = 1/4$, $\beta = L$, where L and W is the number of spins/atoms in x and y direction, respectively. The crossing point in the thermodynamic limit can be extrapolated as $\lambda_c \sim 0.28$ that differs from the single chain case in a similar way to the ladder. In this two-dimensional case, the broken symmetry is not trivial, which is corresponding to $Z_{2W}(W \to \infty)$. The ground state in the ordered phase is macroscopically degenerated. From the above calculations, we conclude the quantum phase transition occurs from the $1D-$like (spin) liquid phase to the macroscopically-degenerated
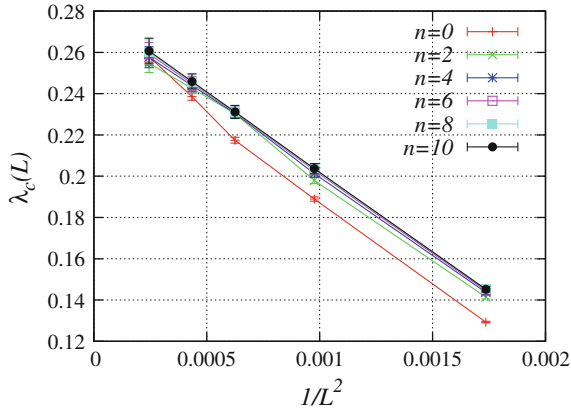
Fig. 6.8 Level-crossing points for $L = 4W$, $\gamma_y = 2\gamma_{xy} = 0.04$, $\omega = 1/4$, $\beta = L$. The crossing point in the thermodynamic limit can be extrapolated as $\lambda_c \sim 0.28$ that differs from the single chain case in a similar way to the ladder

dimer phase at the finite spin-phonon coupling. The both phases on the fully frustrated line ($\gamma_y = 2\gamma_{xy}$) are located at the boundary between the doubly-degenerated dimer (valence bond crystal) phases as in Fig. 6.9. In the spin liquid phase, on one hand, the spinon is deconfined. In the macroscopically-degenerate phase, on the other hand, the vison [3, 8] will appear as the exotic excitation.
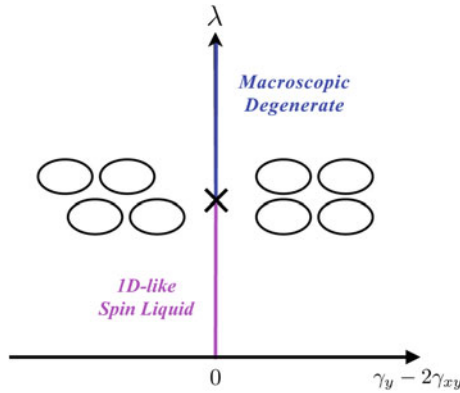
Fig. 6.9 Expected ground-state phase diagram of the two-dimensional spin-Peierls system. The phase diagram consists of the 4 phases: the doubly-degenerated dimer phase with $\mathbf{k} = (\pi, 0)$ ($\gamma_y - 2\gamma_{xy} > 0$), $\mathbf{k} = (\pi, \pi)$ ($\gamma_y - 2\gamma_{xy} < 0$), the 1D-like spin liquid phase with the deconfined spinon ($\gamma_y = 2\gamma_{xy}$, $\lambda < \lambda_c$), and the macroscopically-degenerated dimer phase ($\gamma_y = 2\gamma_{xy}$, $\lambda > \lambda_c$)

6.5 Discussion

Finally, let us discuss the order of magnitude for the effective spin interaction. From the perturbation expansion for the interchain lattice interaction, the effective interchain spin interaction J_4 for the unfrustrated case (6.20) is expanded as

$$J_4 \sim a_1 \lambda \gamma_y + a_2 \lambda \gamma_y^2 + \cdots , \tag{6.22}$$

where a_1 and a_2 are coefficients independent of λ and γ_y. As we have seen for the unfrustrated cases, the asymmetry of the order parameter distribution is clearly seen for $\lambda = 0.5$, $\gamma_y = 0.5$, $L = \beta \geq 32$ and for $\lambda = 0.1$, $\gamma_y = 0.1$, $L = \beta \geq 96$ in Sect. 6.2. On the other hand, it is not so clear for $\lambda = 0.1$, $\gamma_y = 0.1$, $L = \beta = 48$. Thus, the order of the coefficient for $\omega = 1/4$ can be roughly estimated as $a_1 \sim O(1)$. For the frustrated ladder, no asymmetry is observed for $\lambda = 0.1$, $\gamma_y = 2\gamma_{xy} = 0.04$, $L = \beta \leq 192$ as shown in Sect. 6.3. These sizes are likely not enough to conclude that the biquadratic J_4 term cancels for the frustrated case because the next order term $a_2 \lambda \gamma_y^2$ is smaller than $1/\beta$ with the assumption that a_2 is also in $O(1)$. Moreover, the higher-order effective spin interactions are also in $O(\lambda \gamma_y^2)$. Therefore, the precise calculation for larger system sizes and the detailed expression of the effective spin model are needed for the decisive conclusion. Also for the two-dimensional case, the calculated system sizes and the inverse temperatures may not be enough to conclude the ground state.

In order to assess the dimer order degeneracy, we have simulated the ladder systems with stronger interchain lattice interaction, $\gamma_y = 2\gamma_{xy} = 4$, $\lambda = 1$, $L = \beta$. The dimer order parameter distribution is presented in Fig. 6.10; it is symmetric again until $L = 192$. This result implies that there is no dimer order in the thermodynamic limit because even the much higher order terms do not lift the degeneracy.
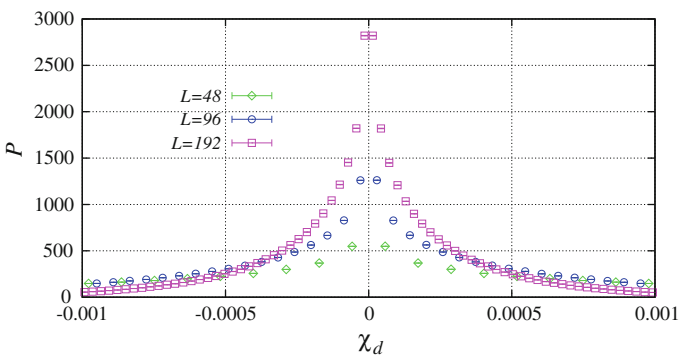

Fig. 6.10 Histogram of the order parameter for the frustrated ladder for $\gamma_y = 2\gamma_{xy} = 4$, $\omega = 1/4$, $\lambda = 1$, $\beta = L$. No dimer order appears even with this stronger interchain lattice coupling parameters

Furthermore, not only the ladder but also the two-dimensional system as investigated above is to be liquid. Therefore, the interesting phase diagram (Fig. 6.9) is expected to be correct.

As we have discussed the order of the effective interaction, the ground state of such a frustrated system is difficult to clarify. However, we insist here that our results are free from *approximation* except the tiny bias from the MCMC scheme. Thus it is possible to observe the nontrivial quantum states appearing on the fully-frustrated line at very-low temperatures experimentally.

References

1. Batista, C. D., & Trugman, S. A. (2004). Exact ground states of a frustrated 2d magnet: Deconfined fractional excitations at a first-order quantum phase transition. *Physical Review Letters*, *93*, 217–202.
2. Fukui, K., & Todo, S. (2009). Order-N cluster Monte Carlo method for spin systems with long-range interactions. *Journal of Computational Physics*, *228*, 2629.
3. Steven Kivelson, A., Rokhsar Daniel, S., Sethna James, P. (1987). Topology of the resonating valence-bond state: Solitons and high-T, superconductivity. *Physics Review B*, *35*, 8865–8868.
4. Lake, B., Tsvelik, A. M., Notbohm, S., Tennant, D. A., Perring, T. G., Reehuis, M., et al. (2010). Confinement of fractional quantum number particles in a condensed-matter system. *Nature Physics*, *6*, 50–55.
5. Mastrogiuseppe, D., Gazza, C., & Dobry, A. (2008). Dimerization process and elementary excitations in spin-Peierls chains coupled by frustrated interactions. *Journal of Physics: Condense Matter*, *20*, 135–223.
6. Nersesyan, A., & Tsvelik, A. M. (1997). One-dimensional spin-liquid without magnon excitations. *Physical Review Letters*, *78*, 3939–3942.
7. Nersesyan, A., Tsvelik, A. M. (2003). Spinons in more than one dimension: Resonance valence bond state stabilized by frustration. *Physical Review B*, *67*, 024422.
8. Senthil, T., & Fisher Matthew, P. A. (2001). Fractionalization in the cuprates: Detecting the topological order. *Physical Review Letters*, *86*, 292–295.
9. Shelton, D. G., Nersesyan, A. A., & Tsvelik, A. M. (1996). Antiferromagnetic spin ladders: Crossover between spin $S = 1/2$ and $S = 1$ chains. *Physical Review B*, *53*, 8521–8532.
10. Starykh, O. A., Balents, L. (2004). Dimerized phase and transitions in a spatially anisotropic square lattice antiferromagnet. *Physics Review Letter*, *93*, 127–202.
11. Tsvelik, A. M. (2004). Confinement and deconfinement of spinons in a frustrated spin-1/2 Heisenberg model. *Physical Review B*, *70*, 134–412.

Chapter 7
Summary

In this thesis, we have developed the novel Monte Carlo methods and investigated precisely the critical phenomena of the spin-Peierls systems. The key theme is that the quantum lattice fluctuation introduces the spin frustration. The concept of the Peierls transition originates from the simple but drastic property about the instability to dimerization of the one-dimensional metal as early as 50's. The lattice degree of freedom, there, was treated *adiabatically*; that is, it was approximated as a classical parameter. Over 1970's, it was experimentally shown that the quasi one-dimensional quantum spin system can realistically dimerize through the spin-lattice interaction. The adiabatic approximation based on the mean-field treatment was effective for the dimerization mechanism of the organic materials. The discovery of the first inorganic spin-Peierls material $CuGeO_3$ [1] in 1993 brightly shed light on the importance of the quantum nature of the lattice degree of freedom. It has been shown that the quantum spin system is *antiadiabatically* perturbed by the quantum phonon, and acquires effective frustration that gives birth to various nontrivial physics in the condensed matter, such as the spin-Peierls transition.

The complexity of the multi-degree of freedoms has hindered the precise investigation of the quantum spin-phonon systems. Our result in the present thesis is the significant progress in the analysis of the spin-phonon systems. We can simulate the spin-Peierls models without any systematic error and investigate the phase transitions accurately. Our modifications were mainly on the following three points: the new optimization algorithms of the Markov chain transition kernel based on the geometric weight allocation, the extension of the worm (directed-loop) algorithm for nonconserved particles, and the quantum Monte Carlo level spectroscopy.

On the first point, we have invented the several algorithms that always minimize the average rejection rate in the Markov chain Monte Carlo method in Chap. 2. We demonstrated that our algorithm is the best update method so far for the single spin update of the Potts model and the worm algorithm of the Heisenberg model under the magnetic field, compared to the several existing methods. Also for the spin-Peierls model, the sampling efficiency is significantly improved. Our optimization scheme using the geometric allocation is totally different from the conventional optimization

method. The usefulness of such a geometric approach has been shown beyond the usual algebraic approaches. In the meantime, the Markov chain Monte Carlo method has evolved within the paradigm of the detailed balance since the invention in 1953 by Metropolis et al. This condition is, however, not necessary. Our algorithm is the first versatile method that satisfies the total balance without imposing the detailed balance. We have shown the extension of the algorithm to continuous variables. These new methods will improve the efficiency of almost all kinds of the Markov chain Monte Carlo methods in the future.

About the second point, we have extended the worm algorithm, as a more general method than ever, to nonconserved particles in Chap. 3. The lattice degree of freedom has been treated by the so-called path integral Monte Carlo method so far, where the real-space coordinate basis is used. However, the many problems have deterred efficient calculation and the analysis of the critical phenomena have been extremely difficult. Then, it is a good way to use the second quantization taking the advantage of the discrete nature of the quantum phonon. In the spin-Peierls system, the transformed phonon (soft-core boson) is not a conserved particle in the Hamiltonian. Unfortunately, the conventional worm algorithm cannot treat such a nonconserved particle efficiently. We, thus, have extended the worm update to satisfy the ergodicity and made it possible to measure the nontrivial correlation functions without any systematic error. By this improved scheme, the large-scale spin-Peierls systems became, for the first time, accessible by the quantum Monte Carlo method.

On the third point, we have proposed the new gap estimators and the combined method with the level spectroscopy in Chap. 4. In the one-dimensional spin-Peierls system, the Kosterlitz-Thouless transition occurs where the conventional Monte Carlo analyses break down because of the strong finite-size effect. As a powerful method for the Kosterlitz-Thouless transition of one-dimensional quantum systems, the level spectroscopy was invented by Nomura et al. [2]. The critical dimensions being combined for eliminating the problematic logarithmic correction, it becomes possible to extrapolate the transition point accurately and to identify also the universality class. Meanwhile, the accurate gap estimation is inevitable if we apply the quantum Monte Carlo method to the level spectroscopy. It is, however, far from trivial to estimate it without systematic error. Then, we have proposed the new gap-estimator sequence that systematically approaches to a true value, and succeeded in combining the two methods. As a demonstration, we have shown the level spectroscopy for the alternating-bond model and determined the transition point from much smaller system-size data than the previous Monte Carlo analysis.

In Chap. 5, we have investigated the one-dimensional XXZ spin-Peierls system. The accurate analysis of the large-scale spin-Peierls systems and the phase transition becomes feasible, for the first time, by applying the above three methods. We have determined the phase boundary much more precisely than ever for the isotropic case ($\Delta = 1$). Meanwhile, for the XY-anisotropic case ($\Delta < 1$), there has been no effective method for investigating the critical phenomena. Taking advantage of the level spectroscopy, we have determined the transition point and the universality class as the $k = 1$ $SU(2)$ Wess-Zumino-Witten model, where the emergent $SU(2)$ symmetry appears. Also for the Ising-anisotropic case ($\Delta > 1$), the universality class

has been identified as the Gaussian universality. From the above detailed calculations, we obtained the phase diagram (Fig. 5.22) of the model, and confirmed that it is totally consistent with the $J_1 - J_2$ model, which is an effective model in the antiadiabatic limit. Furthermore, the previous result [3] by the renormalization-group method was checked and we carefully modified it. From these calculations, we have concluded that the phase diagram should continuously connect from the antiadiabatic limit to the adiabatic limit where the Tomonaga-Luttinger liquid phase collapses on the line and the diagram becomes the same with the alternating-bond model. From the viewpoint of the computability, we are successful in investigating the critical phenomena of the effectively frustrated quantum spin system by the quantum Monte Carlo method *without* the negative sign.

Furthermore, we have investigated the multi-chain systems connected by the inter-chain lattice interaction in Chap. 6. For the unfrustrated ladder case, we have observed that the dimer order rapidly develops with the lattice interaction. In order to detect the dimer order more sensitively, we defined the order parameter that is the difference of the dimer susceptibilities with the different wavenumber. Through the close check of the order parameter histogram and the dimension analysis of the effective spin model in the continuum limit, we concluded that the interchain phonon interaction instantaneously drives the ground state into the doubly degenerated dimer phase. For the fully frustrated ladder case, on the other hand, no order and asymmetry was observed for small spin-phonon coupling in the distribution of the order parameter. For large coupling, however, clearly the double-peak structure appears, which indicates the uncorrelation between the chains and the spontaneously $Z_2 \times Z_2$ symmetry breaking. We confirmed the 2^4 and 2^6 degeneracy in the 4-chain and 6-chain cases, respectively. The level-crossing point between the triplet and singlet gap was scaled as the same with the single chain case. We estimated the transition point that significantly differs from the single chain case. Therefore, the interchain phonon interaction indeed plays some role to the critical phenomena although it does not introduce the interchain correlation. Finally, we calculated the two-dimensional (infinite number of chains) case where the number of chains are increased as the chain length. We confirmed again that the level-crossing point is surprisingly scaled as the same with the single chain case, but the extrapolated point differs from the one-dimensional case. Thus, we obtained the expected phase diagram (Fig. 6.9) of the two-dimensional system where the quantum phase transition from the 1D-like spin-liquid phase to the macroscopically-degenerated dimer phase occurs on the fully frustrated line that separates the two doubly-degenerated dimer phases. As an exotic excitation, the deconfined spinon and the vison will play an essential role to the low-energy physics in the liquid phase and the degenerated phases.

For a long time, the accurate analysis of the frustrated quantum spin systems has been impossible in most cases because of the complexity and the negative sign problem. Through this thesis, we have acquired a powerful method to the spin-Peierls or the effectively frustrated spin system without any approximation. Our method will surely clarify nontrivial features of the frustrated spin systems further.

References

1. Hase, M., Terasaki, I., & Uchinokura, K. (1993). Observation of the spin-Peierls transition in linear Cu^{2+} (spin-$\frac{1}{2}$) chains in an inorganic compound $CuGeO_3$. *Physical Review Letters*, *70*, 3651.
2. Nomura, K., & Okamoto, K. (1994). Critical properties of $S = \frac{1}{2}$ antiferromagnetic *XXZ* chain with next-nearest-neighbour interactions. *Journal of Physics A: Mathematical and General*, *27*, 5773.
3. Sun, P., Schmeltzer, D., & Bishop, A. R. (2000). Analytic approach to the one-dimensional spin-Peierls system in the entire frequency range. *Physical Review B*, *62*, 11308–11311.

Curriculum Vitae

Hidemaro Suwa

Date and Place of Birth

May/31/1984 in Kanagawa (Japan)

Email

suwamaro@looper.t.u-tokyo.ac.jp

Research Interests

Monte Carlo method, Numerical method, Condensed-matter physics, Quantum spin systems, Repeated games

Fellowship

April 2012:
Visiting Scholar in Department of Physics, Boston University
JSPS (Japan Society for the Promotion of Science) Postdoctoral Fellow for Research Abroad

Award

Award for Excellent Poster: ISSP, CMSI, Next-Generation Supercomputer Project, Allied Conference, Chiba, January, 2011

Education

March 2012   Ph.D. in Engineering
Title of Thesis: "Geometrically Constructed Markov Chain Monte Carlo Study of Quantum Spin-phonon Complex Systems".

April 2009 to March 2012
Doctoral course in Department of Applied Physics, The University of Tokyo.

March 2009   Master of Engineering
Title of Thesis: "Quantum Monte Carlo Method for Particle Number Non-Conserved Systems and Application to Spin-Peierls Systems".

April 2007 to March 2009
Master's course in Department of Applied Physics, The University of Tokyo.

April 2003 to March 2007
Undergraduate in Department of Applied Physics, The University of Tokyo.

Experience

May 2007 to March 2012
Research Assistant of GCOE (Global Centers of Excellence) program and Grand Challenge in Next-Generation Integrated Nanoscience Computational Materials Science Initiative from MEXT, Japan, and CREST (Core Research for Evolutional Science and Technology) program from JST, Japan.

Publication List

Hidemaro Suwa and Synge Todo
"Markov Chain Monte Carlo Method without Detailed Balance"
Phys. Rev. Lett. **105**, 120603 (2010); arXiv 1007.2262.

Hidemaro Suwa and Synge Todo

"Geometric Allocation Approach for the Transition Kernel of a Markov Chain"
Monte Carlo Methods and Applications, 213–222 (2012); arXiv:1106.3562.
Proceedings of the 8th IMACS Seminar on Monte Carlo Methods, August 29 to September 2, 2011, Borovets, Bulgaria, Edited by Sabelfeld, Karl K. / Dimov, Ivan. DE GRUYTER
Hidemaro Suwa and Synge Todo
Butsuri, 66, 370 (2011) in Japanese.

Arxiv List

Hidemaro Suwa and Synge Todo
"General Construction of Irreversible Kernel in Markov Chain Monte Carlo"
arXiv:1207.0258.

Selected Presentations at International Conferences

Hidemaro Suwa and Synge Todo
"Quantum Monte Carlo Method for Particle Number Non-conserved Systems and
Application to Spin-Peierls Systems".
XXIV IUPAP International Conference on Statistical Physics STATPHYS24, Cairns,
July, 2010.

Hidemaro Suwa and Synge Todo
"Markov Chain Monte Carlo without Detailed Balance and Bounce-free Worm Algorithm".
Monte Carlo Algorithms in Statistical Physics, Melbourne, July, 2010.

Hidemaro Suwa
"Nonreversible Quantum Monte Carlo Analysis for Spin-Peierls Transition".
International Workshop on Recent Developments of Studies on Phase Transitions,
Tokyo, Jun, 2011.

Hidemaro Suwa and Synge Todo
"Geometric Allocation Approach for Transition Kernel of Markov Chain".
Eighth IMACS Seminar on Monte Carlo Methods, Borovets, August, 2011.

Participation in Research Projects

HPCI (High Performance Computing Infrastructure) research project.
"Entanglement Measurement by Quantum Monte Carlo Method and Search of Topological Phases", project manager, September 2012 to March 2014
(https://www.hpci-office.jp/).

ALPS project (Algorithms and Libraries for Physical Simulations), developer, October 2010:
(http://alps.comp-phys.org/).

CMSI (Computational Materials Science Initiative), quantum Monte Carlo group researcher,
November 2011:
(http://www.cms-initiative.jp/en/).

Relevant Professional Skills

Programming Languages: C++/C, Python, Perl, Bourne Shell

Revision Control: Subversion, GitHub, Trac

Numerical Simulations:
Markov chain Monte Carlo method, Sequential Monte Carlo method, Quasi Monte Carlo method, Numerical linear algebra, Cellular automata, Markov Decision Process, Massive parallelization (by MPI, OpenMP).